MODELING AND ASSESSMENT OF GROUNDING SYSTEMS FOR POWER DISTRIBUTION NETWORKS UNDER FAULT CONDITIONS

ZHE LI

PhD

The Hong Kong Polytechnic University

2025

The Hong Kong Polytechnic University

Department of Building Environment and Energy Engineering

Modeling and Assessment of Grounding Systems for Power Distribution Networks under Fault Conditions

Zhe Li

A thesis submitted in partial fulfilment of the requirements for the degree of Doctor of Philosophy

April, 2025

CERTIFICATE OF ORIGINALITY

I hereby declare that this thesis is my own work and that, to the best of my knowledge and belief, it reproduces no material previously published or written, nor material that has been accepted for the award of any other degree of diploma, except where due acknowledgment has been made in the text.

Signed:

Name of Student: Zhe Li

Abstract

thesis entitled:		Modeling and Assessment of Grounding Systems for Power Distribution Networks under Fault Conditions
Submitted by	:	Zhe Li
For the degree of	:	Doctor of Philosophy

This thesis explores the modeling and evaluation of grounding systems in power distribution networks, with a particular focus on addressing the challenges posed by lightning transients and fault conditions. As modern infrastructures become increasingly reliant on sensitive electronic systems, the risks associated with lightning strikes and fault currents have grown significantly, as these systems are more vulnerable to damage. Lightning events can induce high-voltage surges that affect both the power grid and sensitive equipment, while fault conditions, particularly in low-voltage distribution systems, can create hazardous touch voltage levels, leading to potential electrocution risks. Given the growing dependence on electrical and electronic systems in urban environments, ensuring effective grounding solutions is critical for both protecting equipment and ensuring human safety. This research investigates these issues in depth, aiming to provide a better understanding of the behavior of grounding systems under lightning strikes and fault scenarios, with a view to enhancing protective measures and improving overall safety in power distribution networks.

The first part of this research focuses on simulating lightning strikes, a major risk for power distribution networks, particularly in areas with tall structures such as wind turbines. This research introduces a novel Nonlinear Charge Simulation Method (NCSM) to model the charge dynamics in downward negative lightning leaders. This method offers a more accurate representation of the complex electrical interactions that occur during lightning strikes, providing critical insights for improving lightning protection measures in sensitive and critical infrastructure. A hybrid model combining Transmission Line (TL) theory and

Partial Element Equivalent Circuit (PEEC) methods is proposed to simulate the interaction between lightning channels and such structures. This model accounts for electromagnetic coupling effects that are often neglected in conventional lightning simulation approaches. The model not only improves the understanding of lightning-induced transients but also helps in evaluating the performance of lightning protection systems, such as grounding electrodes and surge arresters, in mitigating the effects of lightning strikes on tall structures. This is particularly significant as the size and number of tall structures like wind turbines continue to increase globally, demanding better protection strategies to prevent equipment damage and ensure operational reliability.

In the second part of the thesis, the focus shifts to fault conditions, with an in-depth evaluation of the risks posed by touch voltage and fault potential in low-voltage (LV) distribution systems, particularly in older residential communities with outdated grounding configurations. In such environments, traditional grounding systems often fail to provide adequate protection, increasing the risk of electrocution during faults. This research uses the PEEC method to model various grounding configurations, including TT, TT(M)-C-S, and TX(M)-C-S, assessing their ability to mitigate the risks of electrocution in fault scenarios such as phase-to-ground and line-to-neutral faults. The simulations reveal how different grounding designs affect touch voltage levels and fault potential, highlighting the critical role that grounding configurations play in reducing safety hazards, particularly in areas where modern protective devices are difficult or costly to retrofit. The results from this research demonstrate that specific grounding configurations can significantly reduce the touch voltage levels, making it safer for residents, especially in aging urban communities with outdated electrical infrastructure. Furthermore, the study emphasizes the importance of distributed grounding points along network paths to enhance safety in low-voltage distribution systems, suggesting that such designs can help mitigate the risks of electrocution and improve the overall safety of the electrical system.

In conclusion, the research presents significant advancements in the modeling and assessment of grounding systems, providing a robust framework for understanding and mitigating the risks associated with lightning strikes and electrical faults. These contributions are essential for the development of more resilient, fault-tolerant infrastructures, particularly in aging urban environments,

and provide critical guidance for the design of improved grounding solutions that ensure both human safety and equipment protection in modern power distribution systems.

Keywords: lighting protection, fault protection, PEEC, numerical simulation, electromagnetic transients.

Publications

I. Papers in Journals

- **Z. Li** et al., "Ground Potential Distribution and Human-Body Touch Voltage in Old Residential Communities," in IEEE Transactions on Industry Applications, vol. 59, no. 4, pp. 4980-4989, July-Aug. 2023, doi: 10.1109/TIA.2023.3264198.

- **Z. Li** et al., "Integrated Model for Lightning Strikes on a Tall Structure: Application to a Wind Turbine System," in IEEE Transactions on Electromagnetic Compatibility, vol. 65, no. 1, pp. 271-280, Feb. 2023, doi: 10.1109/TEMC.2022.3215825.

- **Z. Li** et al., "The Lightning Charge Simulation Method Considering Both Nonlinear and Time-variant Physical Behavior for a Downward Negative Leader", in IEEE Transactions on Electromagnetic Compatibility (in preparation)

- J. Cao, **Z. Li**, Y. Ding, Y. Du, J. Wang, Y. Zhang, M. Chen, L. Cai, “Assessment of fault potential and touch voltage in the low-voltage distribution line system of the residential community” Electric Power Systems Research, Volume 228, 2024.

- J. Cao, Y. Du, Y. Ding, Z. Li, M. Chen and R. Qi, "Performance Against Direct Lightning on 10-kV Overhead Distribution Lines With Counterpoise Wires," in IEEE Transactions on Electromagnetic Compatibility, vol. 65, no. 4, pp. 1108-1116, Aug. 2023, doi: 10.1109/TEMC.2023.3243734.

- J. Cao, Y. Du, Y. Ding, R. Qi, M. Chen, **Z. Li** and X. Zhao "Lightning Protection With a Differentiated Configuration of Arresters in a Distribution Network," in IEEE Transactions on Power Delivery, vol. 38, no. 1, pp. 409-419, Feb. 2023, doi: 10.1109/TPWRD.2022.3192482.

- J. Cao, Y. Du, Y. Ding, M. Chen, **Z. Li**, B. Li, & R. Qi. "Practical Schemes on Lightning Energy Suppression in Arresters for Transformers on 10 kV Overhead Distribution Lines," in IEEE Transactions on Power Delivery, vol. 37, no. 5, pp. 4272-4281, Oct. 2022, doi: 10.1109/TPWRD.2022.3148280.

- J. Cao, Y. Du, Y. Ding, B. Li, R. Qi, Y. Zhang, & **Z. Li**. "Lightning Surge Analysis of Transmission Line Towers With a Hybrid FDTD-PEEC Method," in IEEE Transactions on Power Delivery, vol. 37, no. 2, pp. 1275-1284, April 2022, doi: 10.1109/TPWRD.2021.3083324.

- J. Cao, Y. Du, Y. Ding, R. Qi, B. Li, M. Chen, & **Z. Li**. "Comprehensive Assessment of Lightning Protection Schemes for 10 kV Overhead Distribution Lines," in IEEE Transactions on Power Delivery, vol. 37, no. 3, pp. 2326-2336, June 2022, doi: 10.1109/TPWRD.2021.3110248.

- Y. Ding, Li, B., Du, Y. P., Chen, M., **Li, Z.**, & Zhao, Y. M. "Extended Traveling Wave Theory for the Multistage Tower Under a Direct Lightning Strike," in IEEE Transactions on Electromagnetic Compatibility, vol. 63, no. 3, pp. 830-839, June 2021, doi: 10.1109/TEMC.2020.3030413.

II. Papers in Conferences

- Z. Li, et al. "The Distribution of Ground Potential around Grounding grids under a Direct Lightning Strike," 2022 36th International Conference on Lightning Protection (ICLP), Cape Town, South Africa, 2022, pp. 272-275, doi: 10.1109/ICLP56858.2022.9942629.

- Z. Li, et al. "The Risk Analysis of Electric Shock in Different Grounding Systems." Journal of Physics: Conference Series. Vol. 2378. No. 1. IOP Publishing, 2022.

- Z. Li, et al. "Residential Electrical Fire in Shenzhen: Data Analysis and Possible Solution." 2021 IEEE/IAS 57th Industrial and Commercial Power Systems Technical Conference (I&CPS). IEEE, 2021.

- Z. Li, et al. "Electric Shock in Urban Village: Reflections from A Practical Accident." 2021 IEEE/IAS 57th Industrial and Commercial Power Systems Technical Conference (I&CPS). IEEE, 2021.

Acknowledgements

First and foremost, I wish to express my deepest gratitude to **Director Huang Huishan**, whose trust and guidance allowed me to lead the establishment of the Futian Bureau’s Low-Voltage Innovation Laboratory and subsequently a series of scientific projects on low-voltage safety. His vision and magnanimity have profoundly improved the safety environment for millions in this city, and fundamentally altered the trajectory of my own career. Indeed, all of my doctoral achievements can be traced back to this very starting point.

I am sincerely grateful to my supervisor, **Professor Du Yaping**, for giving me the opportunity to return to academia after years of professional work. Professor Du is not only a true mentor but also a craftsman in scholarship: a teacher of genuine capability, tireless patience, and rigorous dedication. His guidance has left an indelible mark on my life. Beyond academics, he also cared deeply about my well-being, often helping me manage insomnia and headaches during my doctoral journey. Every meeting or discussion with him would always bring me comfort and renewed strength. He is, in every sense, a warm and inspiring elder mentor.

My heartfelt thanks also go to my fellow lab members and brothers-in-arms, who became the greatest personal treasure of my PhD years. **Dr. Zhang Yang** stood by me from the application stage through project planning—we dreamed big, stumbled forward, traveled together across the world, shared doubts and struggles, and built unforgettable youthful memories. **Dr. Chen Hongcai**, my senior brother, was indispensable in every critical stage of delivery. Despite our jokes about his occasional rough logic, I will always respect his commitment and ability—his support made my work at the laboratory and my mid-term defense possible. **Dr. Ding Yuxuan**, my third senior brother, was the key factor in my completing this degree. If Chen embodied Professor Du’s diligence, Ding inherited his wisdom and generosity. He was like a mentor to many of us, always patiently explaining, and his selflessness laid much of the theoretical foundation of our group. **Dr. Cao Jinxing** impressed everyone with his unmatched output, despite his youthful zeal. **Dr. Zhou Qibin**, though he had graduated before I joined, still treated me like a younger brother and became a spiritual leader for many of us. **Dr. Lü Jiahua** and **Dr. Jia Chuanzhen** were my closest companions—smart, capable, and supportive both

academically and in life, with whom I also enjoyed countless joyful sports moments. To all other group members: though our interactions may have been briefer, I constantly felt the warmth and strength of belonging to this remarkable academic family.

I also owe special thanks to **Mr. Ma Nan**, **Mr. Qiu Fang Chi**, and **Mr. Li Rui**. Mr. Ma encouraged me to pursue the PhD in the first place—without him, I would never have even considered this path. A true idealist scholar, he patiently guided me in turning vague real-world problems into scientific questions, then into engineering solutions, and finally into real change. Working with him has been the most exciting and valuable time of my career so far. Mr. Fang not only devoted tremendous effort to supporting the laboratory's construction and promotion, but also cared deeply about my personal life—he is a reliable brother. Mr. Li, with foresight and strategic vision, advanced Hong Kong–Shenzhen scientific collaboration to new heights.

Finally, I would like to express my profound gratitude to my **family**. My parents and my partner gave me unwavering support in life throughout these demanding years. Above all, I wish to dedicate this doctoral degree to my grandfather, hoping that he finds joy in knowing that I have earned the first PhD in our family.

Table of Contents

1. Introduction

1.1 Background

As electrical distribution grids in residential areas continue to evolve, many older neighborhoods face significant challenges in ensuring the safety and reliability of their electrical systems. While modern distribution networks benefit from advancements in electrical engineering, older systems often rely on outdated infrastructure that lacks the necessary protective devices to effectively manage risks associated with electrical faults and transient overvoltages. Specifically, issues such as inadequate fault protection, insufficient grounding, and vulnerability to lightning-induced overvoltages pose significant safety concerns. These problems are further compounded by the difficulty of upgrading electrical systems in established buildings due to financial constraints and structural limitations.

This thesis focuses on the electromagnetic transient simulation methods for power distribution networks based on the Partial Element Equivalent Circuit (PEEC) approach, with a particular emphasis on lightning and fault analysis scenarios. The research addresses two key issues in electrical distribution grids: 1) lightning modeling and protection of tall structures, and 2) fault potential and touch voltage risks in low-voltage (LV) distribution systems.

1.1.1 Lightning modeling and protection of tall structures

In recent decades, the increasing deployment of tall infrastructure such as wind turbines, skyscrapers, broadcast towers, and telecommunication masts has significantly altered the landscape of power systems and urban development. While these structures support critical services and sustainable energy development, they are also highly susceptible to lightning strikes due to their physical height and exposed locations. Lightning, a natural but complex atmospheric discharge phenomenon, can inject currents of tens to hundreds of kiloamperes into these structures, often resulting in overvoltages that threaten the structural integrity of equipment, disrupt power delivery, and pose safety hazards to personnel.

The design of lightning protection systems for such structures traditionally follows empirical or simplified engineering models that are based on assumptions valid only for low-height installations or idealized ground conditions. These models often overlook the intricate physical processes involved in lightning discharge, particularly during the leader formation and attachment phase. In conventional approaches, the lightning channel is represented as a simple current source, and the interaction between the lightning and the protected structure is often treated in isolation. However, recent studies have shown that the dynamic behavior of the lightning leader, including the evolution of the corona sheath and its nonlinear interactions with the surrounding medium, significantly affects the electromagnetic fields induced in and around tall structures. The neglect of these effects leads to underestimation of peak overvoltages and ineffective design of critical protective components such as surge arresters, grounding electrodes, and bonding networks.

From a scientific perspective, modeling the lightning discharge process presents several challenges. The physical properties of the lightning channel—including its time-varying conductivity, expanding core radius, and corona charge distribution—are not uniform along its length and change rapidly during the discharge process. Moreover, the induced fields on nearby conductors are strongly influenced by the geometrical arrangement, grounding configuration, and frequency-dependent behavior of soil resistivity. Capturing these factors requires a multi-physics modeling approach that integrates electromagnetic theory with atmospheric discharge physics.

One of the key gaps in current research is the lack of integrated models that can simulate the interaction between a lightning channel and a tall structure in a way that reflects both the spatial distribution of charges and the dynamic behavior of the channel. Traditional models such as the transmission line (TL) model or the antenna theory (AT) model have certain advantages but are often limited in scope and accuracy when applied to complex geometries. Recent advancements in numerical methods, such as the Partial Element Equivalent Circuit (PEEC) method, provide promising avenues to simulate the full electromagnetic behavior of wire-based systems and grounding networks in the time domain, with realistic representations of physical parameters. When coupled with an improved model for the lightning channel that considers corona sheath evolution and nonlinear charge-potential relationships, these tools can significantly enhance our ability to evaluate and mitigate lightning-induced hazards.

From an engineering standpoint, the accurate prediction of transient overvoltages and the associated current paths is essential for the effective design of protection systems in wind farms, urban high-rises, and critical infrastructure. As wind turbines grow taller—often exceeding 150 meters in blade tip height—their probability of being struck by lightning increases, and so does the potential for insulation failure, control system malfunction, and grounding grid overload. Inadequate modeling of these events may lead to the deployment of protection schemes that are either insufficient or excessively conservative, resulting in either compromised reliability or unnecessary cost. Moreover, in the presence of poor soil conductivity or shallow grounding systems, the step and touch voltages arising from lightning strikes can exceed safe limits, posing a significant risk to maintenance personnel and nearby residents.

Thus, the need for a physically accurate and computationally efficient model that accounts for the mutual interaction between lightning channels and tall grounded structures is both urgent and highly practical. By incorporating nonlinear charge simulation, corona sheath dynamics, and detailed grounding structure modeling using hybrid TL–PEEC methods, a new class of simulation tools can be developed. These tools would not only improve the scientific understanding of lightning physics but also provide practical guidance for designing more resilient grounding and surge protection systems.

The research presented in this thesis contributes to this goal by proposing a nonlinear charge simulation method (NCSM) for downward negative leaders and integrating it with a hybrid TL–PEEC framework. This approach enables the analysis of lightning-induced transient responses in tall structures with unprecedented physical fidelity. By bridging the gap between physical modeling and engineering application, the work advances the state-of-the-art in lightning protection system design and provides essential insights into the safe and reliable operation of tall infrastructure under severe atmospheric conditions.

1.1.2 Fault potential and touch voltage risk in LV distribution systems

With the increasing complexity and aging of urban infrastructure, electrical safety in LV distribution systems has become an urgent and multifaceted issue, particularly in older residential communities. These communities, often developed decades ago, are typically equipped with outdated wiring layouts, inadequate grounding measures, and protective devices that no longer meet modern safety standards. The rapid urban expansion in regions such as Southeast Asia and Southern China has led to the emergence of densely populated urban villages and informal housing clusters where the electrical systems are neither standardized nor regularly maintained. In such environments, the risk of electric shock resulting from grounding faults, insufficient equipotential bonding, and line interruptions remains alarmingly high.

Electric shock incidents in LV networks can result from a variety of fault scenarios, including phase-to-ground faults, line-to-neutral faults, and neutral-line disconnections. In each of these cases, a dangerous fault potential may develop across exposed conductive parts such as water heaters, household appliances, and building frameworks. If the human body comes into contact with these conductive surfaces while simultaneously connected to the ground (e.g., by standing barefoot on a concrete floor), a hazardous touch voltage may be induced across the body, potentially leading to severe injury or even fatality. These risks are exacerbated in residential areas where protective devices such as Residual Current Devices (RCDs) are either absent or have become unreliable due to equipment aging or improper installation.

Traditional safety strategies for LV systems rely on automatic disconnection of supply during fault events and proper implementation of equipotential bonding. However, in aging neighborhoods, several constraints limit the practical application of these protective measures. Firstly, the cost and complexity of retrofitting outdated electrical systems are often prohibitive, especially in economically disadvantaged communities. Secondly, building structures constructed decades ago may not have been designed with a dedicated protective earth (PE) conductor or modern grounding schemes. Finally, informal or unauthorized electrical modifications, which are common in urban villages, further complicate the situation by introducing inconsistencies and safety hazards into the distribution network.

Grounding configuration plays a central role in determining the electrical safety of LV systems. Commonly adopted configurations such as TT (Terra-Terra), TT(M)-C-S (multi-grounded TT with common-neutral bonding), and TX(M)-C-S (hybrid TN-C-S system with multiple grounding points) differ in how the neutral and protective earth conductors are arranged and grounded. These variations directly affect fault current paths, grounding impedance, and ultimately the resulting touch voltage at different locations throughout the network. However, a detailed comparison of these configurations under real-world fault conditions, especially in deteriorating infrastructure, is lacking in the literature. Engineering standards provide general guidelines, but do not offer clear quantitative evaluations of the fault potential distribution or the risk levels for specific grounding topologies in aged systems.

From a scientific standpoint, the accurate prediction of touch voltage and fault potential requires an electromagnetic model capable of capturing the distributed nature of conductors, grounding electrodes, soil resistivity, and even building foundations. Traditional circuit-based models fall short in this respect due to their oversimplified representations of physical structures. Finite Element Method (FEM) and Boundary Element Method (BEM) approaches offer more detailed modeling capabilities but are often limited by computational costs when applied to complex distribution systems. In contrast, the Partial Element Equivalent Circuit (PEEC) method has emerged as a powerful and versatile modeling technique that can represent complex conductor geometries, incorporate frequency-dependent ground parameters, and simulate transient electromagnetic behavior in the time domain. By applying PEEC to residential LV networks, it becomes possible to accurately quantify the impact of grounding design and structural configuration on safety-related parameters.

The role of building materials and embedded conductors, such as steel reinforcement in concrete (rebars), in fault current dissipation is equally important. These structural elements, although not originally designed for electrical purposes, can influence the current return path during an electric shock event. When rebars are unintentionally energized or bonded to grounded components, they may serve as alternate current paths, affecting both the distribution of fault potential and the touch voltage experienced by residents. The lack of standardized practices regarding the bonding of such elements introduces significant variability and uncertainty in safety assessments.

This research addresses both engineering and academic challenges in evaluating and mitigating fault potential and touch voltage risks in LV distribution systems. It focuses on (1) modeling the performance of typical grounding configurations in aging residential networks, (2) assessing the role of structural conductors such as rebars in current distribution during fault conditions, and (3) proposing practical grounding strategies that can enhance safety without requiring large-scale infrastructural overhauls. A simulation framework based on the PEEC method is developed to analyze the influence of fault location, grounding configuration, soil resistivity, and structural layout on fault potential and touch voltage.

By combining field measurements, practical case studies, and advanced numerical modeling, this research contributes to the development of safer, more resilient LV distribution systems in real-world urban environments. The findings are particularly relevant to policymakers, utility companies, and engineers tasked with upgrading or maintaining electrical infrastructure in aging or economically constrained residential areas. Ultimately, this work supports the broader goal of reducing electrical hazards and improving the quality of life in vulnerable communities through informed, technically grounded design decisions.

1.2 Objectives

This thesis aims to address the following two issues:

(1) Lightning Modeling and Protection of Tall Structures

The primary focus of this issue lies in enhancing the accuracy and reliability of lightning modeling and protection systems, which are crucial for safeguarding tall structures and distribution networks from the potentially catastrophic effects of lightning strikes. As infrastructure continues to grow taller and more complex, and as lightning-induced surges increase in frequency and intensity, effective lightning protection and fault mitigation systems are becoming more important. The first objective addresses the need for a better understanding of the charge dynamics in lightning strikes, while the second objective focuses on accurately representing the interaction between lightning channels and tall structures. Both objectives are essential for bridging theoretical lightning models with practical engineering applications, improving the safety and operational reliability of modern electrical systems exposed to lightning strikes.

Objective 1: Development of a Nonlinear Charge Simulation Method for Lightning Leader Dynamics.

The first objective of this research is to develop a nonlinear charge simulation method that accurately models the temporal and spatial charge evolution in the leader stage of downward negative lightning. Lightning is a highly complex, nonlinear phenomenon, and traditional models often fail to account for the intricate and dynamic interactions between the cloud, the leader channel, and the ground. By incorporating time-variant and nonlinear corona effects into the simulation, this method will provide a more precise representation of the charge distribution during lightning strikes. This will allow for a better understanding of the electric field dynamics that occur as the lightning leader propagates toward the ground.

The key contribution of this objective is the development of a realistic model that closely aligns with experimental observations of lightning charge distribution, which is critical for improving the design of lightning protection systems. The insights gained from this work will be instrumental in refining lightning protection strategies, particularly for tall structures and sensitive infrastructure. A more accurate simulation of the lightning leader's behavior will enhance the ability to predict lightning-induced transients and improve the performance of protective measures such as surge arresters and grounding systems.

Objective 2: Development of an Integrated Model for Lightning Strikes Tall Structures.

The second objective of this research is to develop an integrated model that accurately represents the interaction between a lightning channel and tall structures, such as wind turbines, high-rise buildings, and communication towers. This objective focuses on the limitations of existing models, which often treat the lightning channel as a simple current source and fail to account for the dynamic behavior of the lightning channel and its interaction with the surrounding structure. By employing a modified transmission line (TL) model for the lightning channel and the Partial Element Equivalent Circuit (PEEC) method for the structure, this model will provide a comprehensive and accurate representation of lightning-induced currents and electromagnetic fields in tall structures.

The primary contribution of this objective is to overcome the simplifications of traditional models by incorporating the nonlinear, non-uniform characteristics of the lightning channel and the corona sheath, which can significantly affect the induced lightning currents in tall structures. By doing so, this research will provide a more accurate and reliable tool for designing lightning protection systems that better protect critical infrastructure from lightning-induced damage. This integrated model will be especially useful for the design of wind turbine protection systems, where the size and frequency of lightning strikes make traditional approaches insufficient.

Together, these two objectives address critical gaps in current lightning protection research and practice. The development of a nonlinear charge simulation method and the integration of more sophisticated models for tall structures will provide a more accurate, physically grounded approach to understanding and mitigating lightning-induced hazards. This research will not only improve theoretical lightning models but also contribute directly to the engineering design of safer, more resilient infrastructure, particularly in high-risk areas where lightning strikes are frequent and intense. These advancements will have a profound impact on the design and reliability of lightning protection systems, ensuring the continued safety of both equipment and people exposed to the dangers of lightning.

(2) **Fault Potential and Touch Voltage Risk in Low-Voltage Distribution Systems**

The second key issue addressed by this research focuses on evaluating and improving the safety of LV distribution systems in aging residential communities, particularly in terms of fault potential and touch voltage risks. As many older neighborhoods continue to rely on outdated electrical systems, these infrastructures face significant vulnerabilities, especially during fault conditions. Inadequate grounding, outdated protective devices, and aging network components can lead to unsafe conditions, putting residents at risk of electric shock. The following two objectives outlined in this issue aim to fill critical gaps in understanding the impact of these system deficiencies and to provide practical solutions for improving safety. By using advanced simulation techniques like the PEEC method, this research seeks to accurately quantify fault potentials and touch voltages under various fault scenarios, offering evidence-based insights for enhancing grounding configurations and mitigating electric shock risks.

Objective 3: Evaluate Fault Potential and Touch Voltage in Low-Voltage Networks Using the PEEC Method

The first objective of this research is to evaluate and analyze fault potential and touch voltage in low-voltage distribution networks under various fault conditions in old residential communities using the Partial Element Equivalent Circuit (PEEC) method. This objective seeks to quantify the fault potentials and touch voltages that arise from different fault scenarios, such as phase-to-ground and line-to-neutral faults, within the context of outdated electrical systems. The PEEC method will be applied to simulate the interactions between grounding configurations, fault currents, and structural elements like reinforced concrete, which are common in older buildings. These simulations will help to understand how different fault conditions affect the safety of residents, especially when grounding systems are suboptimal or non-compliant with modern safety standards.

The primary contribution of this objective lies in providing a detailed and comprehensive analysis of fault potentials and touch voltages that occur in real-world, aging low-voltage distribution systems. By using the PEEC method, which accurately represents complex conductor geometries and grounding configurations, this research will offer quantitative insights into the magnitude of electrical hazards that residents may face during fault events. The results will inform the design of more reliable grounding systems and contribute to the development of safer electrical networks, especially in older residential communities where the retrofitting of modern protective devices may be challenging or cost-prohibitive. This objective will provide practical solutions for evaluating and mitigating risks, improving public safety, and ensuring compliance with evolving electrical safety standards.

Objective 4: Assess the Effectiveness of Grounding Configurations and Protective Measures in Outdated LV Systems

The second objective is to assess the effectiveness of existing grounding configurations and protective measures in mitigating touch voltage risks in outdated low-voltage electrical systems. This research will evaluate the safety performance of various grounding configurations, including TT, TT(M)-C-S, and TX(M)-C-S, in residential communities with aging electrical infrastructures. These systems often lack modern protective devices, making them particularly vulnerable to faults. The research will also explore potential improvements to grounding methods and propose recommendations for reducing electric shock risks, especially in scenarios where it is impractical or impossible to retrofit modern protective devices like residual current devices (RCDs).

The primary contribution of this objective is to provide a thorough evaluation of the effectiveness of different grounding configurations in mitigating electric shock risks in old residential areas. By studying the performance of grounding systems in real-world scenarios, this research will identify which configurations offer the best protection and where improvements can be made. Additionally, the research will propose new or modified grounding methods to address gaps in current safety practices, especially in environments where retrofitting modern devices is not feasible. These findings will be directly applicable to electrical engineers and urban planners, offering practical, cost-effective solutions to improve safety in aging electrical networks. This objective contributes to the broader goal of enhancing public safety and ensuring that low-voltage distribution systems continue to meet evolving safety standards, even in challenging or resource-limited environments.

1.3 Thesis Outline

In Chapter 2, the author proposes a leader charge simulation method to reproduce the spatial and temporal charge distribution in the lightning leader process. The method considers cloud, channel, and ground charges in a unified NCSM framework, introducing a charge-dependent potential coefficient driven by corona sheath evolution based on experimental observations. The method was experimentally validated by comparing electric field results at various distances. Using this approach, charge distribution density across different lightning conditions can be calculated, providing insights into the relationship between lightning parameters and leader channel charge density. The inclusion of the corona effect yields more accurate simulation results.

In Chapter 3, the author proposes an integrated model for analyzing the interaction between the lightning channel and tall structures, accounting for the dynamic corona sheath behavior and non-linear characteristics of the lightning channel. The Partial Element Equivalent Circuit (PEEC) method is used for modeling the ground wire structure, with a lumped voltage source ensuring accurate current waveforms. The model, validated with experimental data, is applied to simulate lightning surges on wind turbines, revealing that the simple current source model produces unrealistic oscillations compared to actual lightning observations.

In Chapter 4, the modeling of the grounding system in the Low-Voltage Distribution Line System is proposed. The author investigates fault potential and human-body touch voltage in low-voltage distribution networks of old residential communities, focusing on three protective grounding configurations. This study finds that the phase-to-ground fault potential increases with proximity to the fault location, and bonding non-exposed steelwork to a nearby grounded grid effectively reduces touch voltage.

In Chapter 5, the conclusion and future work.

2 A Downward Negative Leader Model Considering both Nonlinear and Time-variant Behavior

2.1 Introduction

Lightning strikes represent a significant threat to modern infrastructure due to their ability to induce high currents and voltages, potentially causing severe damage to electrical systems, equipment, and even human lives. As urbanization and reliance on electronic systems grow, accurate modeling of lightning behavior becomes critical to designing effective protection systems. Among the most challenging aspects of lightning modeling is the downward negative leader (DNL), the initial discharge phase where the lightning propagates from the cloud to the ground. This stage plays a crucial role in determining the lightning strike's intensity and impact. Therefore, a more precise understanding of the leader's behavior, including the complex interactions between cloud charges, the leader channel, and the ground, is necessary for improving lightning protection strategies.

Negative cloud-to-ground lightning flashes are of the most concern in both engineering applications and academic research. These flashes start with a negative downward leader, initiated from the bottom of a cloud. The evolving downward leader propagates toward the ground and distributes the negative charge from the cloud to the leader channel. Meanwhile, by induction, the positive charge on the ground is concentrated near the channel. A charge structure consisting of the cloud, channel, and ground charges is then formulated. These charges play an important role in the leader's evolution.

The cloud is usually constructed as a three-layer structure in the simulation [1]. The top two layers have the same amount of charge but opposite charge polarity and are the major part of the cloud. They are often simplified as a dipole structure with a point, plane, or spherically symmetrical volume charge [2]. The bottom layer has a small amount of positive charge and is not always present. The height of the cloud bottom above the ground varies from 2 km to 10 km [3] and the cloud top can reach an altitude of up to 20 km [4]. The cloud radius is normally within the range of 2-6 km [14]. The magnitude of the main charge is in the range of 20 C to 120 C [5].

The channel charge, which is a crucial factor in determining lightning return stroke parameters, can be simulated numerically with a leader channel model. Research related to lightning leader channel modeling has been conducted for more than decades. The leader progression model (LPM) was first proposed in [12,13], in which the lightning leader channel was modeled as a charged line segment. The leader charge was then calculated by the charge simulation method (CSM). Since then, a lot of academic research has been conducted for further development of leader progression model [15-20]. The revised models were applied to study the shielding failure of transmission lines [21-22]. Similar approaches were proposed by Risk [23-24] for lightning channel modeling and simulation. In [25] a simplified physical model was proposed by M. Becerra to simulate the leader propagation for determining the upward connecting leader inception. To include the effect of corona charge, a charged ring with a uniformly distributed charge is adopted to represent the corona sheath in the simulation and the charge per unit length in the channel is assumed to be a pre-given constant [26]. Until now the cloud volume charge and ground surface charge have not been included in the CSM. The time-and-space-variant and nonlinear effects of the corona sheath have not been considered either. Thus, a new mathematical model would become necessary to bridge the physical mechanisms and engineering applications.

The charge on a lightning channel varies with time and space in the downward leader stage. It will cause the breakdown of air around the channel core. The charge will be then redistributed in the space. Thus, the leader channel can be represented by a thin core surrounded by a radially formed corona sheath, where the bulk of the corona charge is stored [6]. The corona sheath radius is of the order of meters [6] while the channel core radius ranges from 0.1 cm to 1.49 cm [11]. The breakdown electric field for negative breakdown is normally assumed to be of magnitude from 0.5 MV to 3 MV [7-9] and to be height-variant [8] and time-variant [9]. The leader charge is most likely in the range of 5 C to 15 C and is found to be proportional to the channel length [8]. It is shown in [10] that given the charge distribution in the cloud, the charge distribution in the leader channel is uniquely determined.

Most recently, the physical evolution of the corona sheath has been elaborately studied [27-31]. During the leader stage, the negative breakdown zone is expanded outward and finally formed with the bulk of the negative space charge. In the subsequent return-stroke process, the corona sheath is composed of two zones, the outer zone with the negative charge and the inner zone with mixed positive and negative charges. Cooray [33] proposed the corona sheath model in a coaxial geometry which is in high coincidence with experiments using coaxial cylindrical electrodes. It was then widely applied in the lightning return stroke simulation [34-36]. However, in a lightning flash, the channel does not have an outer conductor or a current-return path. This may differ from the coaxial cylindrical structure used in the laboratory. Meanwhile, the length of the lightning channel is normally several kilometers and the lightning current varies from several kA to more than a hundred kA. The strong nonlinearity of some channel parameters has not been considered. Kuma [37] proposed a macroscopic model for the return stroke and Chen [38] developed it into a leader-return-stroke model by including the initial condition before the attachment. In their models, the core charge is transferred from the core directly to the corona outer boundary with a relaxation time in the leader stage. This is, to some extent, similar to an electrode buried underground, where the charge is transferred from the electrode to infinity with a relaxation time. With the recent advances in the corona sheath physical research and electromagnetic simulation modeling, a more dedicated leader channel corona model, which provides a solution for the charge movement considering time-variant behavior and nonlinearity, is proposed in this thesis.

In this section, we present a downward negative leader (DNL) model before the attachment by incorporating the cloud volume dipole charge, leader channel corona charge, and ground surface charge. The nonlinear corona expansion is modeled by introducing a charge-dependent potential coefficient. The nonlinear charge simulation method (NCSM) with the Gaussian-Seidel iteration at each time step is proposed to solve the spatial and temporal charge distribution in the lightning leader stage. The model is validated by comparing the simulation results with experimental observation results. All the physical parameters adopted in the numerical simulation are collected from the literature.

This method is valuable for studying the spatiotemporal evolution of the leader charge under the strong nonlinear effects of the lightning channel, providing a foundational model for research into the nonlinear physical mechanisms of lightning channels. By applying this model to the leader stage of the lightning channel, it allows for the determination of the charge spatial distribution characteristics before the attachment, offering essential initial charge distribution conditions for the lightning return stroke model presented in Section 3.

2.2 Nonlinear Charge Simulation Method (NCSM)

In this section, the traditional charge simulation method is expanded by including the nonlinear evolution of the corona sheath around the channel core. By giving the initial condition, which includes the size and the potential of the thundercloud as well as the initial channel core radius, the temporal and spatial evolution of the leader channel can be numerically simulated.

Fig. 2-1 shows a typical DNL process. The DNL propagates towards the ground with its tip height $h_{tip}(t)$ at time t. Suppose that $\boldsymbol{Q}_{cl}$, $\boldsymbol{Q}_{ch}$ are respectively the charge on the cloud and leader channel, $\boldsymbol{P}_{cl}$, $\boldsymbol{P}_{ch}$ are the corresponding potential coefficients, and $\boldsymbol{P}_{m}$ is the mutual potential coefficient between them. The relationship between the potential and charge then is given, as follows:

$$\begin{bmatrix} \mathbf{P}_{cl} & \mathbf{P}_{m} \\ \mathbf{P}_{m} & \mathbf{P}_{ch} \end{bmatrix} \begin{bmatrix} \mathbf{Q}_{cl} \\ \mathbf{Q}_{ch} \end{bmatrix} = \begin{bmatrix} \boldsymbol{\Phi}_{cl} \\ \boldsymbol{\Phi}_{ch} \end{bmatrix} \tag{2-1}$$

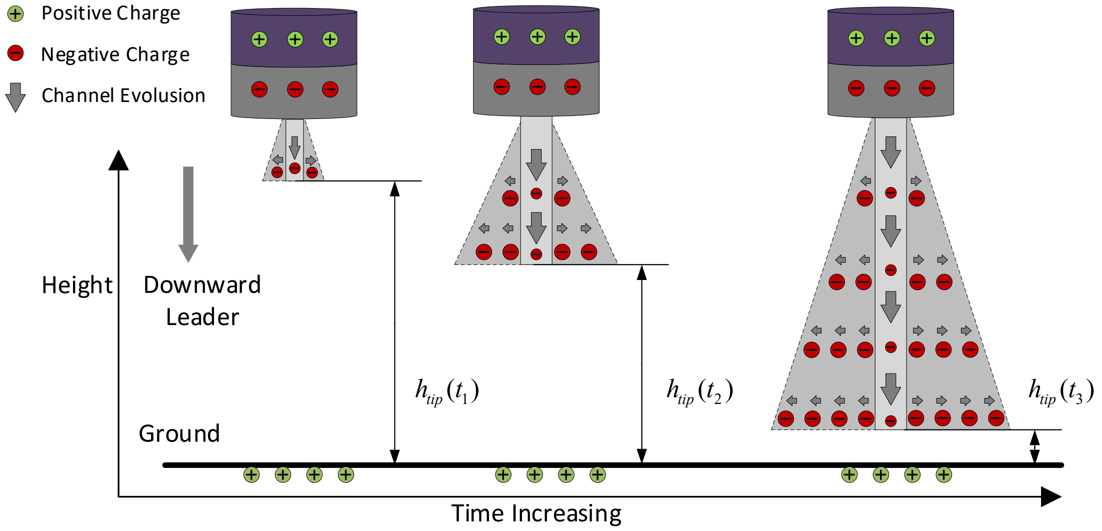

Fig.2-1 The leader channel evolution over time

where $\boldsymbol{\Phi}_{cl}$ and $\boldsymbol{\Phi}_{ch}$ are respectively the potentials of the cloud and leader channel. The cloud is modeled as a two-layer cylindrical volume structure as shown in Fig. 2-1. The lower layer starts from height h_b to h_m and the higher layer from h_m to h_t. The cloud potential is known in advance as $\boldsymbol{\Phi}_{cl} = [\phi_{cl,+}\ \phi_{cl,-}]^{t}$ ($\phi_{cl,+} = \phi_{cl,-}$).

The charges on the two layers of the cloud are denoted by $\boldsymbol{Q_{cl}} = \left[Q_{cl,+}\ Q_{cl,-}\right]^{\boldsymbol{t}}$, and are assumed to be uniformly distributed.

The leader channel is divided into N segments along its height and each segment is physically represented by a frustum of the cone. With the point-matching approach, (2-1) is expanded for charges in cloud $Q_{cl,+}\ Q_{cl,-}$ and in channel segments $Q_{ch,j}$ as follows:

$$\begin{bmatrix} P_{cl,++} & P_{cl,+-} & P_{cl+,ch1} & \cdots & P_{cl+,chn} \\ P_{cl,-+} & P_{cl,--} & P_{cl-,ch1} & \cdots & P_{cl-,chn} \\ P_{ch1,cl+} & P_{ch1,cl-} & P_{ch,11} & \cdots & P_{ch,1N} \\ \vdots & \vdots & \vdots & \ddots & \vdots \\ P_{chN,cl+} & P_{chN,cl-} & P_{ch,N1} & \cdots & P_{ch,NN} \end{bmatrix} \begin{bmatrix} Q_{cl,+} \\ Q_{cl,-} \\ Q_{ch,1} \\ \vdots \\ Q_{ch,N} \end{bmatrix} = \begin{bmatrix} \phi_{cl,+} \\ \phi_{cl,-} \\ \phi_{ch,1} \\ \vdots \\ \phi_{ch,N} \end{bmatrix} \qquad (2\text{-}2)$$

The potential $\phi_{ch,j}$ of channel segment j can be obtained by the potential at the cloud bottom $\Phi_{cl,-}$ and the longitude DNL electric field E_{DL}, as follows:

$$\phi_{ch,j} = \phi_{cl,-} + E_{DL}(h_b - h_j) \qquad (2\text{-}3)$$

where $(j = 1,2,3,\ldots,N)$ and h_j is the height of the middle point of the jth segment. In each segment of the channel, the relationship between electric field and current can be written as: $E_{DL}I_{DL} = C_b$, where C_b is equal to 3×10^4 determined from laboratory experiments [41]. The DNL current I_{DL} is evaluated by the product of current density $J_{DL} = \sigma_c E_{DL}$ and the core cross-sectional area $s_c = \pi r_{core}^2$. Thus, $\phi_{ch,j}$, is uniquely determined by (2-3) if core radius is given.

The mutual potential coefficient P_{ji} between cylindrical segments i and j in the air is shown below:

$$P_{ji,air} = \frac{\phi_{ji}}{Q_i} = \frac{\int_0^{2\pi}\int_0^{r_i}\int_{h_i-\Delta h/2}^{h_i+\Delta h/2} \rho_i(r',\theta',h')G(r_j,\theta_j,h_j,r',\theta',h')r'dr'd\theta'h'}{\int_0^{2\pi}\int_0^{r_i}\int_{h_i-\Delta h/2}^{h_i+\Delta h/2} \rho_i(r',\theta',h')r'dr'd\theta'dh'} \qquad (2\text{-}4)$$

where ϕ_{ji} is the potential at the middle point of segment i contributed by the charge Q_i on segment j in the air. r' is the radial distance and θ is the azimuth angle. r_i and r_j are respectively the radius of segments i and j. $G(r,\theta,h,r',\theta',h')$ is the Green's function. ρ_i is the charge density of segment i. In this method, the ground surface charge is substituted with a mirror image under the ground [43]. The potential coefficient for the image charge is evaluated by simply replacing the position of Green's function in (4) from height h to $-h$.

$$P_{ji,image} = \frac{\phi_{ji}}{Q_i} = \frac{\int_0^{2\pi} \int_0^{r_i} \int_{h_i-\Delta h/2}^{h_i+\Delta h/2} \rho_i(r',\theta',h') G(r_j,\theta_j,h_j,r',\theta',-h') r'dr'd\theta'h'}{\int_0^{2\pi} \int_0^{r_i} \int_{h_i-\Delta h/2}^{h_i+\Delta h/2} \rho_i(r',\theta',h') r'dr'd\theta'dh'} \tag{2-5}$$

The total potential coefficient P_{ji} between segments j and i will then be equal to $P_{ji,air} - P_{ji,image}$.

Once the electric field surrounding the core exceeds the breakdown electric field of the air E_b, the charge will be redistributed at the core and the nearby air due to the corona effect. Potential coefficient $P_{ch,ji}$ between channel segments i and j will then be expressed with core charge $Q_{core,i}$ and corona charge $Q_{corona,i}$, as follows:

$$P_{ch,ji} = \frac{Q_{core,i} P_{core,ji} + Q_{corona,i} P_{corona,ji}}{Q_{core,i} + Q_{corona,i}} \tag{2-6}$$

where potential coefficients $P_{core,ji,air}$ and $P_{corona,ji,air}$ are defined as

$$P_{core,ji,air} = \frac{\int_0^{2\pi} \int_0^{r_{core,i}} \int_{H-\Delta h/2}^{H+\Delta h/2} \rho_{core}(r',\theta',z') G(r,\theta,z,r',\theta',z') rdrd\theta dz}{Q_{core,i}}$$

$$P_{corona,ji,air} = \frac{\int_0^{2\pi} \int_{r_{core,i}}^{r_{corona,i}} \int_{H-\Delta h/2}^{H+\Delta h/2} \rho_{corona,i}(r',\theta',z') G(r,\theta,z,r',\theta',z') rdrd\theta dz}{Q_{corona,i}}$$

The charges on the core and corona sheath can be obtained by integrating these volume densities $\rho_{core,i}$ on the core and $\rho_{corona,i}$ on the corona sheath. Similar expressions can be obtained for $P_{core,ji,image}$ and $P_{corona,ji,image}$.

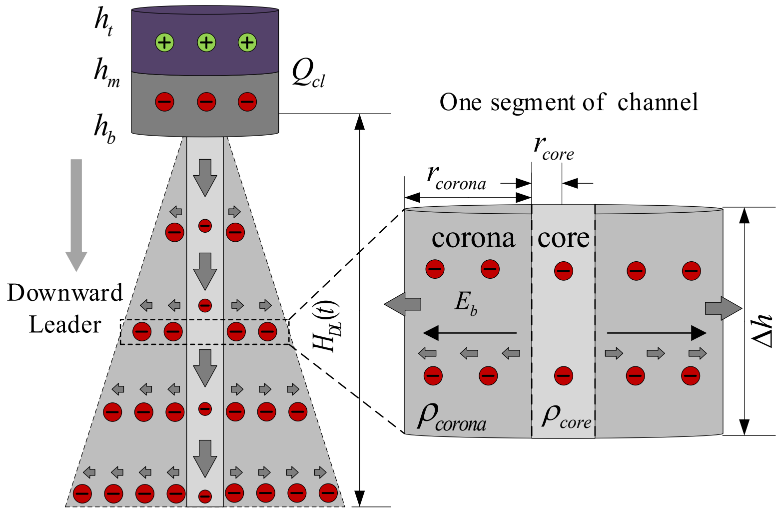

Fig.2-2 The discretized segment of a lightning channel

The electric field inside the core ($r < r_c$) is neglected and that inside the corona sheath ($r_c \leq r \leq r_s$) is assumed to be a pre-set breakdown field E_b in charge simulation[33]. Then, the core charge can be determined with Gaussian's flux theorem $\varepsilon\nabla \cdot (E\vec{\boldsymbol{a}}_r) = \rho$ on the surface of the core, i.e., $Q_{core,i} = 2\pi E_b r_{c,i}$. By assuming constant density on the surface of the channel core, the core charge density is expressed by:

$$\rho_{core,i}(r,\theta,z) = \varepsilon E_b \delta(r - r_{core,i}) \tag{2-7}$$

Where δ(r) is the Dirichlet function. The corona charge volume density can be determined in a similar way inside the corona, i.e.,

$$\rho_{corona,i}(r,\theta,z) = \varepsilon\nabla \cdot (E_b \vec{\boldsymbol{a}}_\rho) = \frac{\varepsilon E_b}{r} \tag{2-8}$$

which varies with radial distance in the corona sheath.

Note that the outer radius of the corona sheath is dependent on the total charge by using Gaussian's flux theorem $\varepsilon\nabla \cdot (E\vec{\boldsymbol{a}}_r) = \rho$ on the surface of the corona zone, and is expressed by

$$r_{corona,i} = \left(Q_{core,i} + Q_{corona,i}\right)/2\pi\varepsilon E_b \tag{2-9}$$

This leads to a nonlinear effect and potential coefficients can be finally expressed with charges on both the core and corona. The formulated nonlinear CSM equation in (2) will be solved by the Gauss-Seidel iterative technique.

The Gauss-Seidel iterative technique is applied to solve (2-1) or (2-2) in the expanded form, as follows:

$$\mathbf{Q}^{(k+1)} = \mathbf{L}^{-1}(\mathbf{\Phi} - \mathbf{U}\mathbf{Q}^{(k)}) \tag{2-10}$$

where, **L** and **U** are the lower and upper triangular components of the potential coefficient matrix $\mathbf{P}_{ch}$, and is expressed by

$$\mathbf{L} = \begin{bmatrix} P_{11} & 0 & \cdots & 0 \\ P_{21} & P_{22} & \cdots & 0 \\ \vdots & \vdots & \ddots & \vdots \\ P_{n1} & P_{n2} & \cdots & P_{nn} \end{bmatrix}, \quad \mathbf{U} = \begin{bmatrix} 0 & P_{12} & \cdots & P_{1n} \\ 0 & 0 & \cdots & P_{2n} \\ \vdots & \vdots & \ddots & \vdots \\ 0 & 0 & \cdots & 0 \end{bmatrix} \tag{2-11}$$

The elements of these matrices are evaluated with (2-6).

The calculation procedure is illustrated in Fig.4. Firstly, at each time step in the leader stage, potential $\mathbf{\phi}^{(0)} = [\mathbf{\phi}_{cl}^{*}\ \mathbf{\phi}_{ch}^{(0)}]^{\mathbf{t}}$ is calculated in advance using (2-3) with a pre-given $\mathbf{\phi}_{cl}^{*}$. Then, the initial charge $\mathbf{Q}^{(0)}$ is calculated using $\mathbf{\phi}^{(0)}$ and potential coefficient $\mathbf{P}_{ch}$ without any corona effect, that is,zero thickness for the corona sheath. Next, the corona radius $\mathbf{r}_{corona}$ is calculated with (2-9) using the initial charge $\mathbf{Q}^{(0)}$. Potential coefficient $\mathbf{P}_{ch}$ with the corona effect then is evaluated through (2-6). By using the Gauss-seidel iterative technique in (2-10), the charge is updated into $\mathbf{Q}^{(k+1)}$. Potential $\mathbf{\phi}^{(k+1)}$at the k+1th iteration can be obtained by (2-2). If the error between $\mathbf{\phi}^{(k+1)}$ and the given potential $\mathbf{\phi}^{(0)}$, the iteration process is terminated.

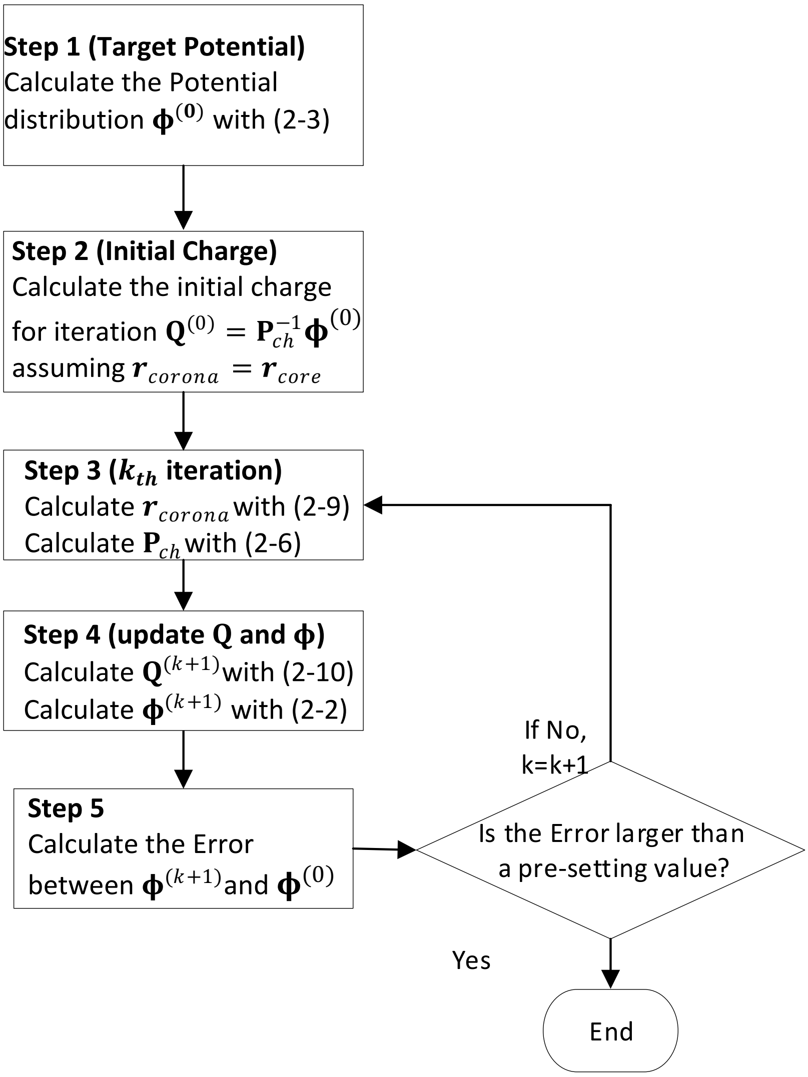

Fig.2-4 Flowchart of the calculation procedure

2.3 Numerical Simulation Results and Discussion

In this section, the electric field induced by a lightning leader channel is calculated with the proposed model. In the simulation, a two-layer cloud is situated at a height of 6 km above the ground, and the depth of each layer is 3 km ($h_b = 6\ km$, $h_m = 9\ km$, and $h_t = 12\ km$). The cloud radius is 2 km and the cloud potential is 10 MV. The breakdown electric field is set to be 2 MV/m The channel core radius is 5 mm and core conductivity is $2 \times 10^4\ S/m$. The tip of the leader channel propagates from 6 km to the attachment height above the ground with the propagation velocity of 10^7m/s. The height of the attachment is set to be 40m above the ground. The channel is discretized with a segment length of 20 m and has 298 segments in total. The propagation velocity of the leader channel is set to be 10^7 m/s. The maximum simulation time is 596 μs and the time step is set to be 2 μs. The electric field before the attachment is calculated with the expressions in [39] at the distances of 10 m, 20 m, 30 m, 50 m, 110 m, and 500 m from the striking position. The results are compared with the experimental observation results in [40]. Fig. 2-5 shows the electric fields both calculated and measured [40] at these distances during the leader stage. The propagation velocity of the leader channel is set to be 10^7m/s. Table 1 shows both the measured and calculated changes of the electric field for comparison. It is found that these electric field waveforms match very well. The average difference of the electric field change in the leader stage is less than 15%.

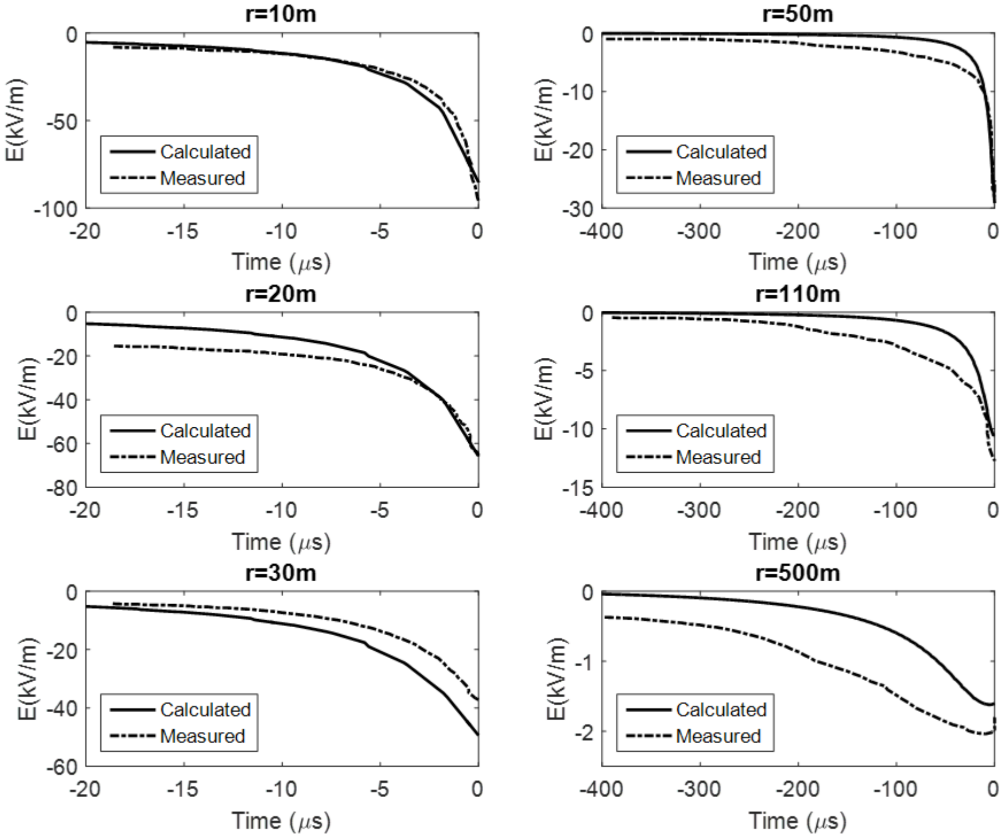

Fig.2-5 Measured and calculated electric fields at the distances of 10 m, 20 m, 30 m, 50 m,110 m, and 500 m from the lightning striking position

Table.2-1 Comparison of the electric field change by measurement and simulation

DISTANCE	MEASURED E FIELD	CALCULATED E FIELD
10	79.92	85.46(6.48%)
20	60.58	50.27(20.5%)
30	43.7	33.22(24.6%)
50	28.01	25.75(8.76%)
110	10.42	12.13(14.08%)
500	1.52	1.56(2.56%)

Charge density along the channel is shown in Fig. 6. Curves 1, 2, 3, and 4 are the charge density when the leader tip arrives at the height of approximately 0 m, 1 km, 2 km, and 3 km, respectively. It is found that the charge density increases approximately linearly from the bottom of the cloud toward the leader tip. At the leader tip, the charge density starts to increase sharply. This is similar to Cooray's suggestion in [41].

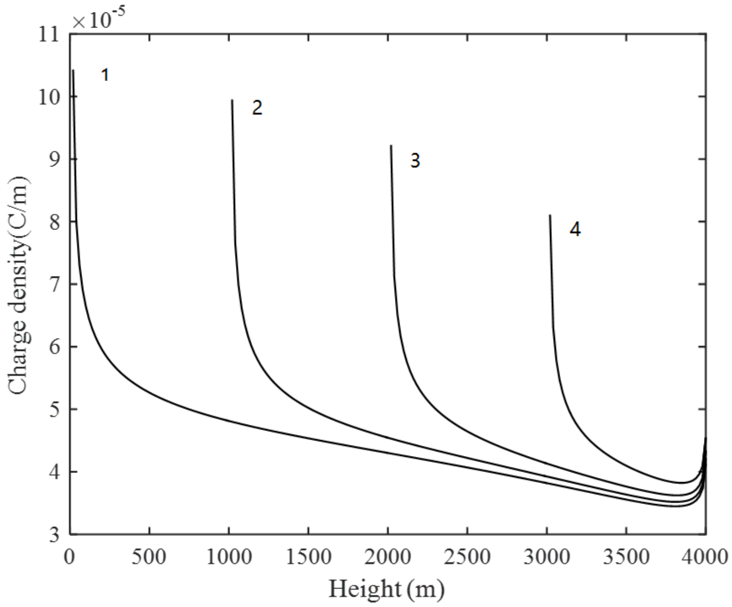

Fig. 2-6 Charge density evolution along the leader channel

A further study was performed on the relationship between the charge density and the channel physical parameters, such as channel core radius, channel height, breakdown field, and cloud potential. In each case, one of these parameters is varied, and others remain unchanged. The configuration presented early in this section is adopted as the reference configuration. In the simulation, the core radius varies from 1 mm to 10mm. The cloud top $\mathbf{h_t}$ varies from 5 km to 8 km, while the cloud bottom $\mathbf{h_b}$ is fixed to be 4 km above the ground. The negative breakdown electric field varies from 1 MV/m to 3 MV/m. The cloud potential varies from 20 MV to 80 MV. Fig.

2-7 shows the influence of channel core radius, cloud size, breakdown field, and cloud potential on the charge distribution along the leader channel.

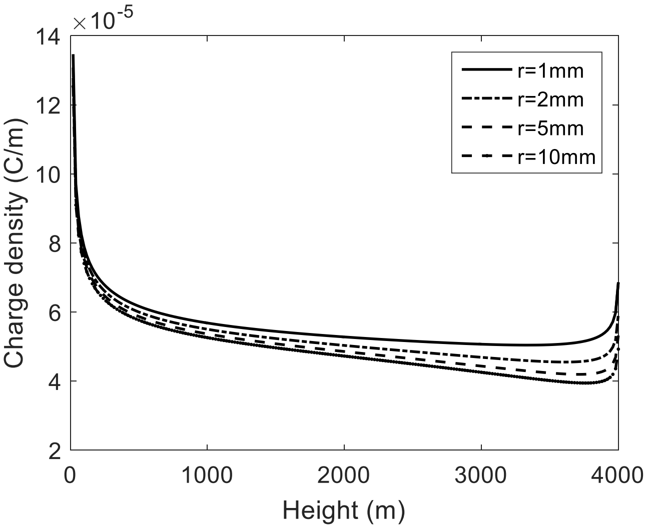

(a) Influence of core radius

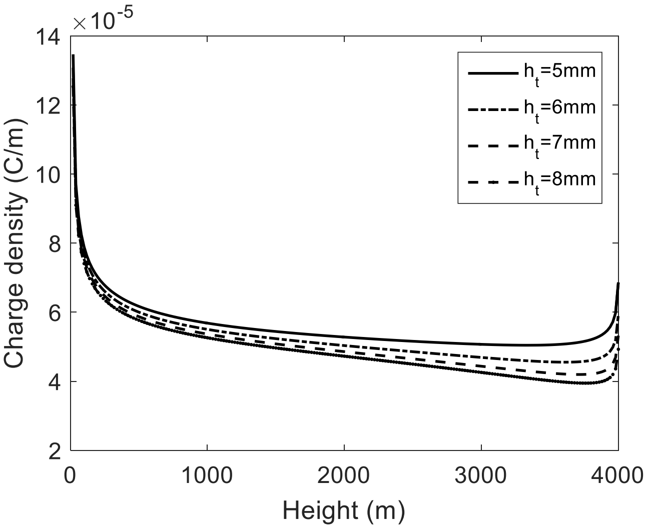

(b) Influence of cloud tip height

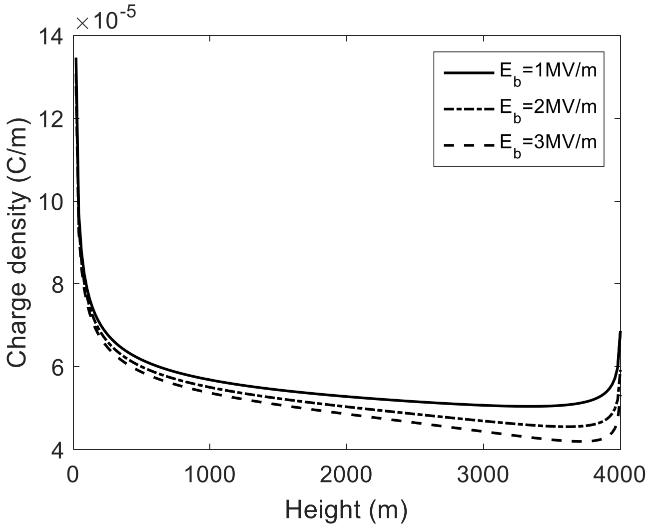

(c) influence of breakdown electric field

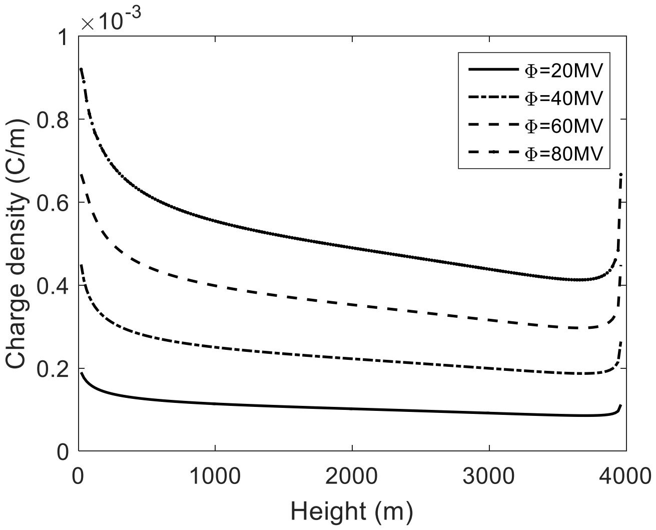

(d) influence of cloud potential

Fig.2-7 An investigation of different parameters on the charge density distribution along height

It is found that the core radius does not have a noticeable effect on the charge density distribution along the channel. With increasing the cloud size, the charge density along the channel decreases, especially in the position near the cloud base. The charge density decreases more than 10% when the breakdown field changes from 1 MV/m. to 3 MV/m. This is because increasing the breakdown electric field will cause the corona sheath to be hard to expand, and lead to a decrease in the channel charge density. The cloud potential determines the total charge distributed at the cloud and then influences the charge density along the channel. With increasing cloud potential, the magnitude of charge density increases significantly.

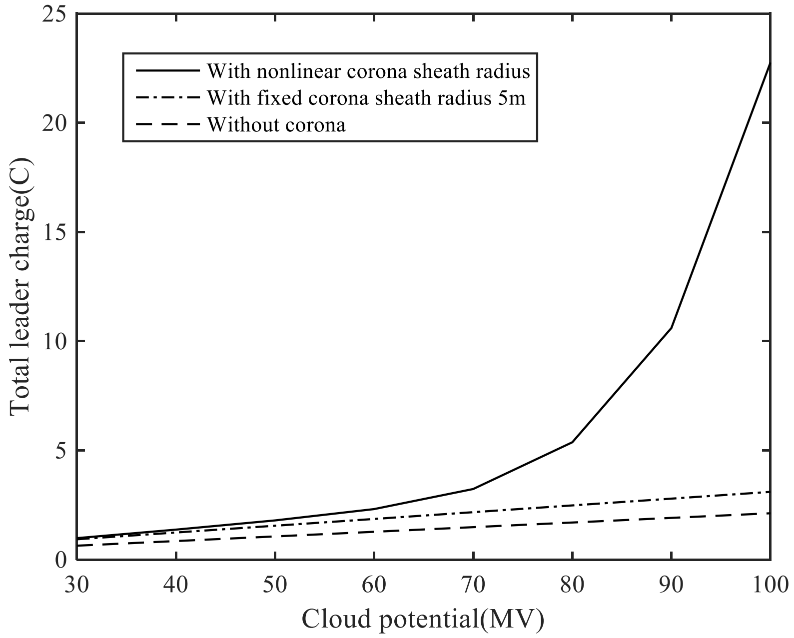

Fig. 2-8 Relationship between the cloud potential and the total leader charge with and without corona considered

Fig. 2-8 shows the corona effect on the relationship between the total leader charge and the cloud potential. The cloud potential varies from 30 MV to 100 MV. The solid line is the calculated result with the corona discharge and the dashed line is without the corona discharge in the leader channel. To give a comparison with the existing linear leader model in the literature [38], the result calculated with a fixed corona sheath radius r_{corona} of 5 m is also presented. It is found that, when considering the corona effect, the ratio of the total leader charge to the cloud potential increases significantly with the cloud potential. Which means, a strong nonlinear relationship is observed. The possible reason may be that, under the effect of corona discharge, some of the leader charge is pushed away from the channel core and stored in the corona sheath. This may result in a decrease in the nonlinear potential coefficient because the core potential coefficient is much greater than the corona-sheath potential coefficient according to (6). With the proposed method, the simulated charge varies from 0.98C to 22.75 C. This is close to the experimental observation results, which are generally in the range of 1.1 C-20 C [42]. However, if the corona discharge is not considered, the charge varies from 0.63 C to 2.12 C, and if a fixed corona sheath radius is considered, the charge varies from 0.93 C to 3.1 C. These results deviate significantly from the experimental observation results.

Thus, a strong nonlinear behavior of the corona discharge during the lightning leader is necessary to consider if the cloud potential is of a large value.

2.4 Section Conclusion

This section proposed a leader charge simulation method that can reproduce the spatial-and-temporal distribution of the charge in the lightning leader process. The cloud volume charge, the channel volume charge, and the ground surface charge are taken into consideration as a whole in the proposed NCSM. In this method, the charge-dependent potential coefficient is introduced. This charge-dependent potential coefficient is mainly caused by the physical evolution of the corona sheath according to the experimental observation presented in the literature.

The NCSM proposed in this section accurately models the spatial and temporal distribution of charge during the downward negative lightning leader process, considering the cloud volume charge, channel volume charge, and ground surface charge. It incorporates a charge-dependent potential coefficient, which reflects the physical evolution of the corona sheath. The method has been validated experimentally by comparing the resulting electric field at distant positions, showing its ability to calculate charge distribution density under various lightning environments. The relationship between the lightning physical parameters and the charge density distribution along a leader channel is further studied. The simulation results are much more reasonable if the dynamic corona effect is taken into consideration.

This method is practically used to improve the design of lightning protection systems for tall structures, assess lightning-induced surges in power grids, and better understand the effects of environmental conditions on lightning behavior. It can solve problems related to inaccurate charge distribution modeling, enhance lightning-induced overvoltage prediction, improve protection strategies, and increase the accuracy of lightning simulations, ultimately providing more effective protection and risk assessment for electrical infrastructures exposed to lightning.

3 NCSM-PEEC-Based Leader-Return Stroke Integrated Modeling

3.1 Introduction

Understanding the interaction between lightning strikes and tall structures is critical for advancing both scientific research and practical engineering solutions. The complexity of lightning discharges, particularly the behavior of lightning channels and their effects on the surrounding environment, necessitates the development of more accurate models. These models can provide a deeper understanding of the physical processes that govern lightning strikes, such as the influence of the corona sheath, charge distribution, and the resulting electromagnetic fields. Accurately simulating these dynamics is essential for designing more effective lightning protection systems, which are increasingly important as the number of tall structures, such as wind turbines and high-rise buildings, continues to grow. By improving the understanding of how lightning interacts with these structures, engineers can develop better strategies to mitigate the risks of lightning-induced damage to critical infrastructure.

In the second section, we proposed a method to simulate the charge distribution during the leader stage before the lightning return stroke. The charge distribution during this phase is crucial as it determines the initial conditions for the return stroke, directly influencing the current and electric field distribution during the stroke. By simulating the evolution of charge in the leader stage, we gain a better understanding of the spatial and temporal charge distribution along the lightning channel, which provides accurate initial conditions for the return stroke. However, simulating only the charge distribution in the leader phase is insufficient to fully capture the interaction between the lightning channel and tall structures, particularly during the return stroke. Therefore, in this section, we will further present an integrated model for the lightning return stroke that incorporates the interaction between the lightning channel and tall structures. This model will combine the electrical properties of the lightning channel with the geometric and conductive characteristics of the structure, as well as the ground properties, providing a more accurate representation of the return stroke behavior.

Over the past several decades, researchers have developed numerous methods for assessing the impact of lightning on structures and systems on the ground. However, modeling the interaction between a lightning discharge and tall, vertically extended structures—such as wind turbines, transmission towers, and high-rise buildings—presents additional complexities. The presence of such structures in the discharge path can significantly influence the return-stroke current waveform and modify the characteristics of the radiated EM fields in the vicinity. Studies have shown that tall structures can distort the lightning return stroke and create variations in the behavior of the induced electromagnetic fields that are not observed in strikes to the flat ground [1-2]. Moreover, the electrical characteristics of the lightning channel itself play an essential role in this interaction, particularly by affecting the reflection coefficient at the top of tall towers. The reflection coefficient determines how much of the lightning current is reflected back up the tower and how much is transmitted downward into the structure and grounding system. This, in turn, impacts the current distribution along the tower, which is crucial for understanding the stress experienced by the structure during a lightning strike [3].

Given the complex nature of the interaction between a lightning strike and a tall structure, simulating lightning currents using a simple current source model is insufficient for accurately predicting the behavior of the system under real-world conditions. Lightning strikes involve not only the current flowing through the lightning channel but also the electromagnetic coupling between the channel and the surrounding environment. Thus, to adequately represent these dynamics, an integrated model that accounts for the interaction between the lightning channel and the structure on the ground is necessary. Such a model must consider the electrical properties of the channel, the geometry of the structure, and the characteristics of the ground. By accurately simulating these factors, engineers can design more effective lightning protection systems and better understand the potential risks posed by lightning strikes.

In the past few decades, numerous models of lightning return strokes have been developed, each with its strengths and limitations. These models generally fall into four categories: physical models, electromagnetic (EM) models, transmission line (TL) models, and engineering models. Each of these models offers a different perspective on how lightning strikes interact with structures on the ground. For example, some models represent the return stroke as a current source, while others treat it as a voltage source or a charged line. Each approach provides valuable insights into the behavior of lightning-induced transients in tall structures and the electromagnetic fields that these transients generate.

The **engineering model**, initially developed to simulate lightning strikes on flat ground, has been extended to account for the presence of tall structures [4-5]. In this model, a current pulse is assumed at the lightning attachment point, which then propagates as two waves: one traveling upward along the lightning channel and the other downward along the structure. The tower or structure is typically modeled as a uniform, lossless transmission line characterized by reflection coefficients at its top and bottom. The accuracy of this model depends on how well the current pulse and the tower's transmission line characteristics match real-world conditions.

The **transmission line (TL) model** is another widely used approach for representing lightning channels. This model uses the per-unit-length inductance, capacitance, resistance, and conductance of the lightning channel to represent the distributed electrical properties of the system [6]. The TL model allows researchers to solve the well-known telegrapher’s equations to calculate the currents and voltages along the lightning channel. In the original TL model [7], constant distributed parameters were used, but subsequent revisions incorporated a nonlinear, time-varying resistance to simulate the radial expansion of the lightning core's radius [8]. Further refinements, such as the introduction of the non-uniform TL model [9], addressed current pulse attenuation and distortion, improving the model's ability to reproduce realistic lightning current waveforms. In this model, the characteristic impedance of the lightning channel varies with height, and the corona effect is included by adding either a nonlinear dynamic capacitance or a corona current source [10]. Studies have demonstrated that the distributed circuit model, when accounting for corona effects, is capable of reproducing critical characteristics of lightning return strokes in negative flashes, including realistic return stroke speeds and electromagnetic field signatures that are consistent with experimental observations [11].

The **electromagnetic (EM) model** provides yet another approach, representing the lightning channel as a thin wire that obeys Maxwell’s equations. Numerical solutions to these equations yield the current distribution along the lightning channel [12]. One common EM model is the antenna theory (AT) model, which simulates the interaction between a lightning strike and a tall tower [13]. In this model, a voltage source is used to simulate the lightning current at the attachment point, but the model generally disregards multiple reflections at discontinuities in the tower. While the AT model offers a detailed representation of the electromagnetic interactions in a lightning strike, it does not fully account for the complex reflection dynamics within tall structures.

In recent years, the physical mechanism of the corona sheath surrounding a lightning channel has been the subject of significant study. The corona sheath, which forms around the core of the lightning channel, plays an essential role in determining the current distribution and the electromagnetic fields generated during a lightning strike. A simplified corona sheath model was proposed in [14], representing the corona sheath as a lumped current source that could be applied in the engineering, TL, and EM models. In this model, the distributed charge inside the corona sheath drives the radial expansion of the sheath, influencing both the lightning channel's electrical properties and the surrounding electromagnetic environment. The characteristics of corona discharges in a coaxial geometry have also been studied extensively [15], providing further insight into the role of the corona sheath in lightning-induced transients. Recently, a drift-diffusion model was introduced to capture the dynamic behavior of the corona sheath [40], and experimental studies have validated the model's predictions, particularly in the study of transient overvoltages in transmission line structures.

These advancements in lightning channel modeling have greatly enhanced our understanding of lightning-induced transients and the electromagnetic fields they generate. However, the interaction between lightning channels and complex structures on the ground, such as tall towers, has not been fully explored. In practical engineering applications, the **partial element equivalent circuit (PEEC) method** offers a promising approach for modeling complex wire structures, particularly in the context of electromagnetic compatibility (EMC) and transient simulations [17]. The PEEC method has been widely adopted for modeling lightning strikes in real-world systems, where it can address more complex EMC problems than traditional modeling techniques. By incorporating the PEEC method into lightning channel models, researchers can more accurately simulate the interaction between lightning strikes and tall structures, leading to better-informed decisions about lightning protection design [18-28].

In summary, the modeling of lightning return strokes has progressed significantly over the past few decades, with various models developed to simulate different aspects of lightning strikes and their effects on structures. However, there remains a gap in understanding how lightning interacts with complex, tall structures on the ground. This section aims to address this gap by further exploring the interaction between lightning channels and tall towers using advanced modeling techniques such as the PEEC method. By developing more accurate and integrated models, this research will contribute to the design of more effective lightning protection systems and a better understanding of how lightning affects critical infrastructure on the ground.

3.2 Extended TL Model of a Lightning Channel

Shown in Fig. 1 is the configuration of a return stroke in a negative lightning flash terminating on a tall structure. This return stroke generates two current waves: one propagating upward along the lightning channel and the other one propagating downward along the structure. A hybrid circuit model then is proposed for evaluating both channel and structure currents, with a voltage source at the attachment point. In this model, the lightning channel is represented as a thin-wire core surrounded by the corona sheath. A non-linear and non-uniform TL model, similar to that in [10] is adopted. The telegrapher's equations for this TL model are described using node voltage V (with respect to infinity) and branch current I, as follows:

$$\begin{aligned} -\frac{\partial V(z,t)}{\partial z} &= L_{ch}(z,t)\frac{\partial I(z,t)}{\partial t} + R_{ch}(t)I(z,t) \\ -\frac{\partial I(z,t)}{\partial z} &= C_{ch}(z,t)\frac{\partial V(z,t)}{\partial t} + G_{ch}(z,t)V(z,t) \end{aligned} \quad (3\text{-}1)$$

where R_{ch}, L_{ch} , C_{ch} and G_{ch} are the per-unit length resistance, inductance, capacitance, and conductance of the lightning channel. These parameters generally vary with time and channel current as well.

By neglecting the skin effect, the core resistance is calculated with $R_{ch}(t) = 1/\sigma\pi r_c^2(t)$, where σ is the channel conductivity. Core radius r_c expands radially, and is determined by core current $i(t)$, as follows:

$$r_c(t)=\sqrt{(0.25\sigma\xi\rho_0\pi^2)^{-1/3}\int_0^t i(t)^{2/3}dt+r_0^2} \tag{3-2}$$

according to the strong-shock approximation [8]. In (3-2), r_0 is the initial radius corresponding to the leader channel, ρ_0 is the atmospheric density, and ξ is the factor controlling the expansion rate of the channel proposed in [16].

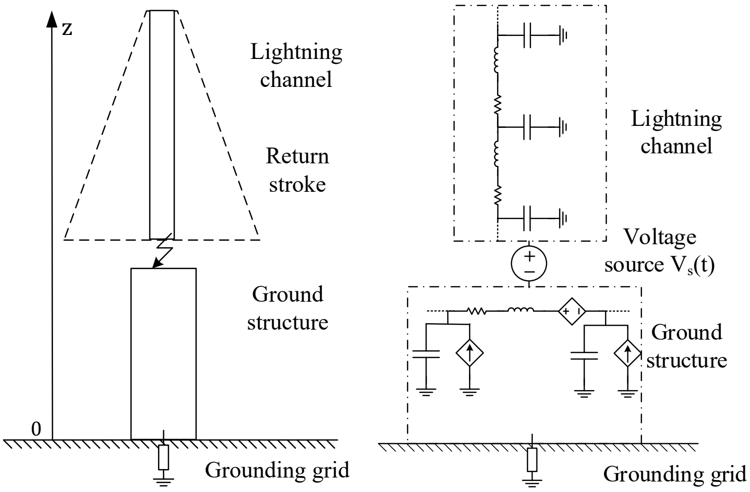

(a) Configuration (b) Equivalent circuit

Fig.3-1 Lightning return stroke terminated on a tall structure.

In [9], both height-variant inductance and capacitance are introduced for the non-uniform model of a lightning channel. Note that in (3-2) core radius is a function of the core current, and varies with both time t and height z. The original per-unit-length inductance and capacitance then are expressed with time-and height-variant radius r_c, as follows:

$$\begin{aligned} L_{ch}(z,t)&=\frac{\mu_0}{2\pi}\ln(\frac{2z}{r_c(z,t)}) \\ C_{ch}(z,t)&=\frac{1}{2\pi\varepsilon_0}\ln(\frac{2z}{r_c(z,t)}) \end{aligned} \tag{3-3}$$

where C_{ch} in (3-3) is the capacitance without the corona effect.

3.3 Dynamic Corona Sheath Capacitance and Conductance

In the corona model proposed in [15], a simple coaxial structure is adopted to calculate radial corona currents. This coaxial arrangement assumes the presence of both central and outer conductors even if the corona does not exist. The radial expansion of the corona sheath increases with increasing voltage applied on the central conductor or the core. In this proposed model, the modified relationship between the voltage and the corona sheath behavior is adopted. Unlike the coaxial structure in which only the core-to-sheath voltage is considered, the voltage in the proposed model is composed of two parts, the sheath voltage V_{sh} and the core-to-sheath voltage V_{co-sh}, as shown in Fig. 3-2(a). Note that the lightning return stroke is a discharging phenomenon. The voltage of the desired lightning source monotonously increases with time if the voltage before the final jump is set to be the reference.

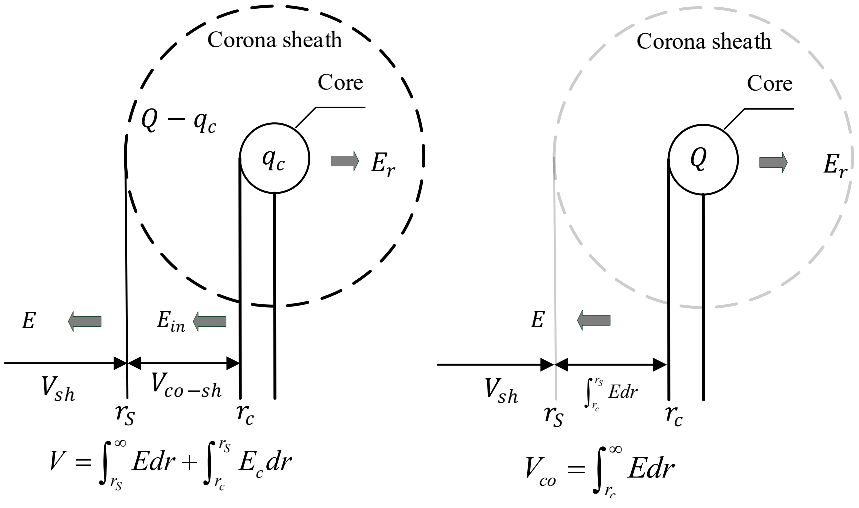

(a) Model with corona effect (b) Model without corona effect

Fig.3-2 Model of dynamic corona sheath

Fig. 3-2 shows the configuration of the corona sheath with radius r_S enclosing a lightning channel core. Q is the total charge per unit length on the transverse plane of the channel. In the corona sheath zone ($r_c < r < r_S$), uniform breakdown transverse electric field E_c is assumed. It is equal to the electric field on the sheath boundary $(r = r_S)$, i.e., $E_c = Q/2\pi r_S \varepsilon_0$. The voltage between core and sheath V_{co-sh} then is obtained by $\int_{r_c}^{r_S} E_c dr$, which is evaluated as $E_c(r_S - r_c)$.

Electric field E outside the corona sheath zone $(r \geq r_S)$, can be determined by per-unit-length charge located on the given position of the channel, i.e., $E = Q/2\pi r \varepsilon_0$. Subsequently, voltage V_{sh} is obtained by $\int_{r_S}^{\infty} E dr$. Note that, according to Coulomb's law, the electric field outside the corona sheath remains the same no matter whether or not the corona effect is considered once the total charge Q is given. Subsequently, $V_{sh} = V_{co} - \int_{r_c}^{r_s} E dr$ remains the same, where $V_{co} = \int_{r_c}^{\infty} E dr$. If the corona effect is not considered, as seen in Fig. 3-2(b), $V_{co} = Q/C_{ch}$ according to (3-3), and the integral $\int_{r_c}^{r_s} E dr$ can be evaluated by using $E = Q/2\pi r \varepsilon_0$ and $Q = 2\pi r_c \varepsilon_0 E_c$ if charge Q is concentrated on the core.

Thus, the core voltage V can be evaluated by summing V_{sh} and V_{co-sh}, as shown below:

$$\begin{aligned} V &= V_{sh} + V_{co-sh} \\ &= V_{co} - \int_{r_c}^{r_S} E dr + \int_{r_c}^{r_S} E_c dr \\ &= Q/C_{ch} - E_c r_c \ln(r_S/r_c) + E_c(r_S - r_c) \end{aligned} \tag{3-4}$$

Then, the modified capacitance including the corona effect is evaluated as

$$C'_{ch} = \frac{Q}{V} = \frac{Q}{Q/C_{ch} - E_c r_c \ln(r_S/r_c) + E_c(r_S - r_c)} \tag{3-5}$$

Sheath radius r_S is determined by per-unit-length total charge Q, i.e., $r_S = Q/2\pi E_c \varepsilon_0$. The derivation of C'_{ch} in (3-5) is made with the assumption of a thin-wire model, which does not need an artificial outer conductor. Similar to the model in [15], the electric field within the corona sheath is uniformly distributed and is equal to the breakdown value.

The channel conductance is defined in [10]. According to the current continuity equation, the following is obtained,

$$-\frac{\partial I(z,t)}{\partial x} = \frac{\partial Q(z,t)}{\partial t} \tag{3-6}$$

With (3-5), the transmission line equation with channel conductance is obtained, as follows:

$$\begin{aligned}-\frac{\partial I(z,t)}{\partial z} &= \frac{\partial C'_{ch}(z,t)V(z,t)}{\partial t} \\ &= C'_{ch}(z,t)\frac{\partial V(z,t)}{\partial t} + G'_{ch}(z,t)V(z,t)\end{aligned} \tag{3-7}$$

where, $G'_{ch} = \partial C'_{ch}/\partial t$ is the time-varying non-linear conductance per unit length of the line.

3.4 Generalized PEEC Model for The Structure On the Ground

The structure on the ground is represented by a set of interconnected wires in the lightning analysis. Such wires can be efficiently modeled with the PEEC method. In this method, a wire segment carrying current I_i with node voltage V_n and V_m at its two ends is described by the circuit equations [30], as follows,

$$\begin{aligned}&R_i I_i + \sum_j L_{ij}\frac{dI_j}{dt} = V_n - V_m \\ &\frac{dV_n}{dt} = \sum_k p_{nk}\frac{dq_k}{dt} = \sum_k p_{nk} I_{c,k}\end{aligned} \tag{3-8}$$

where q_k and $I_{c,k}$ are the total charge and capacitive current on segment (node) l_k. R_i is the resistance of segment (branch) l_i. Its equivalent circuit is given in Fig. 3-3. A network for a wire structure can then be built by connecting these circuits according to their topology.

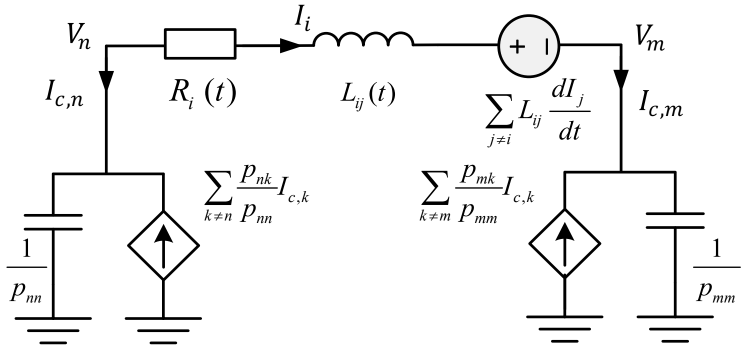

Fig. 3-3 PEEC model of a segment of conductor

In (3-8) partial circuit parameters of inductance L_{ik} and coefficient of potential p_{nj} are expressed using dyadic and scalar Green's functions $\bar{\bar{G}}_A$ and K_ϕ [30], as follows:

$$\begin{aligned} L_{ij} &= \frac{\mu_0}{4\pi}\int_{l_i}\int_{l_j} \bar{\bar{\boldsymbol{G}}}_A(r,r')\cdot d\boldsymbol{l}'_j\cdot d\boldsymbol{l}_i \\ p_{nj} &= \frac{1}{4\pi\varepsilon_0}\frac{1}{s_j s_n}\int_{l_n}\int_{l_j} K_\phi(r,r')\,dl'_j\,dl_n \end{aligned} \qquad (3\text{-}9)$$

where s_j is the length of segment l_j. In the presence of lossy ground, both dyadic Green's function $\bar{\bar{G}}_A$ and scalar Green's function K_ϕ can be approximated using a low-frequency model [30,45]. Note that $\bar{\bar{G}}_A$ has different components for current dipoles in three orthogonal directions. With this low-frequency model [30], both $\bar{\bar{G}}_A$ and K_ϕ for lossy ground can be expressed by:

$$\begin{aligned} &\bar{\bar{\boldsymbol{G}}}_A(r,r') \approx G_0(r,r')(\hat{x}\hat{x}+\hat{y}\hat{y}+\hat{z}\hat{z}) + G_0(r,r'')\hat{z}\hat{z} \\ &K_\phi(r,r') \approx G_0(r,r') - G_0(r,r'') \end{aligned} \qquad (3\text{-}10)$$

where free-space Green's function $G_0(r,r^*) = 1/|r-r^*|$, in which $*$ represents a symbol of prime $'$ or double primes $''$. Both r' and r'' are the source point and its image under the ground surface. $\hat{x}\hat{x}$, $\hat{y}\hat{y}$ and $\hat{z}\hat{z}$ are the dyadic products of unit vectors $\hat{x}$, $\hat{y}$ and $\hat{z}$ in the Cartesian coordination system. By considering the electromagnetic retardation in the model, the time-domain PEEC equations of (3-8) are revised to be

$$\begin{aligned} V_n - V_m &= R_i I_i + \sum_j L_{ij,a}\frac{dI_j(t-\tau)}{dt} + \sum_j L_{ij,g}\frac{dI_j(t-\tau)}{dt} \\ I_{c,n} &= \frac{1}{p_{nn,a}}\frac{dV_n}{dt} - \sum_{j\neq n}\frac{p_{nj,a}}{p_{nn,a}} I_{c,j}(t-\tau) - \sum_j \frac{p_{nj,g}}{p_{nn,a}} I_{c,j}(t-\tau) \end{aligned} \qquad (3\text{-}11)$$

where τ the retardation time. Subscripts "a" and "g" denote the parameters for the elements in the air and their images under the ground, respectively.

3.4.1 Integrated model for the channel and wire structure

Both the lightning channel and the wire structure on the ground are respectively represented with the TL and PEEC models. As the voltage in two circuits is defined as the electric potential with respect to infinity, these circuits can be merged by serial connection via a voltage source, as shown in Fig. 3-1(b).

The PEEC model is solved with a modified node analysis (MNA) approach. The matrix equation is expressed by:

$$\begin{bmatrix} -\mathbf{A}_{st} & -\mathbf{R}_{st} - \mathbf{L}_{st}\, d/dt \\ \mathbf{C}_{st}\, d/dt & -\mathbf{A}_{st}^{T} \end{bmatrix} \begin{bmatrix} \mathbf{V}_{st} \\ \mathbf{I}_{st} \end{bmatrix} = \begin{bmatrix} \mathbf{V}_{st,s} \\ \mathbf{I}_{st,s} \end{bmatrix} \tag{3-12}$$

where $\boldsymbol{A}_{st}$ is the incidence matrix of the wire structure, and $\boldsymbol{R}_{st}$, $\boldsymbol{L}_{st}$and $\boldsymbol{C}_{st}$ are the resistance, inductance, and capacitance matrices, respectively. $\boldsymbol{C}_{st}$ is the inverse of the potential coefficient matrix.

The TL model is described by the telegraph equations as shown in (3-1). With the spatial discretization along the channel using backward differences, the following equations are obtained at $z = k\Delta z$ with a segment length of Δz,

$$\begin{aligned} V_k(t) - V_{k+1}(t) &= L_{ch}(z,t)\frac{dI_k(t)}{dt} + R_{ch}(t)I_k \\ I_k(t) - I_{k+1}(t) &= C_{ch}(z,t)\frac{dV_k(t)}{dt} \end{aligned} \tag{3-13}$$

Here, the subscript "*ch*" represents the lightning channel. The matrix equation of (3-13) is given by

$$\begin{bmatrix} -\mathbf{A}_{ch} & -\mathbf{R}_{ch} - \mathbf{L}_{ch}(z,t)\, d/dt \\ \mathbf{C}_{ch}(z,t)\, d/dt & \mathbf{A}_{ch}^{T} \end{bmatrix} \begin{bmatrix} \mathbf{V}_{ch} \\ \mathbf{I}_{ch} \end{bmatrix} = \begin{bmatrix} \mathbf{V}_{s,ch} \\ \mathbf{I}_{s,ch} \end{bmatrix} \tag{3-14}$$

(3-14) is similar to the equation of the PEEC model in (3-12). Note that both $\boldsymbol{L}_{ch}$ and $\boldsymbol{C}_{ch}$ are the diagonal matrices.

By merging (3-12) and (3-14) together, a generalized MNA matrix equation with combined node voltage $\mathbf{V}=[\mathbf{V}_{\mathrm{st}}\ \mathbf{V}_{\mathrm{ch}}]^{\mathrm{T}}$ and branch current $\mathbf{I}=[\mathbf{I}_{\mathrm{st}}\ \mathbf{I}_{\mathrm{ch}}]^{\mathrm{T}}$, is obtained by

$$\begin{bmatrix} -\mathbf{A} & -\mathbf{R} - \mathbf{L}d/dt \\ \mathbf{C}d/dt & -\mathbf{A}^{T} \end{bmatrix} \begin{bmatrix} \mathbf{V}(t) \\ \mathbf{I}(t) \end{bmatrix} = \begin{bmatrix} \mathbf{V}_s(t) \\ \mathbf{I}_s(t) \end{bmatrix} \tag{3-15}$$

Mutual coupling between the lightning channel and wire structure can be modeled with the PEEC method. Its circuit parameters $\boldsymbol{L}_m$ and $\boldsymbol{P}_m$ can be calculated with (3-9). Then, the resistance, inductance, and capacitance matrices in (3-15) are

$$\mathbf{R}=\begin{bmatrix}\mathbf{R}_{ch} & 0\\ 0 & \mathbf{R}_{st}\end{bmatrix}\quad \mathbf{L}=\begin{bmatrix}\mathbf{L}_{ch} & \mathbf{L}_{m}\\ \mathbf{L}_{m} & \mathbf{L}_{st}\end{bmatrix}$$

$$\mathbf{P}\approx\begin{bmatrix}\mathbf{C}_{ch}^{-1} & \mathbf{P}_{m}\\ \mathbf{P}_{m} & \mathbf{P}_{st}\end{bmatrix}\quad \mathbf{C}=\mathbf{P}^{-1}\approx\begin{bmatrix}\mathbf{C}_{ch} & \mathbf{C}_{m}\\ \mathbf{C}_{m} & \mathbf{P}_{st}^{-1}\end{bmatrix}$$

where $\boldsymbol{C}_m = \boldsymbol{C}_{ch}\boldsymbol{P}_m\boldsymbol{P}_{st}^{-1}$ for the weak coupling in a line structure. If the retardation effect is taken into consideration, the merged matrix equation is re-written, as follows:

$$\begin{bmatrix}-\mathbf{A} & -\mathbf{R}-\mathbf{L}_0 d/dt\\ \mathbf{C}_0 d/dt & -\mathbf{A}^T\end{bmatrix}\begin{bmatrix}\mathbf{V}(t)\\ \mathbf{I}(t)\end{bmatrix}=\begin{bmatrix}\mathbf{V}_\text{s}(t)+\mathbf{L}_\text{d} d/dt\,\mathbf{I}(t-\tau)\\ \mathbf{I}_\text{s}(t)+\mathbf{C}_0\mathbf{P}_\text{d}[\mathbf{I}_\text{s}(t-\tau)+\mathbf{I}_\text{c}(t-\tau)]\end{bmatrix} \tag{3-16}$$

where, matrices with subscript 0 and d are the full matrices retaining entries for coupling with zero delay time, and entries for coupling with non-zero delay time, respectively. The other entries in these matrices are set to be zero. Capacitive current $\boldsymbol{I}_c$, is given by

$$\mathbf{I}_c(t)=\mathbf{C}_0 d\mathbf{V}(t)/dt-\mathbf{C}_0\mathbf{P}_\text{d}\mathbf{I}_\text{c}(t-\tau) \tag{3-17}$$

3.4.2 Voltage source in the integrated model

Because of the interaction between the lightning channel and wire structure, a simple current source is not appropriate to study the lightning current within the system. Thus the voltage source in an antenna theory model is proposed in [32] and the "undisturbed" source is defined in [38]. In this paper, the "undisturbed" voltage source used in the integrated model is introduced at the attachment point, as shown in Fig. 3-1(b). The source voltage in the gap is determined in such a way that the lightning current at the attachment point generally has the same waveform as the pre-specified lightning return stroke current $I_s(t)$.

Voltage $V_s(t)$ is composed of two components, voltage $V_{s1}(t)$ on the bottom of the channel and voltage V_{s2}(t) on the top of the structure with reference to infinity, under current $I_s(t)$ in the gap [32], as shown in Fig. 3-4(a). These two voltage components can be evaluated by total charge distribution along the channel/structure and the corresponding potential coefficients on the source position, i.e., $V_{si}(t) = \sum_j Q_{ij} \cdot P_{ij}$ (i =1 or 2). This can be written in a matrix form, as follows:

$$\begin{bmatrix} P_{11} & P_{12} \\ P_{21} & P_{22} \end{bmatrix} \begin{bmatrix} Q_{ch} \\ Q_{st} \end{bmatrix} = \begin{bmatrix} V_{s1} \\ V_{s2} \end{bmatrix} \tag{3-18}$$

where, P_{ii} is the self-coefficient and P_{ij} is the mutual coefficient for evaluating the contribution of distributed channel/structure charge to the structure/channel potential at source position. Both charge Q_{ch} and Q_{st} are determined by channel current I_{ch} and ground structure current I_{st} with the continuity equation of $\partial Q/\partial t = \nabla \cdot I$.

Fig. 3-4(b) and (c) show the configurations of two antennas constructed with the channel and the wire structure alone for the determination of both V_{s1} and V_{s2}. These two antennas are fed by the same current source $I_s(t)$ with a pre-specified waveform. All the parameters are evaluated by (3-16). An approximate match impedance is added at the end of the antenna to avoid the reflected wave. Once the MNA matrix is solved, the current distribution I_{ch} and I_{st}, as well as the charge Q_{ch} and Q_{st}, can be obtained. Note that the changing of radius of one arm does influence the response on another arm [43-44]. The currents in Fig.3-4(b) and (c) are approximately the same as those in the channel and structure. Thus, the channel base voltage $V_{s1}(t)$ and structure tip voltage $V_{s2}(t)$ can be obtained with (3-18).

It is noted that V_s is termed as an “undisturbed” voltage [32]. This “undisturbed” voltage does not contain the reflected waves from the ground. With $V_s = V_{s1} + V_{s2}$, the given “undisturbed” current at the attachment point is achieved before the reflected wave arrives.

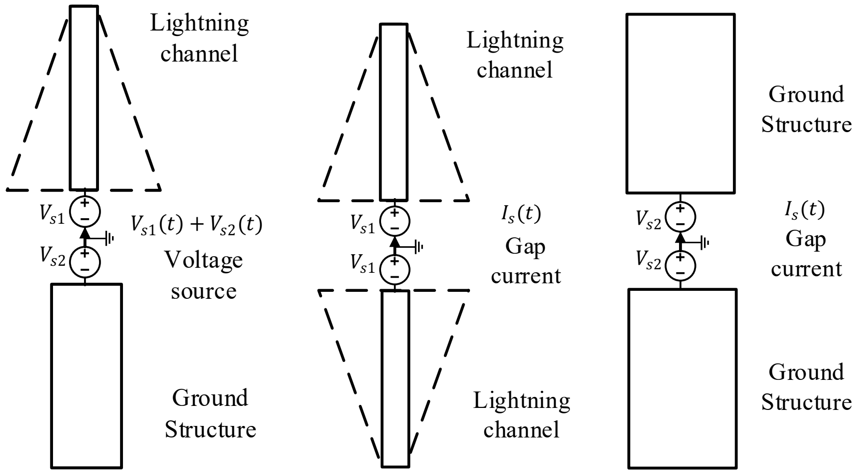

(a) (b) (c)

Fig.3-4 Antenna model for determining voltage source $V_{s1} + V_{s2}$: (a) Channel model (b) channel dipole (V_{s1}) (c) Ground structure dipole (V_{s2})

To find out a time-domain circuit solution, the differential equation in (3-15) is discretized in time by using the backward Euler method. Because the channel radius varies with the current, the MNA matrix contains nonlinear elements, particularly channel capacitance. The solution of (3-15) then is obtained by using the enhanced march on-in-time technique [39]. Consider channel resistance, inductance, and capacitance vary slowly with time. These parameters are assumed to be constant at each time step. The inductive voltage on the channel core and capacitive current in the corona sheath then are discretized, as follows:

$$\begin{aligned} L_{ch}(t)\frac{dI(t)}{dt} &\approx L_{ch}^{n-1}\frac{I^{n}}{\Delta t} - L_{ch}^{n-1}\frac{I^{n-1}}{\Delta t} \\ C_{ch}(t)\frac{dV(t)}{dt} &\approx C_{ch}^{n-1}\frac{V^{n}}{\Delta t} - C_{ch}^{n-1}\frac{V^{n-1}}{\Delta t} \end{aligned} \tag{3-19}$$

where V^n and I^n are the discrete voltage and current, and L_{ch}^n and C_{ch}^n are the discrete inductance and capacitance at $t = n\Delta t$.

It is noted in (3-5) that the channel capacitance is determined by the instantaneous value of channel charge Q. According to the current continuity equation, charge Q at time *t* and height *z* in the lightning channel is evaluated with

$$Q(z,t) = \int_0^t \frac{I(z+\Delta z,t) - I(z-\Delta z,t)}{2\Delta z}dt \tag{3-20a}$$

The charge in the core is determined by

$$q_c = \begin{cases} 2\pi\varepsilon_0 E_c r_c & Q \geq 2\pi\varepsilon_0 E_c r_c \\ Q & Q < 2\pi\varepsilon_0 E_c r_c \end{cases} \tag{3-20b}$$

With the charges given in (3-20), the dynamic capacitance of the channel then is obtained with (3-5).

3.5 Simulation Results and Discussion

3.5.1 Simulation of a direct lightning stroke to a tall tower

A direct lightning strike to the 553 m tall CN tower was recorded in [32]. The lightning current on the tower top was measured, and is presented in Fig. 3-6(b). It is observed that the waveform has two distinct peaks. The second peak is primarily caused by the current wave reflected from the ground. This cannot be simulated with an ideal current source. With the proposed model we can reconstruct the lightning return stroke current in the channel and replicate the lightning current on the tower.

Fig. 3-5 shows the model of the tower struck by lightning. The 5 km-long channel has an initial core radius of 1 mm, and a core conductivity of 2×10^4. The breakdown electric field is set to be 2 MV/m [16]. The tower is modeled with 4-leg 0.05 m-radius vertical conductor with a skypod, the spacing distance of adjacent legs is 4 m. The skypod has a diameter of 20 m and a height of 3 m [33]. The skypod is also modeled with 4-leg 0.05 m-radius conductors. The grounding resistance is set to be 30 ohm in this simulation. Both the channel and the tower body are discretized into segments with a 10 m length. The time step is 20 ns. The lightning channel is 5 km long in the simulation to avoid the reflection of the wave from its end. The computation time in a PC withi7-4790 CPU at 3.6 GHz and 16GB RAM is 360 s

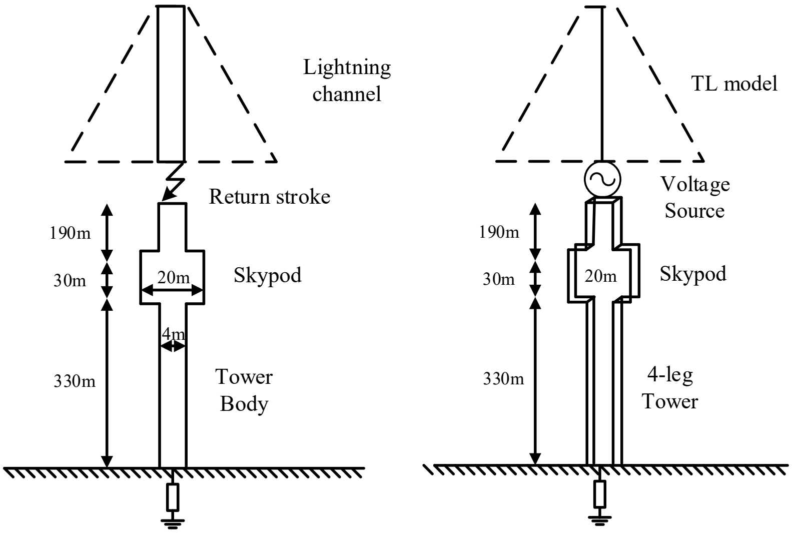

(a) Original configuration (b) Electromagnetic model

Fig.3-5 The lightning strike to the CN tower

Fig.3-6(a) shows the “undistributed" current” fitted with two Heidler’s functions. This current waveform is reconstructed to match the initial rising part of the measured current, and is expressed below:

$$I_s(t) = 5.5\frac{t^2/\tau_1^2}{1+t^2/\tau_1^2}e^{t/\tau_2} + 5.1(e^{-t/\tau_3} - e^{-t/\tau_4}) \tag{3-21}$$

where $\tau_1 = 0.07\mu s$; τ_2= $2\mu s$; ; $\tau_3 = 70\ \mu s$; $\tau_4 = 4\ \mu s$. With this “undistributed" current”, the voltage source in the integrated model can be obtained by applying the procedure in Section 3.5.2.

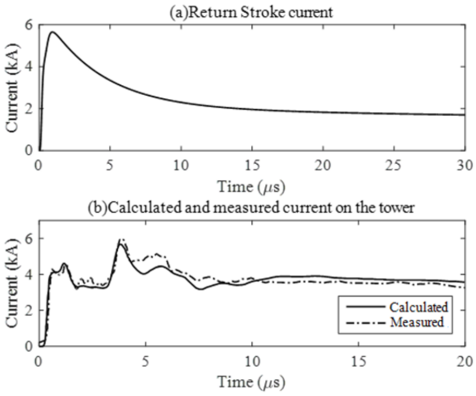

Fig.3-6 Comparison of simulated and measured currents on the CN tower

The tower top current is simulated with (16), and is presented in Fig.3- 6(b) together with the measured current. It is observed that the initial rising portation of the current and its multiple reflections are reproduced. Both measured and simulated currents match well.

Electric fields arising from the lightning return stroke to the ground are evaluated. First of all, the distribution of the channel current is determined with the proposed model. Uman's formula in Appendix [36] then is applied to calculate electric fields at different distances. When calculating the vertical electric field, the effect of the lossy ground is approximated by the perfect ground if the distance is in the order of kilometers or less [41]. For the electric field at 100 km away from the channel, the ground reflection factor is chosen to be zero (no reflection) [42].

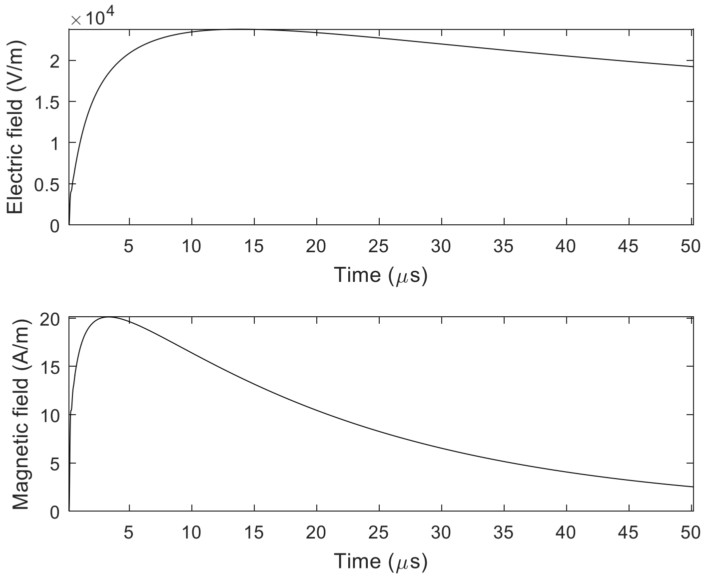

(a) D = 50 m

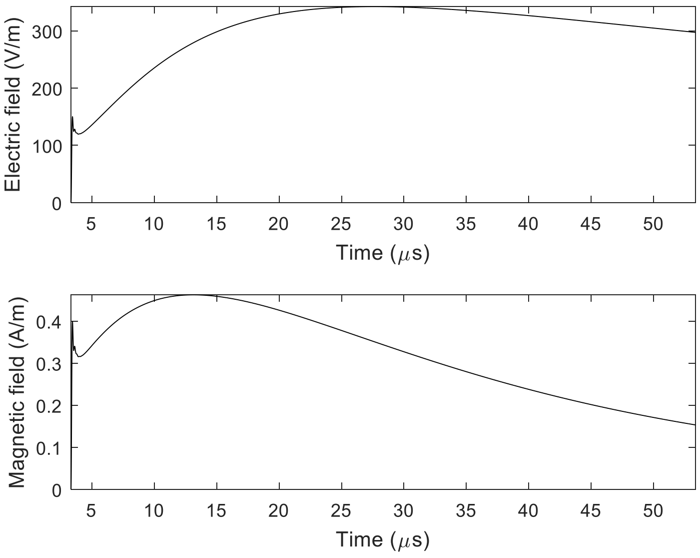

Electric field (V/m)
0
100
200
300
5
10
15
20
25
30
35
40
45
50
Time (μs)
Magnetic field (A/m)
0
0.1
0.2
0.3
0.4
5
10
15
20
25
30
35
40
45
50
Time (μs)

(b) D = 1k m

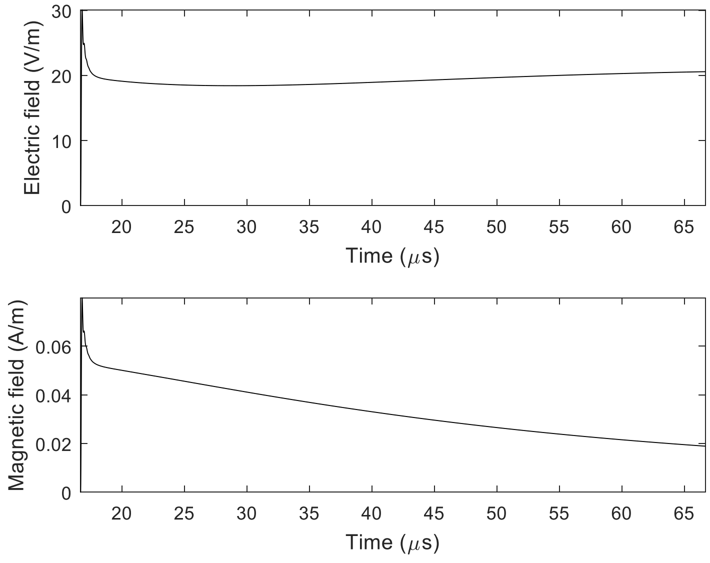

Electric field (V/m)
0
10
20
30
20
25
30
35
40
45
50
55
60
65
Time (μs)
Magnetic field (A/m)
0
0.02
0.04
0.06
20
25
30
35
40
45
50
55
60
65
Time (μs)

(c) D = 5km

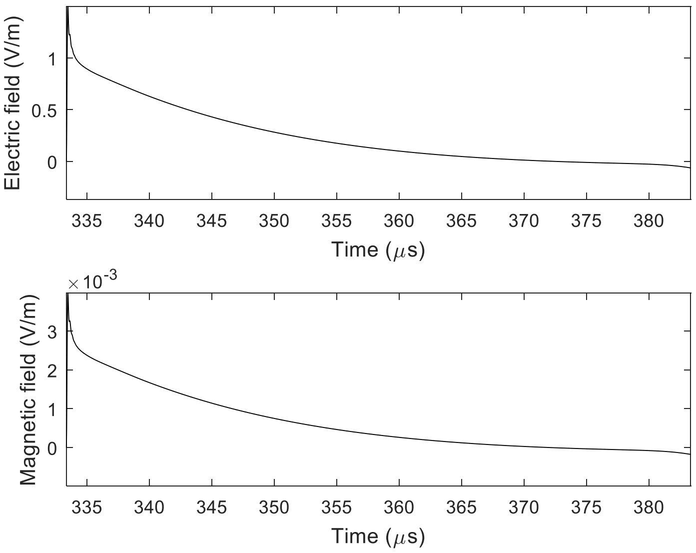

(d) D = 100 km

Fig.3-8 Calculated electric fields at the five distances from the CN tower

Fig.3-8 shows the vertical electric fields calculated at distances of 50 m, 1 km, 5 km, and 100 km. It is observed that these waveforms have the following features:

for electric field:

- A sharp initial peak at the distance of 5 km and 100 km
- Flattening of the electric field measured at 50 m
- Slow ramp after the initial peak at 5 km
- Zero crossing in the tail of field waveforms at 100km

for Magnetic field:

- A hump after the rising stage at 1km
- A Sharp initial peak at 5km and 100km
- Zero crossing in the tail of field waveforms at 100km.

These are the general characteristics of lightning-radiated electric fields reported in the literature [6]. Therefore, the calculated electric and magnetic fields are generally in coincidence with the measured fields.

3.5.2 Simulation of near electric fields under triggered lightning

In [35] a triggered lightning event on the 100-m-tall Gaisberg Tower was reported. Both the lightning current on the tower and electric fields in the vicinity were measured. Fig.3-10 shows the horizontal and vertical electric fields E_r and E_z measured on the height of 1 m above a metallic platform on a one-story building at a distance of 20 m and 22 m from the tower, respectively.

A simulation was performed with the proposed model for the comparison of electric fields in the vicinity of the tower. Fig.3-9 shows the configuration of the triggered lightning experiment. As suggested in [35], the structure struck by lightning is represented with a 60 m vertical wire and a 40 m tall leg constructed with 4 lateral wires and 1 central wire. All the wires have a radius of 0.005 m. The initial core radius is set to be 0.005 m, and the core conductivity is taken to be 10×10^4 S/m. The breakdown electric field is selected as 5 MV/m. The channel and the tower are discretized into 5 m long segments, and the time step is 10 ns. The input current waveform used in the simulation is the approximated Heidler function found in [35]. With this current, the voltage source is obtained by applying the procedure in Section 3.5.2.

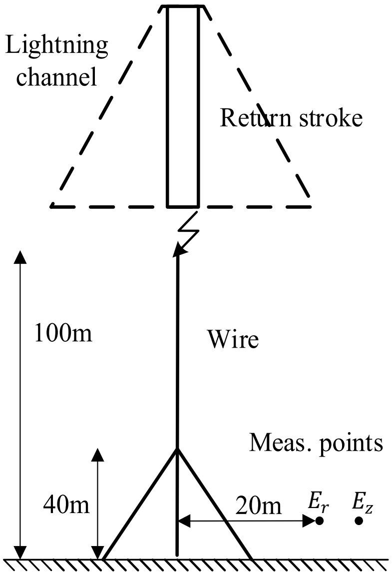

Fig.3-9 Configuration of the triggered lightning experiment

The currents in the channel and wires are simulated with the proposed method, and the electric fields in the vicinity are calculated with Uman's formula [36], as shown in Appendix. Because all the sensors are located above a metallic platform, the perfect ground is adopted in calculating the electric field [35]. Fig.3-10 shows both calculated horizontal and vertical electric fields at the same points where the measurement was taken. Good agreements are found between the calculated and measured results.

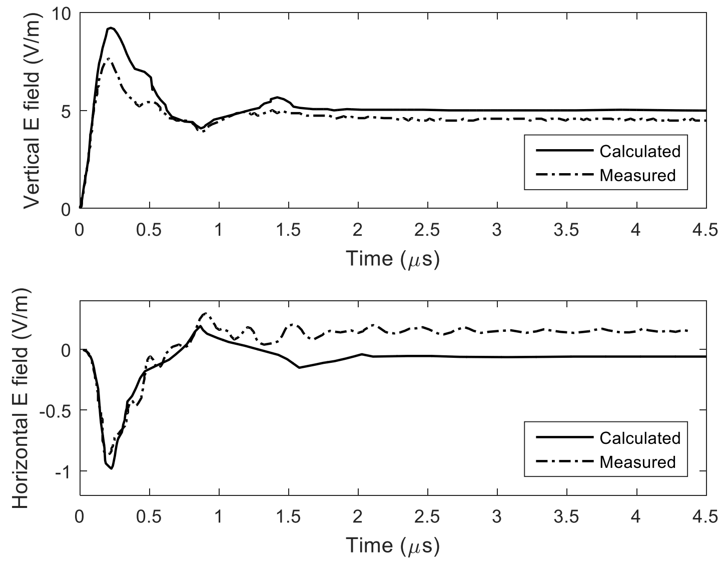

(a) Electric field comparisons

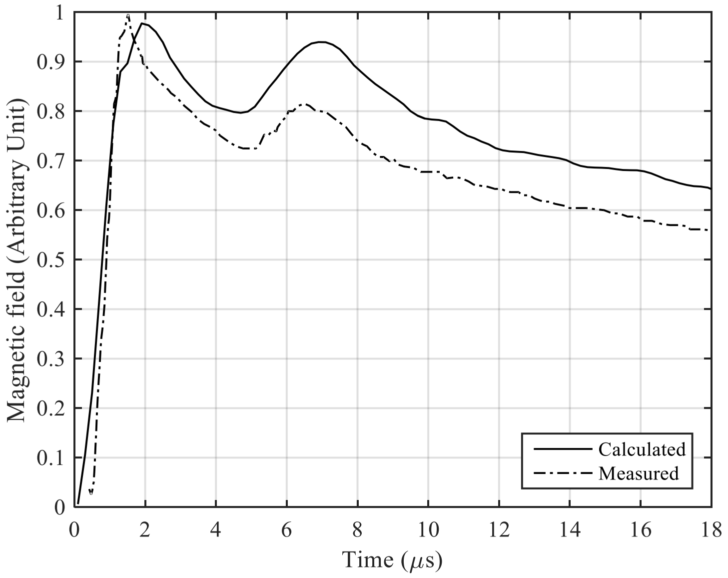

(b) Magnetic field comparison

Fig.3-10 Comparison between calculated and measured electric and magnetic field fields at the Gaisberg tower

4 The modeling and Assessment of Grounding system in the Low-Voltage Distribution Line System

4.1 Introduction

The second and third sections of this thesis primarily focus on lightning protection, where the interaction between lightning strikes and tall structures, including the modeling of lightning return strokes, is explored. These sections aim to develop advanced models to simulate lightning-induced transients and improve protection systems for tall structures. In contrast, the fourth section shifts its focus to address the second key issue of this thesis, which is the Fault Potential and Touch Voltage Risk in LV Distribution Systems. This section presents a detailed investigation into the risks posed by electrical faults in older residential communities, particularly in relation to fault potentials and touch voltages in low-voltage distribution networks, offering a deeper understanding of the safety concerns within these aging electrical infrastructures.

Electric shock hazards are a serious concern in many old residential communities, where outdated electrical infrastructure frequently threatens human safety. As urban environments expand and populations increase, many residential areas, particularly those developed decades ago, have not kept pace with advancements in electrical safety standards. These older communities are characterized by aging protective facilities that are often unable to meet modern safety requirements [1]. Over time, this issue has gained increasing attention from both engineers and regulatory bodies, given the growing awareness of the risks associated with outdated electrical installations [2-3].

The electrical safety infrastructure in older residential buildings typically includes protective devices that are either limited in functionality or significantly degraded due to aging. These devices may no longer be capable of providing adequate protection in the event of electrical faults, particularly when it comes to ensuring fault-line-cutoff protection [3]. As a result, residents of these communities are at heightened risk of electric shock, especially when faults occur within low-voltage (LV) distribution networks. Fault types such as line-to-ground faults, line-to-neutral faults, or neutral-line-open faults can cause the metalwork in the electrical grid to become energized, creating dangerous fault potentials. These faults lead to the risk of exposure to touch voltage, particularly in areas where protective measures are not functioning as intended.

Modern electrical protection methods, such as automatic disconnection of supply and equipotential bonding, have been developed to significantly reduce the risk of electrocution in residential areas [4-5]. However, implementing these protection measures in older residential communities is often challenging. Retrofitting old buildings with new protective devices, such as residual current devices (RCDs), is frequently impractical due to several factors. These include the complex and disorganized nature of the existing wiring systems, the high costs associated with extensive electrical modifications, and the physical limitations of older buildings. In many cases, the installation of new protective equipment in such communities requires substantial rewiring and structural changes, which are often deemed too costly or impractical to undertake.

Electrocution incidents in older residential communities are reported with alarming frequency. Numerous studies and accident reports highlight the vulnerability of residents in these environments, where inadequate protective measures contribute to repeated incidents of electric shock. In many cases, victims are electrocuted while standing on reinforced concrete (RC) floors or directly on the ground, both of which can serve as conductive paths for fault currents. The fault potential on RC floors and the surrounding ground surfaces becomes a critical factor in determining the risk of electrocution, particularly in cases where touch voltage—the voltage difference that a person might experience when simultaneously in contact with conductive surfaces—becomes dangerously high [6]. Understanding and mitigating these risks requires a thorough investigation into the factors that influence the potential rise on RC floors and ground surfaces, as well as the effectiveness of grounding configurations within the community.

One of the key elements in assessing the safety of electrical systems in old communities is the grounding configuration used in the LV distribution network. Grounding configurations play a vital role in directing fault currents to the ground and controlling the resulting touch voltage. Different types of grounding configurations, such as TN, TT, and IT systems, have different effects on the path of the fault current and, consequently, on the distribution of touch voltage throughout the community. Fault positions within the distribution network also have a significant impact on the level of risk posed to individuals in contact with conductive surfaces. A comprehensive investigation of these issues requires detailed consideration of both the grounding configuration and the fault position, as each of these factors contributes to the overall risk of electrocution in the event of an electrical fault.

In modern residential communities, grounding systems are carefully designed to ensure that fault currents are safely directed away from conductive surfaces that people might come into contact with. In particular, equipotential bonding is employed to ensure that exposed metalwork and conductive surfaces are at the same electrical potential, thereby minimizing the risk of electric shock. However, in old residential communities, such systems are often inadequate or absent altogether, meaning that individuals may be exposed to dangerous potential differences when faults occur. This is particularly true in areas where the wiring is poorly maintained or where protective devices have degraded over time.

Grounding configurations in older residential areas are often the result of historical design choices that were made according to the standards of the time. These configurations may no longer be suitable for the current demands placed on the electrical system, particularly as modern households use far more electrical appliances than in the past. Additionally, many old communities have undergone piecemeal renovations over the years, leading to inconsistencies in the grounding system. In some cases, buildings within the same community may have different grounding configurations, further complicating efforts to ensure electrical safety.

The type of grounding configuration used in a residential community has a direct impact on the path taken by fault currents in the event of a fault. For example, in a TN system, the neutral conductor is grounded at multiple points, creating a low-resistance path for fault currents. This reduces the likelihood of dangerous touch voltage developing at exposed metalwork. In contrast, a TT system relies on local earth electrodes to carry fault currents, which can result in higher touch voltages if the earth resistance is too high. Understanding the influence of different grounding configurations on touch voltage is critical for developing effective safety measures in old residential communities.

Accurate assessment of the voltage levels under fault conditions in LV distribution networks is essential for ensuring electrical safety in residential communities. Several methods have been developed to evaluate the ground surface potential and touch voltage under fault conditions. These methods can be broadly categorized into experimental studies and numerical simulation techniques.

Experimental studies, such as those conducted in [7-8], investigate the distribution of ground surface potential near grounding electrodes. These studies provide valuable insights into the behavior of fault currents and the resulting potential distribution on the ground surface, particularly in the vicinity of conductive structures. However, experimental methods are often limited in scope, as they require specialized equipment and controlled conditions that may not fully represent the complexities of real-world residential environments.

Numerical methods offer a more flexible and detailed approach to evaluating fault potentials and touch voltage in LV distribution networks. Analytical formulae can provide simplified models for calculating ground surface potentials, but they may not be sufficient for addressing the complex interactions between multiple conductive elements in a distribution network. More advanced numerical methods, such as the finite element method (FEM) [10-11], the boundary element method (BEM) [12], and the partial element equivalent circuit (PEEC) method [13-18], have been developed to overcome these limitations. These methods allow for detailed simulations of fault conditions, taking into account the specific configurations of the line system, the location of the fault, and the characteristics of the grounding system.

Among these numerical methods, the PEEC method stands out for its ability to model complex wire structures and its versatility in electromagnetic transient simulations. The PEEC method is derived from the mixed potential integral equations (MPIE) and has been widely used to simulate the behavior of buried conductors in the presence of lossy ground. This makes it particularly well-suited for studying ground surface potentials and touch voltages in old residential communities, where the electrical infrastructure is often characterized by a combination of aging buried conductors and unpredictable fault conditions [18]. By modeling the interactions between these elements, the PEEC method allows for a more accurate assessment of the risks associated with electrical faults in LV distribution networks.

With a given configuration of the line system and a known fault position, the ground surface potential and touch voltage can be quantitatively analyzed using the PEEC method. This approach provides a detailed understanding of how fault currents flow through the distribution network, how they interact with the grounding system, and where the most dangerous touch voltages are likely to occur. By applying these simulations to old residential communities, it is possible to identify specific areas of risk and develop targeted interventions to improve electrical safety.

The repeated occurrence of electrocution incidents in old residential communities underscores the urgent need to address the underlying causes of these accidents. The risks posed by outdated electrical infrastructure are not limited to isolated incidents but represent a persistent threat to the safety and well-being of residents. As populations in urban areas continue to grow, the demand for safe and reliable electrical infrastructure will only increase. Failure to address the electrical safety issues in old communities will likely result in continued electrocution fatalities and injuries, placing additional strain on emergency services and healthcare systems.

In many cases, the risks posed by electrical faults in old communities can be mitigated through relatively simple interventions, such as the installation of RCDs or the improvement of grounding systems. However, these interventions must be carefully planned and implemented to avoid creating new risks or exacerbating existing problems. For example, the installation of new protective devices in old buildings with disorganized wiring systems can introduce additional complexity, making it more difficult to ensure that the protective measures function as intended. Therefore, a thorough understanding of the specific electrical conditions in each community is necessary to develop effective and sustainable solutions.

Our contributions in addressing the electrical safety concerns in old residential communities are as follows:

1. PEEC-based Modeling of LV Distribution Network under Faults: A comprehensive modeling approach using the PEEC method is proposed to simulate the behavior of low-voltage (LV) distribution networks under fault conditions. This method is particularly effective for investigating the complex interactions between aging electrical infrastructure and fault currents.

2. Fault Potential Investigation: An in-depth analysis of fault potential is conducted, focusing on the mechanism of faults in the LV distribution network contribute to dangerous voltage differences across the ground surface, particularly near conductive structures. The proposed model is adopted for accurate assessment of the fault potential distribution in complicated environments, pinpointing areas of heightened risk for electric shock.

3. Touch Voltage Assessment: With the proposed PEEC-based simulations, the potential for dangerous touch voltages in residential communities is assessed, providing critical information for identifying high-risk zones and suggesting ways to mitigate these risks. The impact of fault conditions on touch voltage is evaluated, which refers to the voltage difference experienced by a person when simultaneously in contact with different conductive surfaces.

4. Step Voltage Assessment: The detailed simulations to evaluate step voltage in old residential communities is conducted, allowing for a more comprehensive understanding of the step voltage risks associated with faulty electrical systems in complicated environments.

By combining these three crucial assessments—fault potential, touch voltage, and step voltage—we have contributed to a more accurate and holistic understanding of the electrical safety issues in older residential communities. This research is essential for developing targeted safety strategy that can reduce the risk of electric shock and enhance the overall safety of older residential communities.

4.2 LV Residential Distribution Network

4.2.1 Typical configuration of the LV distribution network for simulation

A typical low-voltage (LV) power distribution line system is introduced in Fig.4-1. This system, from the transformer to the loads, consists of a 10kV/380V distribution transformer and main LV switchboard (SB) in the substation, an underground 4/c armored cable with a length of several hundred meters, sub-main distribution board (DB) at the end of the underground cable, overhead lines to final main DBs at the entrance of residential buildings, indoor final-main cables to consumer units, final cables to loads. Protective earth (PE) wires along the line system are provided if needed. Table 1 shows typical parameters of the line system adopted for fault analysis, which are provided by the local power company. After leading from the LV side of the distribution transformer, the buried four-core (4/c) XLPE/PVC cable with steel-wire armor (SWA) is equipped as the main circuit line before the entrance of the old community, after which the circuit is equipped with the overhead lines that have three phase lines and one neutral line, before the entrance of residential buildings. The first section of the overhead lines, called sub-main circuit I in the paper, is the main line of the old community. The subsequent section, called sub-main circuit II, is the main line before the entrance of the buildings. The final main circuit and final circuit, equipped with one-core (1/c) PVC cables, are arranged inside buildings and inside flats, respectively. The relative locations in the whole residential LV line system of each line section have also been illustrated in Fig.4-1 (b). Note that the phase lines have the same parameters as the neutral line, thus noted as the L/N line in Table. 4-1.

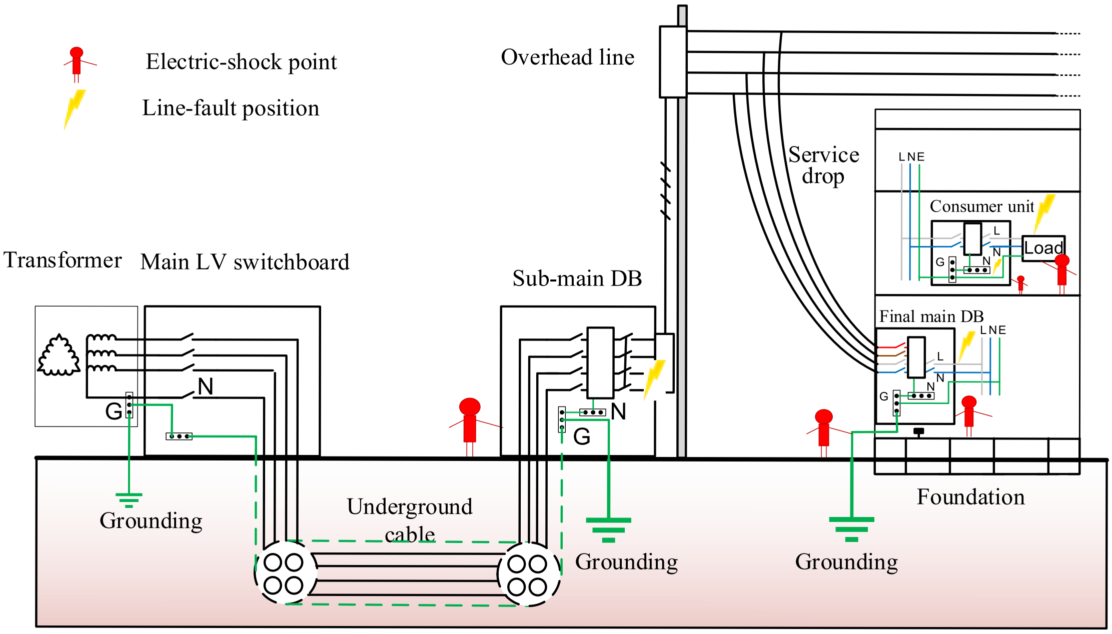

(a) Typical LV power network with the TX(M)–C-S grounding system, labeled with four possible fault locations and five possible electric shock points

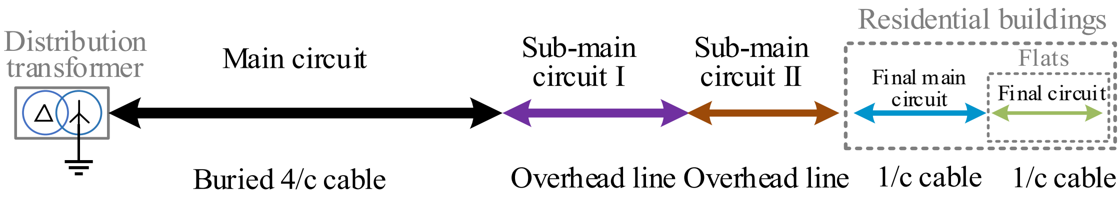

(b) Relative locations in the whole residential LV line system of each line section

Fig.4-1 Configuration in an old residential community.

Table. 4-1 Parameter in a LV distribution line system

Distribution circuit	Equipment	Parameters	
Power-supply side	Distribution transformer	10 kV/0.4 kV, 800 kVA, Z_t=6%	
Main circuit	Buried four-core (4/c) cable with steel-wire armor (SWA) Materials: XLPE/ PVC	L/N line	Length:250 m, Cross-section area (CSA): 240 mm^2
		PE wire	Length:250 m, CSA: 308 mm^2
Sub-main circuit I	Overhead line	Length: 100 m, CSA: 185 mm^2 Height: 3 m Conductor spacing: 0.1 m	
Sub-main circuit II	Overhead line	Length:50 m, CSA: 35 mm2, Height: 3 m Conductor spacing: 0.1 m	
Final main circuit (inside buildings)	1/c PVC cables	L/N line	Length:20 m, CSA: 10 mm^2
		PE wire	Length:20 m, CSA: 6 mm^2
Final circuit (inside flats)	1/c PVC cables	L/N line	Length:20 m, CSA: 4 mm^2
		PE wire	Length:20 m, CSA: 2.5 mm^2

4.2.2 Typical protective grounding configurations

Grounding of an LV residential distribution network is made of the power-supply side (substation) and DBS (Including sub-main DBs at the end of the underground cable and final DBs at the entrance of buildings for customer installation). Generally, a grounding grid is provided at the substation with a resistance of 2 ohms [21]. Vertical rods together with buried horizontal conductors outside buildings are adopted to ground the sub-main DBs and final DBs. No dedicated protective earth wires (PEs) provided in the distribution network for connecting these grounding terminals. Although the transformer neutral is grounded at the substation, the neutral (N) line in the distribution network may or may not be grounded. Inside buildings, electrical equipment is grounded through a separate protective earth wire (PE) or a protective-earth-neutral (PEN) wire. The buildings were built with RC, and their foundations were buried with steel reinforcement (rebar). These bars are interconnected to compose a network of conductors that can be used as a feasible grounded grid, which are not actually employed. Generally, the rebars in the buildings are concealed in concrete and are not exposed to the air. They are not intentionally connected to the grounding terminals at the final-main DBs. The electrode parameters for different sections, as well as the building foundation, are presented in Table. 4-2, which would be adopted in the fault analysis.

In old residential communities, three common grounding configurations are described below:

a) TT grounding configuration: exposed conductive parts (e.g., metal enclosures) of DBs, consumer units, and user equipment are all grounded via separate PE wires to their corresponding local grounding electrodes. The N wires in the distribution network are not connected to grounding terminals, except at the substation where the N wire is grounded solidly through the PE wire. Within buildings, the N wire is separated from the PE wire.

b) TT(M)-C-S grounding configuration: this is similar to the TT grounding configuration, except that the neutral wire is common-grounded at sub-main DBs via the connection with the PE wire. This is a grounding system with a multiple-point grounding of the N wires on the supply side.

c) TX(M)-C-S hybrid configuration: the N wire is connected to grounding terminals at both sub-main DBs and final-main DBs. This is a specialized TN-C-S grounding configuration with a multiple-point grounding of the wires from the substation to the entrance of buildings, as illustrated in Fig.4-1. Note that it is also called a TN-C-S configuration with a PEN extended to the entrance of buildings in [21].

It is noted that no matter which grounding configuration, the PE wires and metal enclosures of sub-main DBs, final main DBs, consumer unit, and loads are grounded via the local grounding terminals and the local grounding electrodes. The connection status between the N wire and PE wire at different sections is the main distinguish between the three configurations.

Table. 4-2 Electrode parameters for different sections of a typical residential LV distribution network.

Grounding Location	Conductor Configuration
Substation (distribution transformer)	Grounding grid of the substation with a resistance of 2 ohms
Sub-main DBs and final-main DBs	Vertical conductor: Number:1; Length: 1.5 m; Radius: 0.008 m; Horizontal conductor: Number:2; Depth: 0.8 m; Length: 1.5 m; Radius: 0.008 m;
Building foundations	Horizontal grid: Depth: 1 m; Size of mesh: 20 m×20 m; Size of cell: 5 m×5 m; Radius: 0.008 m

4.3 PEEC-based Modeling of LV Distribution Network under Faults

Fig.4-1 shows the possible locations of faults in an LV distribution network. Several kinds of faults that may lead to a safety hazard are of concern, including phase-to-ground (P-G) faults and line-to-neutral (L-N) faults. Under the P-G faults, the fault current will return via PE or PEN wires, grounding electrodes to the supply source. Therefore, all circuit components in the fault–current loop, including the grounding electrodes, need to be modeled for fault analysis. These components are generally represented with an equivalent RL circuit according to their physical parameters given in Tables 4-1 and 4-2. With these equivalent circuits, both fault currents and fault potentials at different locations in the community can be evaluated. Subsequently, both touch voltage and fault current across the body in an electric shock event can be determined. This section addresses the modeling of two key components: reinforced concrete and grounding grid, which may appear in a fault loop.

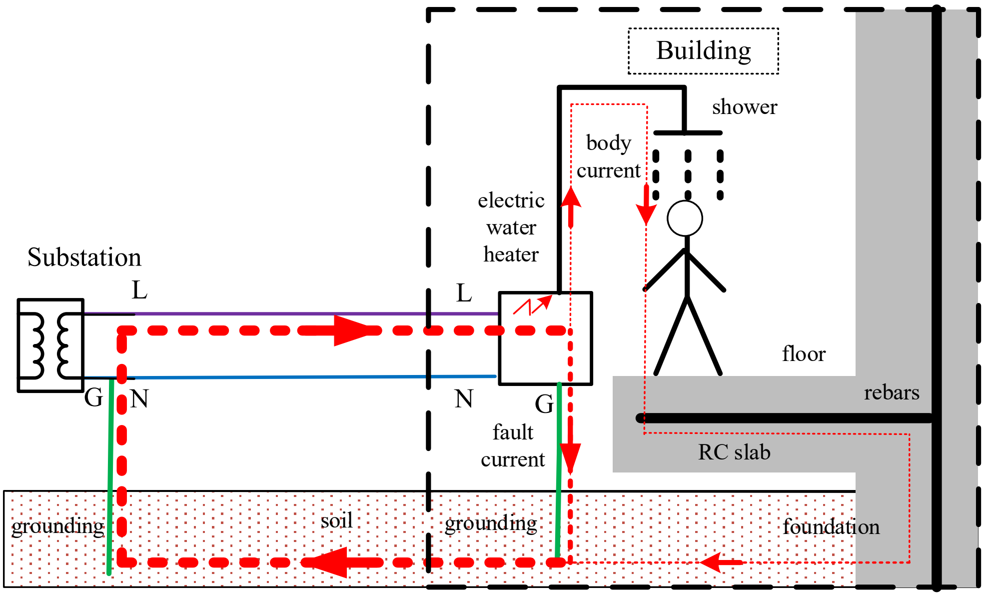

Fig.4-2 An electric shock scenario inside a building.

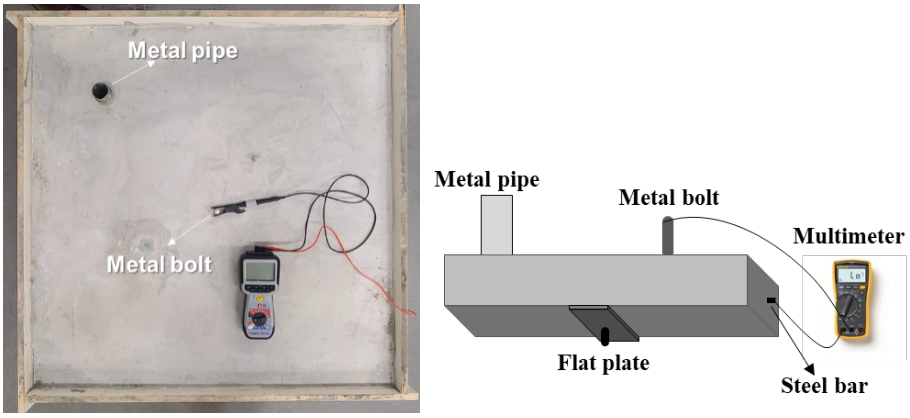

(a) Top view (b) 3D view

Fig.4-3 Experiment to measure the resistance on a 200 mm thick RC slab.

4.3.1 Model of a reinforced concrete (RC) slab in buildings

The concrete in a building may be considered a conductive part for the fault current across the body in an electric shock although it is not to carry a current under normal situations. Fig.4-2 illustrates a possible scenario of an electric shock accident under a ground fault within an electric water heater. The fault potential of an electric water heater in a bathroom generates a fault current when a person touches the metallic hose while standing on the floor. This fault current flows via the concrete slab to rebars. The rebars in the floor slab are connected to the steelwork in the foundation, which may be viewed as a grounding electrode for discharging the fault current across the body. The rebar resistance can be neglected as it is relatively small compared with the concrete resistance or human body impedance.

An equivalent resistance models the concrete appearing in an electric-shock scenario in the fault analysis. It is connected between the rebars and a contact surface emulating a person’s feet. This resistance could be calculated numerically through FEM or FDTD method [13-14]. It can be evaluated experimentally as well.

In this paper, the experiment method is employed in the laboratory to disclose the concrete resistance of a typical RC slab [20]. The experimental setup is shown in Fig.4-3. The RC slab has a size of 1 m×1 m× 0.2 m. A wire mesh made of rebars with a cell size of 0.2 m × 0.2 m was placed in the middle level of the slab. A couple of metal parts were embedded in the slab for measurement but were not connected to the rebars. These include metal screws, a metal pipe passing through the slab, and a metal plate on the slab surface. The resistance between the rebars and the metal parts in the slab was measured at 20℃ under dry and wet conditions, with the results presented in Table. 3. It is found that the resistance between the flat plate and rebars within the slab varies from 200 ohms to 300 ohms. Thus, in the simulation, the value of 300Ω is taken to represent the equivalent resistance between a person’s feet and the rebars of the floor.

Table.3 Experimentally measured resistances of an RC slab.

Metal Part	Flat plate		Metal bolt		Metal pipe	
Parameter	Size: 20 × 20 cm^2		Depth: 3 cm		Diameter: 5 cm	
Condition	Dry	Wet	Dry	Wet	Dry	Wet
Resistance (kΩ)	0.3	0.2	5	1.5	0.4	0.4

4.3.2 Modeling of grounding electrodes

When an electric-shock scenario occurs, the fault current across the body will be discharged via the PE wire, grounding electrode, or contact on the ground, as seen in Fig.4-2. The fault current is generally determined by ground potential or the potential difference $(V_A - V_B)$, as seen in Fig.4-4. Fig.4-4 illustrates the ground potential rise in fault condition, in which R_X represents the resistance of other components in the body-current circuit, such as the RC slab. When the grounding grid is made of a set of horizontal conductors, an admittance matrix for the grounding grid can be established using the PEEC formulas for the horizontal conductors [14, 16]. The detailed description of PEEC method is shown in section.3.4. In the PEEC method, the electromagnetic coupling between the concerned conductors in physic space could be transferred into the circuit-format coupling coefficient matrix to establish the equivalent equation matrix considering the propagation time delay. Note that the potential coefficient p_{nm} between two current-carrying segments l_n and l_m in the soil with a conductivity of σ_g is expressed by

$$p_{nm}=\frac{\sigma_g}{4\pi}\frac{1}{\Delta l_n \Delta l_m}\int_{l_n}\int_{l_m}\frac{1}{|r_n-r_m|}dl_n dl_m+\frac{\sigma_g}{4\pi}\frac{1}{\Delta l_n \Delta l'_m}\int_{l_n}\int_{l'_m}\frac{1}{|r_n-r'_m|}dl_n dl'_m$$

(4-1)

where l'_m is the mirror image of the segment l_m in the air. Both r_n and r_m are the coordinates of the points on segments l_n and l_m, and Δl_n and Δl_m are the length of these segments, respectively. The ground plane in this case is replaced by a segmented image in the air. The capacitance matrix $\boldsymbol{C}$ then is obtained by inverting the potential matrix, that is, $\boldsymbol{C}=\boldsymbol{P}^{-1}$ where $\boldsymbol{P}=\{p_{nm}\}$. Both inductance and resistance of segments themselves are neglected as they have a minor effect at 50 Hz compared with the conductance of these segments. To determine the ground surface potential in an electric shock scenario, an electrode must be provided, and mutual potential coefficients must be included in the potential matrix $\boldsymbol{P}$. In this paper, a flat contact surface of 20 cm x 20 cm serves as an electrode for discharging the fault current across the body. The potential coefficient between the flat surface s_n and the wire segment buried under the ground l_m is expressed by

$$p_{nm}=\frac{\sigma_g}{4\pi}\frac{1}{\Delta s_n \Delta l_m}\int_{s_n}\int_{l_m}\frac{1}{|r_n-r_m|}ds_n dl_m+\frac{\sigma_g}{4\pi}\frac{1}{\Delta s_n \Delta l'_m}\int_{s_n}\int_{l'_m}\frac{1}{|r_n-r'_m|}ds_n dl'_m$$

(4-2)

where Δs_n is the surface area of the flat contact on the ground.

4.4 Fault Potential Investigation for Different Grounding Configurations

Fig.4-4 also illustrates the ground surface potentials caused by a fault current injected into the ground. Under a ground fault, the metal enclosure of DBs and user equipment, or PE wires, could be subject to a fault potential nearly equal to V(0). They are represented as the conductors with fault potential in Fig.4-4. Such a potential, together with the ground potential V(x) at the surface of the soil, can be used to assess the touch voltage. As shown in Fig.4-4, the potential difference between point A (e.g., the hand-touching point) and point B (e.g., the feet-standing point) can be used to evaluate the touch voltage of a person. In the figure, R_x depicts an auxiliary resistance in the human-body current branch. In this section, the fault potential of equipment under different line faults is evaluated.

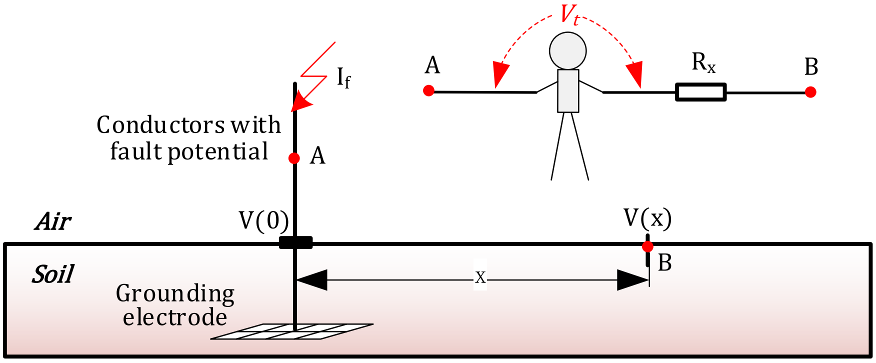

Fig.4-4 Illustration of ground potential *V(x)* and touch voltage V_t in the vicinity of an electrode.

Three typical line faults are of concern in this paper for fault potential assessment, *i.e.*, P-G fault, P-N fault, and neutral-line disconnection. It is noted that the fault current, as well as the fault potential, varies with fault location. Four typical fault locations are considered in the assessment. They are: 1) the sub-main DB, 2) the final-main DB at the entrance of a building, 3) the consumer unit in the building, and 4) the user equipment in the building. Note that the structural steel (rebars) of a building are not intentionally bonded to the grounding terminal at the final-sub main DB, as they are not exposed to the air.

4.4.1 Phase-to-ground fault

In this part, the phase-to-ground (P-G) fault occurring at different positions in an LV distribution network is of concern. Because a person may touch the equipment enclosure, the potential of the equipment enclosure (equipment potential) shall be calculated. It is assumed that the circuit breaker or residual current devices (RCD) is not activated under a fault for the worst-scenario assessment.

Fig.4-5 to Fig.4-7 show the simplified diagrams of the fault circuit with three grounding configurations respectively. The corresponding equipment potential under the ground fault is presented in these figures as well. As there are four possible fault locations described previously, the equipment potential at these locations is evaluated under each fault. In subfigure (b), equipment potential is depicted by vertical bars. These bars are grouped according to the fault location. In each group, the measure of equipment potential at four locations under a fault is presented, and both the maximum and minimum values of equipment potential in that group are indicated on the bar graph.

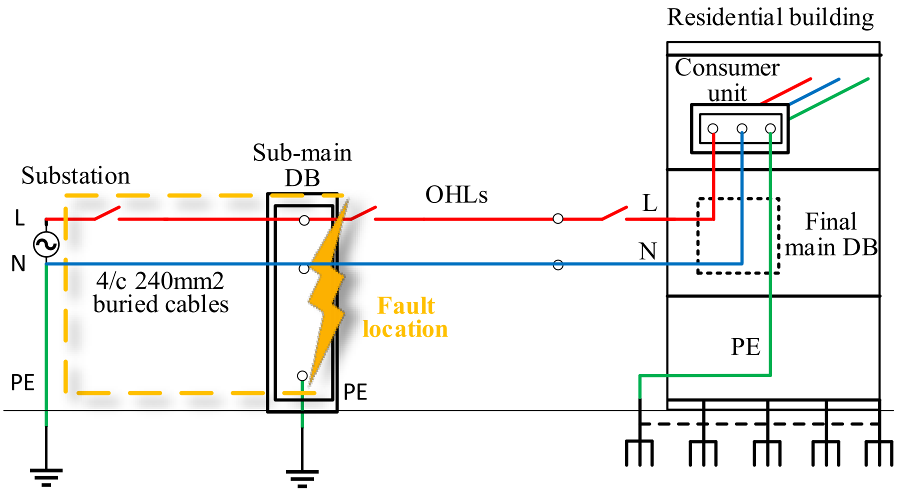

(a) simplified circuit diagram under a ground fault at the sub-main DB

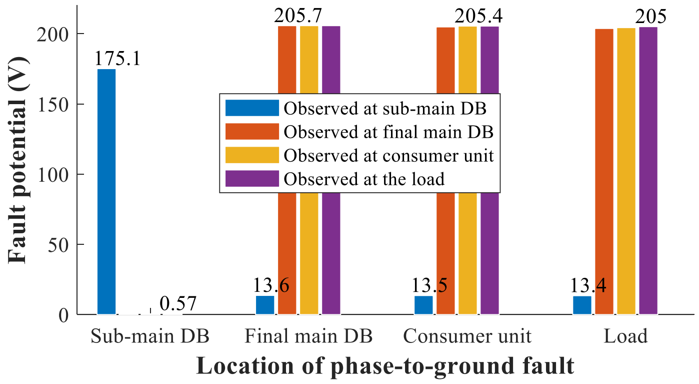

(b) Fault potential at four points caused by faults at four locations

Fig.4-5 TT grounding configuration.

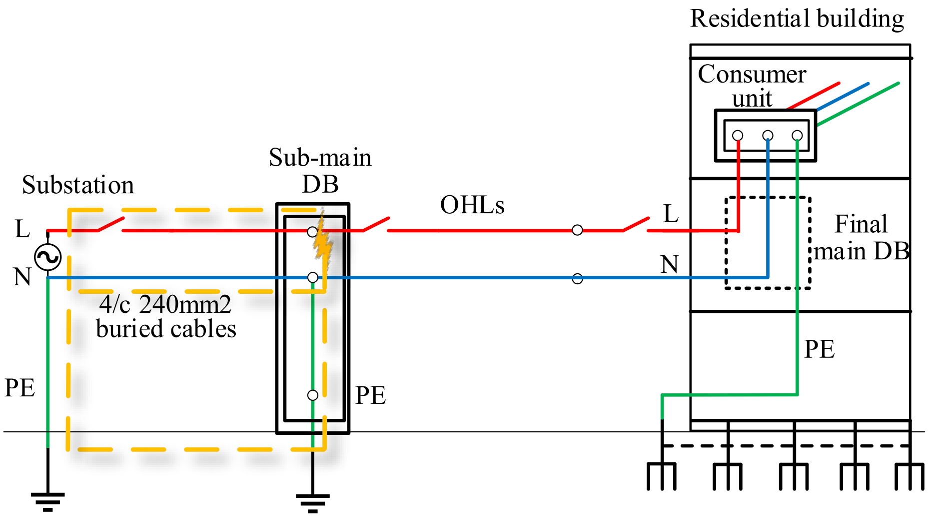

(a) simplified circuit diagram under a ground fault at the sub-main DB

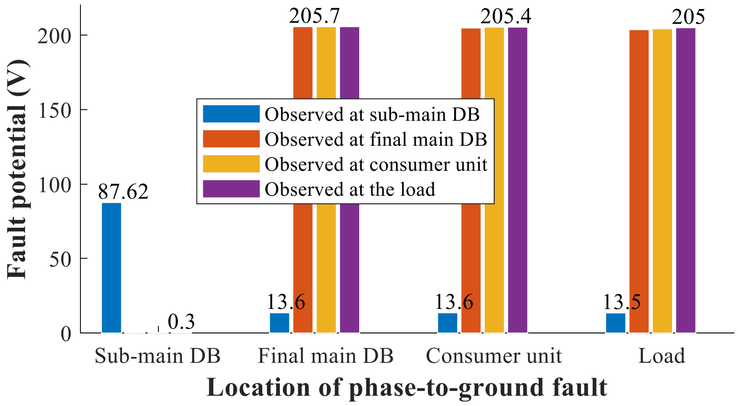

(b) Fault potential at four points caused by faults at four locations

Fig.4-6 In TT(M)-C-S grounding configuration

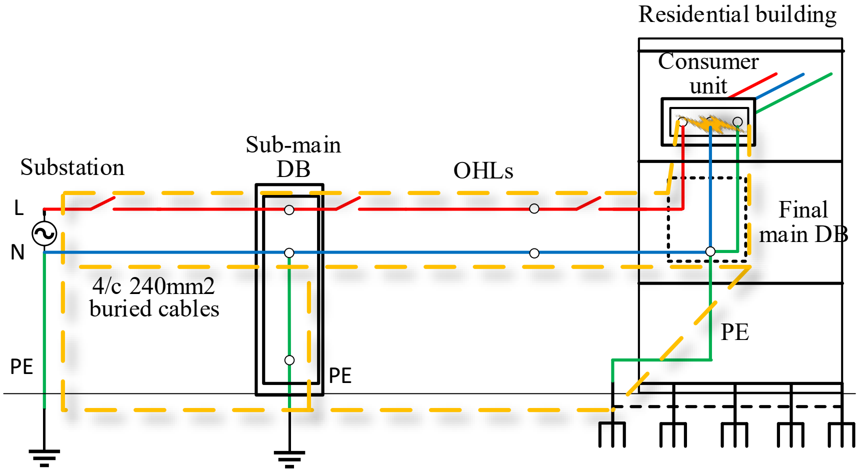

(a) simplified circuit diagram under a ground fault at the consumer unit

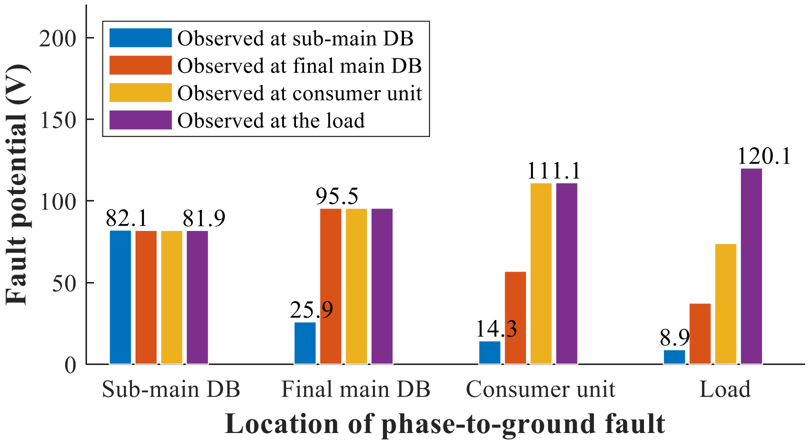

(b) Fault potential at four points caused by faults at four locations

Fig.4-7 TX(M)-C-S grounding configuration.

Under the TT grounding configuration, a ground-fault circuit may be composed of the transformer, the phase wire of a cable and/or an overhead line (OHL), the PE wire, the grounding electrode, and the substation grounding grid. This is illustrated in Fig.4-5(a) by the orange dashed arrows for the fault located at a sub-main DB. Note that the grounding impedance is a dominant part of this fault circuit. The equipment potential at the fault position remains high. Since a separate PE wire grounds the equipment of each section and is not connected to the N wire under this grounding configuration, the equipment potential in the non-faulted section is almost negligible. As for the faults located in the building, the equipment potential inside the building remains high because of the large grounding resistance of the vertical rod at the final-main DBs for a building. While the equipment potential at the sub-main DB is low as the N wire is not also connected to the PE wire in the building.

Fig.4-6(a) shows the simplified diagram of the fault circuit with the TT(M)-C-S grounding configuration, taking the fault located in the sub-main DB as an example. Note that the N wire is connected to the PE wire at the sub-main DB under this grounding configuration. Thus, under the fault at the sub-main DB, the equipment potential is determined by the total impedance of the N wire and the grounding electrode connected in parallel. This equivalent impedance is relatively low. Subsequently, the equipment potential is significantly small compared with that under the TT grounding configuration. As for the faults in the building, the results are similar to that under the TT grounding configuration.

Under the TX(M)-C-S grounding configuration, as shown in Fig.4-7 (a), the N wire is connected to the PE wire at both the sub-main DB and the final-main DB. Thus, even under the fault at the sub-main DB, the PE wire in the building carries the fault potential. Under the fault in the building, the equipment potential there is determined by the impedance of both N/PE wires and grounding electrodes connected in parallel. This equivalent impedance is significantly lower than the grounding resistance under the TT(M)-C-S or TT grounding configuration. Thus, the fault potential in the building is lower than that under the other grounding configurations.

It can be observed in the discussion that the ground fault in a building usually causes a high fault potential in the building. Whether the fault at the sub-main DB brings a high fault potential into the building depends on whether the connection of the N wire and the PE wire is made at the entrance of the building.

4.4.2 Line-to-neutral short circuit

This section assesses the equipment potential under the line-to-neutral (L-N) fault. Under the TT grounding configuration, the electrical connection between the PE and N wires is provided only at the substation. No fault potential would exist at all four observation points arising from the phase-neutral fault along the distribution network.

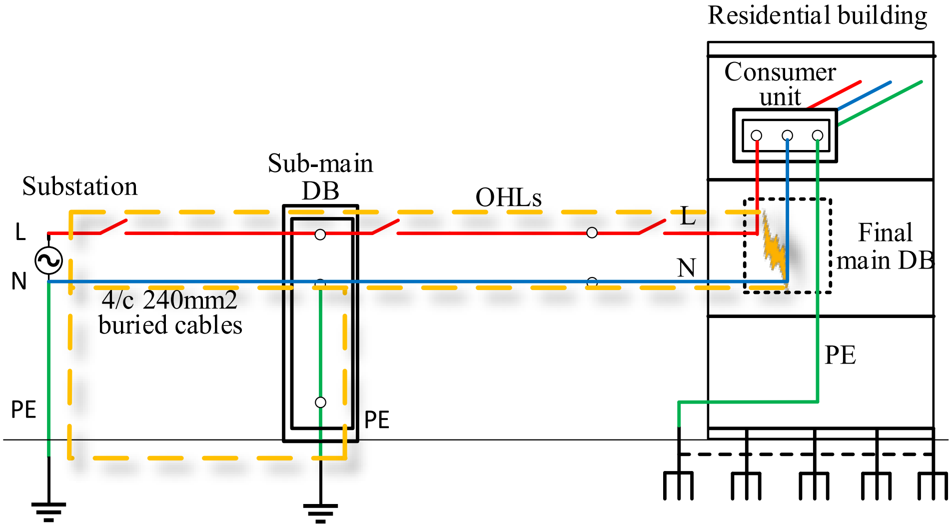

(a) The simplified circuit diagram under the L-N short circuit at the final-main DB

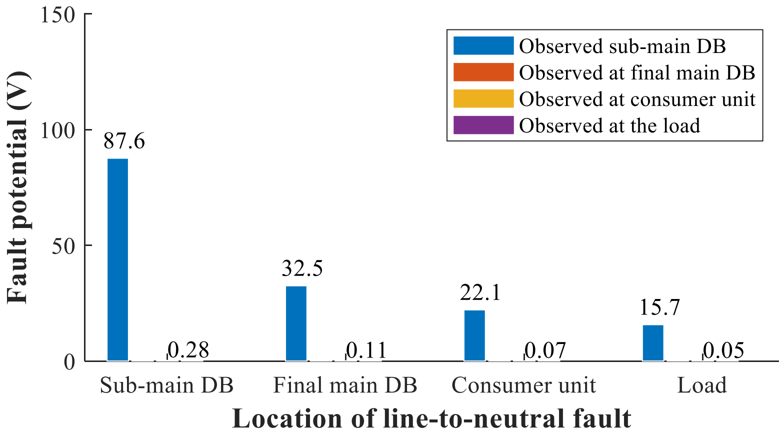

(b) Fault potential at four points caused by faults at four locations

Fig.4-8 TT(M)-C-S grounding configuration.

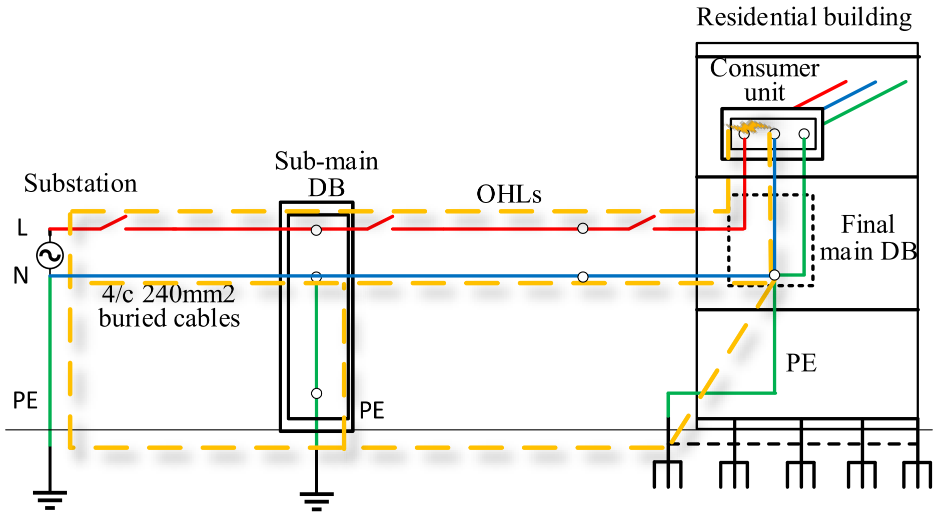

(a) The simplified circuit diagram under the L-N short circuit at the consumer unit

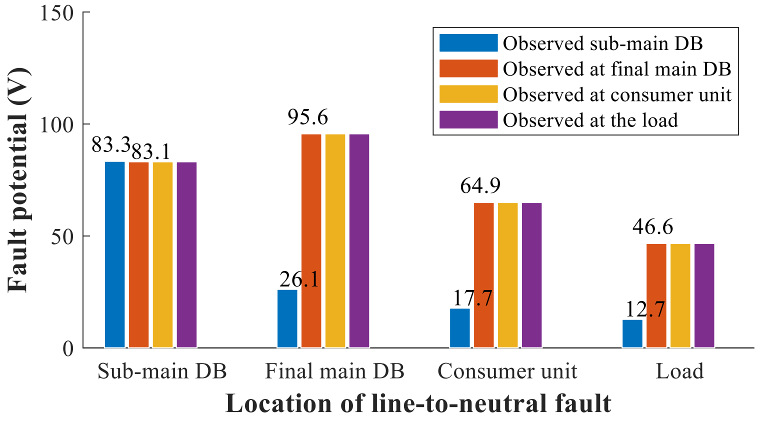

(b) Fault potential at four points caused by faults at four locations

Fig.4-9 TX(M)-C-S grounding configuration.

Under the TT(M)-C-S grounding configuration, the PE wire in the building is separated from the N wire, as shown in Fig.4-8(a). The L-N fault does not bring a fault potential into the observation points in the building (*i.e.*, the last three groups, as shown in Fig.4-8 (b)). In contrast, the equipment potential at the sub-main DB would rise due to the inner connection between the N wire and PE wire at this point. As the fault locations move from the sub-main DB towards the user equipment, the equipment potential at the sub-main DB gradually decreases, as shown in Fig.4-8(b). This is because the fault current decreases with increasing the total short-circuit impedance.

Fig.4-9(a) shows the simplified circuit diagram under the L-N fault with the TX(M)-C-S grounding configuration, taking the fault at the consumer unit as an example. Under this configuration, the PE wire in the building is connected to the N wire at the entrance of the building. Thus, the equipment carries the fault potential caused by the L-N fault occurring at all positions. Note that the N wire is connected in parallel with the grounding. The equivalent impedance of this line section is relatively low. Thus, the faults in the building would cause a lower fault potential than that under a P-G fault with the TX(M)-C-S configuration.

4.4.3 Neutral-line-open fault

Whenever the neutral wire of a three-phase distribution network is open, the N wire potential at the load side would be shifted due to the unbalanced loading among the three phases. In the assessment presented in this section, the neutral wire of a three-phase OHL is assumed to be broken. Generally speaking, the more significant unbalance of three-phase loading, the more considerable shift the N wire potential would have. Now consider a case in which the currents in the three-phase wires are respectively equal to 90%, 50%, and 10% of the design current (e.g., 48 A for a two-story building [22]). Equipment potential, in this case, is calculated by considering different grounding configurations. Table. 4-4 presents the fault potential at the sub-main DB and final-main DB caused by the neutral-line open. Since the PE wire is not connected to the N wire in a building with the TT or TT(M)-C-S configuration, the phase-line disconnection doesn't bring a fault potential to the PE wires. Subsequently, equipment potential remains zero at both the sub-main DB and final-main DB. While under the TX(M)-C-S configuration, the open N-wire fault would bring a significant fault potential to the equipment in the building, with a maximum value of 91.7 V at the final-main DB.

Table.4-4 The fault potential caused by the neutral-line-open fault at the sub-main and final-main DBs under different grounding configurations.

Measuring point **Grounding configurations**	Sub-main DB	Final-main DB
TT	0	0
TT(M)-C-S	0	0
TX(M)-C-S	6.07 V	91.7 V

A summary of the fault potential under different scenarios is provided below:

a) The observation point nearer the line-fault position has a higher phase-to-ground fault potential, while the fault potential decreases when the observation moves toward the end of the distribution network.

b) Generally speaking, a phase-to-ground fault potential at the line-fault position is relatively high once a fault is located in the building due to the high overall equivalent impedance in the fault circuit.

c) As for line-to-neutral short circuit and neutral-line-open fault, the fault potential distribution mainly depends on the specific grounding configurations.

4.5 Touch voltage assessment

In this section, the touch voltage under typical line-fault cases is further evaluated, as shown in Fig.4- 4. Since the fault current across the body could be discharged into the ground via non-dedicated conductors, the circuit model for a scenario of electric shock is required for the touch voltage evaluation.

4.5.1 Circuit model for electric shock scenarios

Two cases of electric shock in a building are of concern, shown in Fig.4-10(a). The first one is an indoor case in which a resident touches the metal enclosure of equipment grounded via a PE under a line fault. The equivalent circuit in this situation is illustrated in the right part of Fig.4- 10(c). The human body in the circuit is modeled by an equivalent impedance recommended by IEC 60990 standard [22], In as shown in Fig.4- 10(b). The RC between the human body and rebars in the concrete is represented with a lumped resistance and determined in the experiment mentioned in Section 3.1. Note that the worst case is of concern in this study, in which a person stands on a wet floor without wearing shoes. The steelwork in the building foundation serves as a grounding grid, the parameters of which are provided in Table.2.

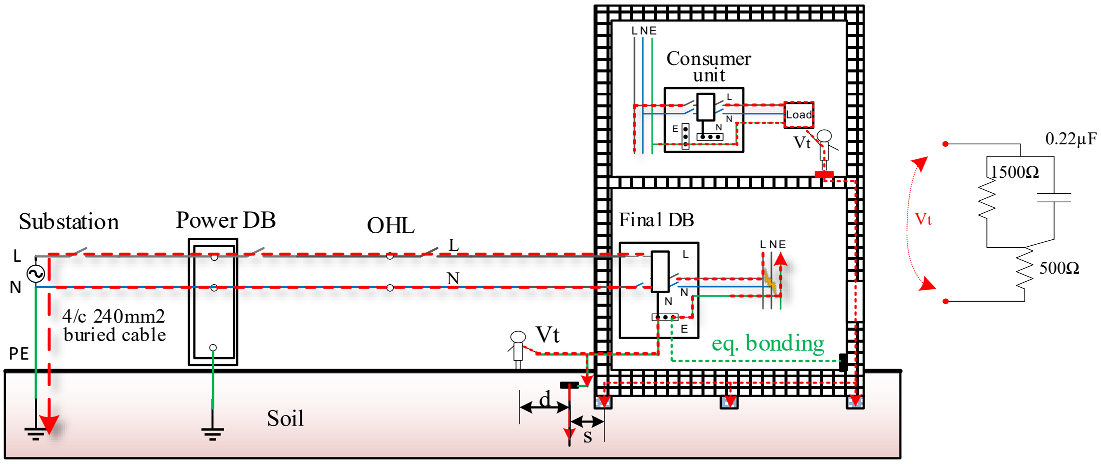

(a) Electric shock scenarios (b) Human body impedance

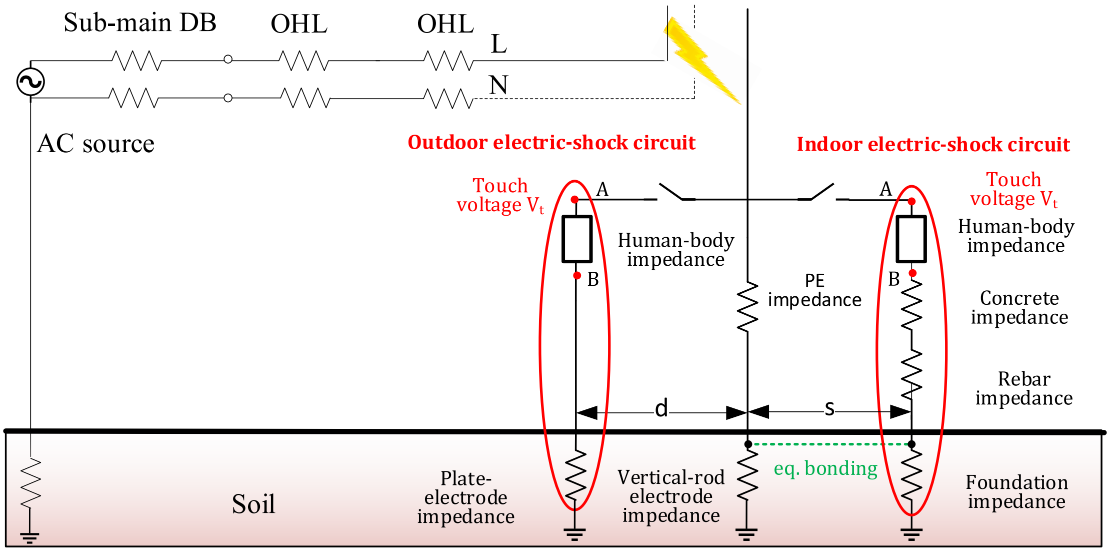

(c) Equivalent circuit of the indoor/outdoor scenarios of electric shock.

Fig.4-10 (a) Illustration of an electric shock happens indoors or outdoors (b) Human-body circuit recommended by IEC 60990 [22]. (c) Equivalent circuit of the indoor/outdoor scenarios of electric shock.

Table 5 Five cases of electric-shock positions concerned in simulation

Scenario number / Position	1	2	3	4	5
Standing point	Ground	Ground	RC floor within a building	RC floor inside a flat	RC floor inside a flat
Touch point	Metal enclosure				
	Sub-main DB	Final-main DB	Final-main DB	Consumer unit	User equipment

For the second case in Fig.4-10(a) and on the left side of Fig.4-10(c), a person touches the outdoor PE wire while standing on earth. The distance between the feet and the grounding electrode is *d*. The steelwork in the building foundation may or may not be bonded to the dedicated grounding electrode at the final-main DBs. These two parts have a separation distance *s*.

4.5.2 Touch voltage

In this part, the touch voltage that the human body suffers is investigated. Five scenarios of electric-shock positions and the circuit models for indoor/outdoor scenarios are under investigation. The specific scenarios are also shown in Fig.4-11, as illustrated in Table. 5. These five scenarios also indicate the locations for touch voltage observation.

Shown in Fig.4-11 is the distribution of the touch voltage under different P-G fault locations and the electric shock points with the TT grounding configuration. The value of each bar represents the amplitude under one combination and is labeled above the corresponding bar. Two plots are presented respectively for the cases with and without the eq. bonding. The eq. bonding is made by providing a wire connection between the grounding electrode and steelwork in the building foundation. The distance *s* between the two parts, as illustrated in Fig.4-10(a) and Fig.4-10(c), is fixed to be 0.2 m.

It can be observed in Fig.4-11 that the touch voltage without eq. bonding at the building remains high in the electric shock scenarios nearby or inside a building (case (b) to case (d)) for the fault located in the building. The measure of eq. bonding provided at the building can effectively reduce the touch voltage nearby or inside the building, but cannot at the sub-main DB. Note that with eq. bonding provided at the building, the overall grounding impedance of a building decreases significantly. Accordingly, the fault potential and touch voltage at the case (a) location, *i.e.*, sub-main DB, increase substantially.

Fig.4-12 shows the touch voltage underground faults in the network with the TT(M)-C-S configuration. It is found that the touch voltage has a similar distribution to that under the TT grounding configuration. Again, the measure of eq. bonding can reduce the touch voltage nearby or inside the building, but the reduction is ineffective in electric shock at the sub-main DB.

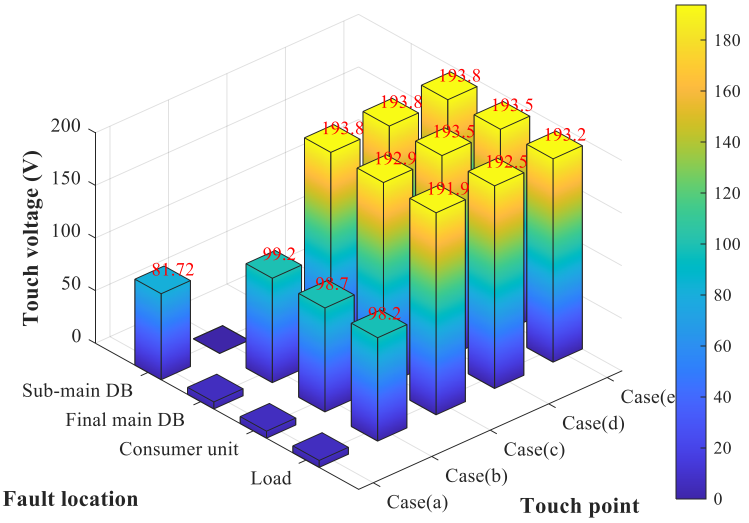

(a) without eq. bonding

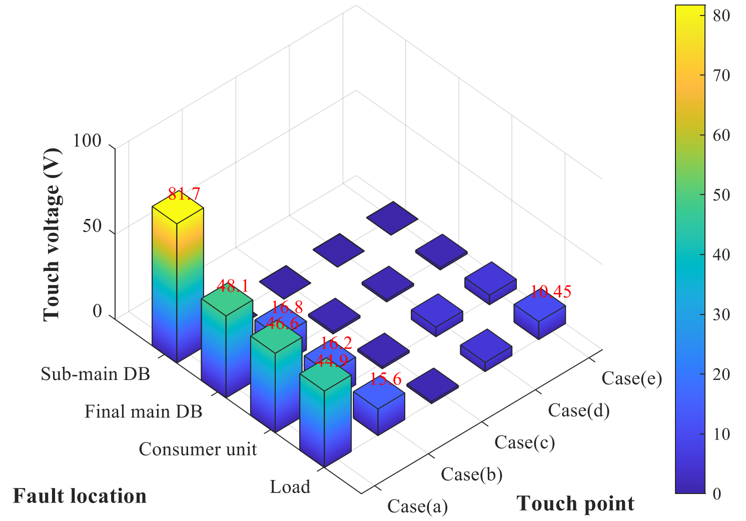

(b) with eq. bonding,

Fig.4-11 Touch-voltage distribution under different cases, with P-G faults and TT grounding configurations.

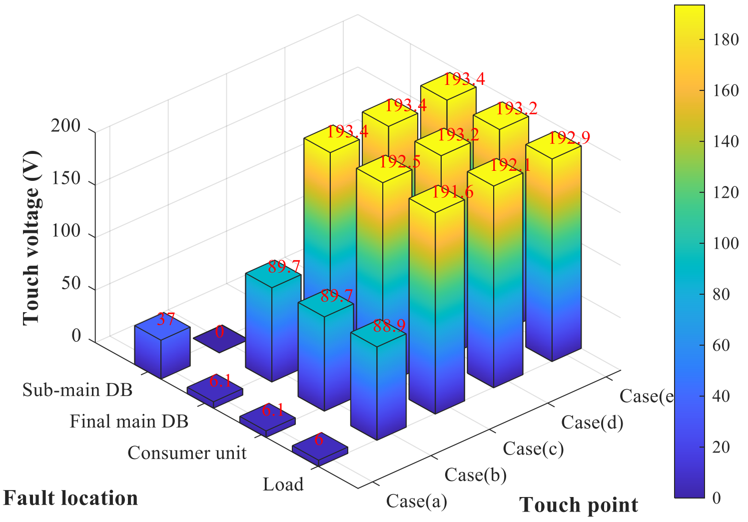

(a) without eq. bonding

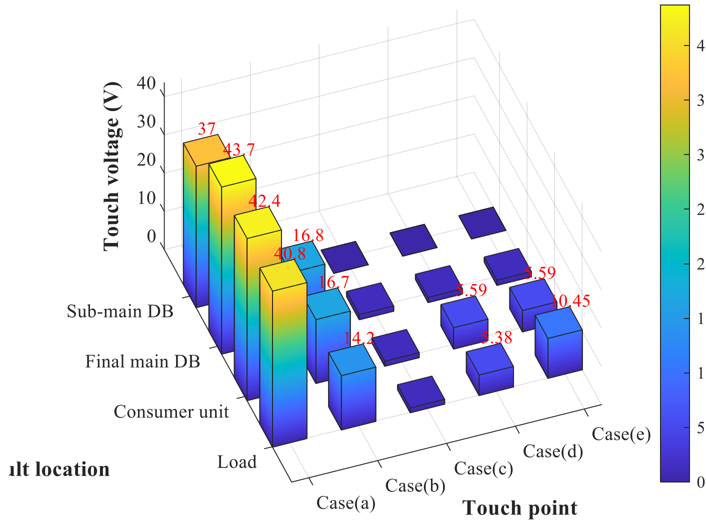

(b) with eq. bonding,

Fig.4-12 Touch-voltage distribution under different cases, with P-G faults and TT(M)-C-S grounding configurations.

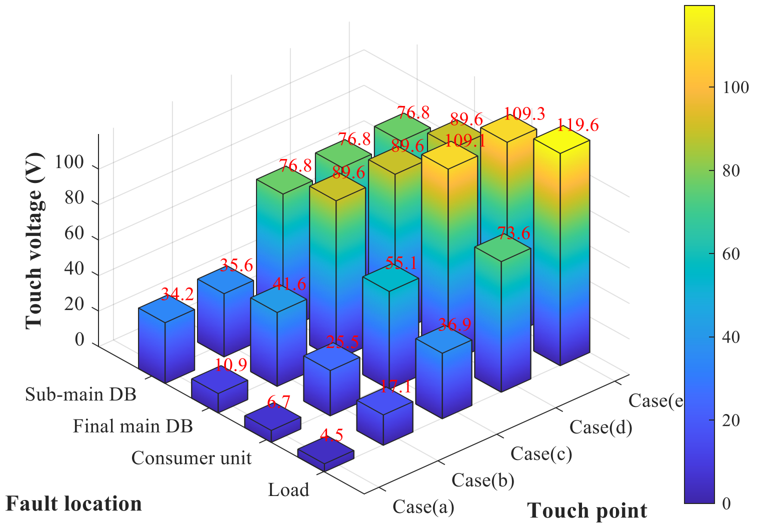

(a) without eq. bonding

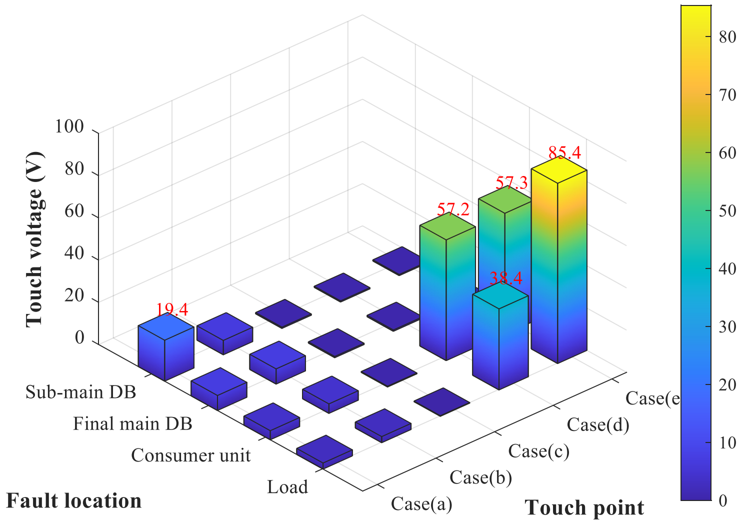

(b) with eq. bonding

Fig.4-13 Touch-voltage distribution under different cases, with P-G faults and TX(M)-C-S grounding configurations.

Shown in Fig.4-13 is the distribution of the touch voltage when P-G faults happen at different locations and the electric-shock points in the network with the TX(M)-C-S grounding configuration. It is evident that the touch voltage is higher in the indoor scenarios (case (c) and (d)) for the fault inside the building. Different from that under the other two grounding configurations, the measure of eq. bonding could mitigate the touch voltage, although this mitigation may not be obvious. This is because the resistance of the PE wire within the building becomes dominant. The measure of eq. bonding, however, reduces the touch voltage significantly in the electric shock scenarios outside the building under the fault at all the possible locations and in all the electric-shock scenarios under the fault at the final-main DB or its upstream. It is clear that to reduce the touch voltage within the building further, it would be necessary to provide local eq. bonding within the building.

Fig.4-14 & 15 show the touch voltage when L-N faults happen. Since there is no fault potential in the distribution network with the TT configuration, only the simulated results with the TT(M)-C-S and TX(M)-C-S are presented in these figures, respectively. It is found in Fig.4-14 that in most cases, the line fault under the TT(M)-C-S configuration wouldn't generate dangerous touch voltage. It is because the PE wire is not connected to the neutral line at the final-main DB of the building. Also, in this case, the measure of eq. bonding does not make any meaningful difference in the touch voltage. It can be observed in Fig.4-15 that the touch voltage can be higher than that under the TT(M)-C-S configuration, due to the parallel connection of the N wire and PE wires under this configuration. It is also found the great protective effect of eq. bonding against touch voltage in case of electrical shock.

Fig.4-16 shows the touch voltage under a neutral-line-open fault. Since no fault potential is generated in both the TT and TT(M)-C-S configurations, only the simulated results with the TX(M)-C-S configuration are presented. The fault is assumed to be located at the outdoor line section. The results are presented against the measure of eq. bonding and the distance *d* between the feet of a person and the electrode with fault potential (when a person is electrocuted outside a building). It is found that without eq. bonding the line fault with TX(M)-C-S configuration would generate dangerous touch voltage in most cases. The farther distance *d* brings a higher touch voltage outside the building, as shown in case (b) w/o eq. bonding. The measure of eq. bonding may eliminate the dangerous touch voltage in all cases in or around the buildings, while it would cause a transfer voltage at the sub-main DB.

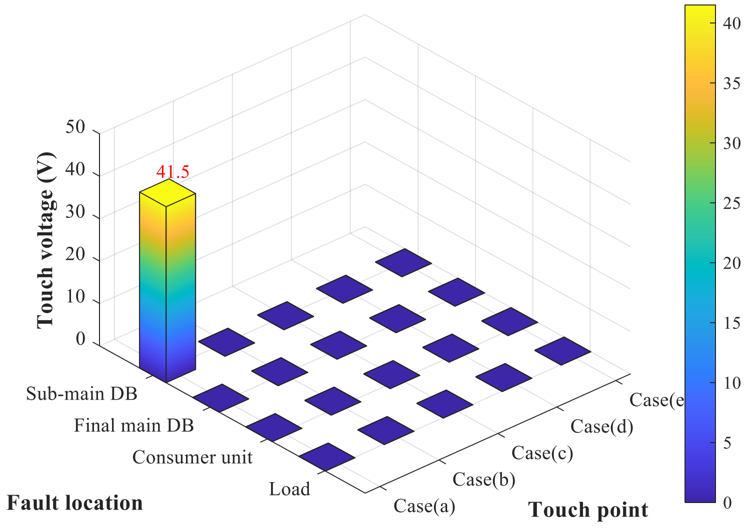

(a) without eq. bonding

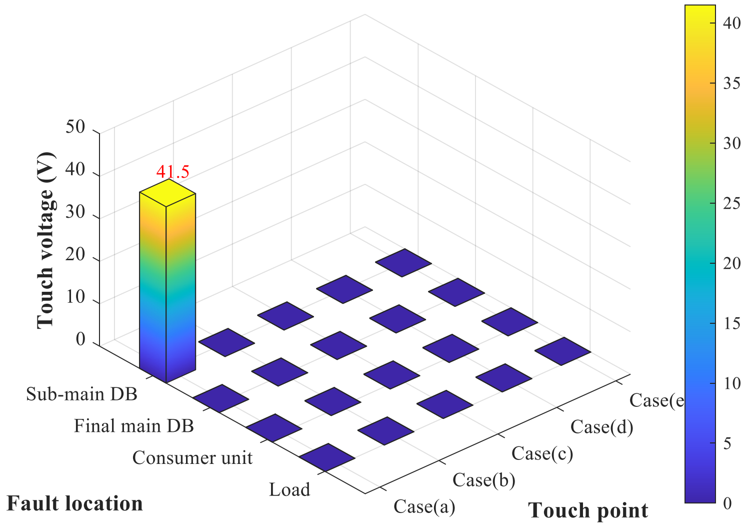

(b) with eq. bonding

Fig.4-14 Touch-voltage distribution under different cases, with phase fault and TT(M)-C-S grounding.

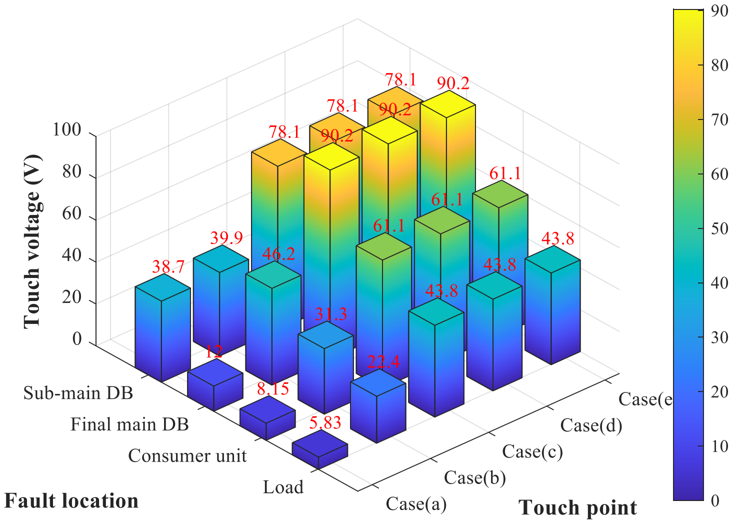

(a) without eq. bonding

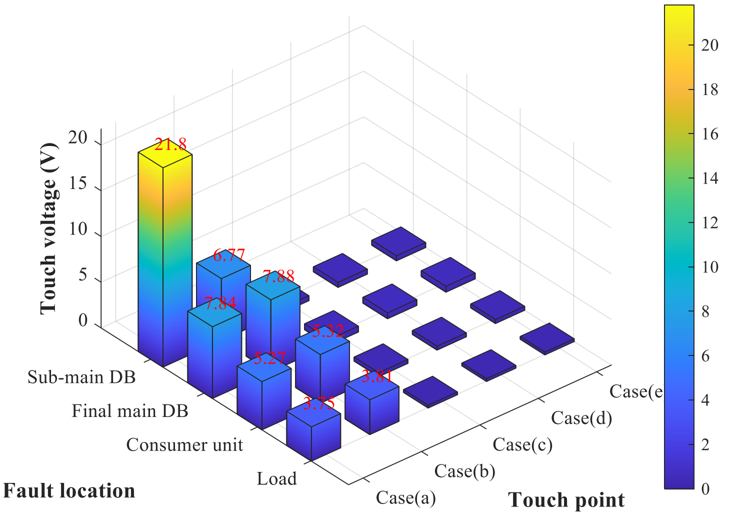

(b) with eq. bonding

Fig.4-15 Touch-voltage distribution under different cases, with L-N fault and TX(M)-C-S grounding.

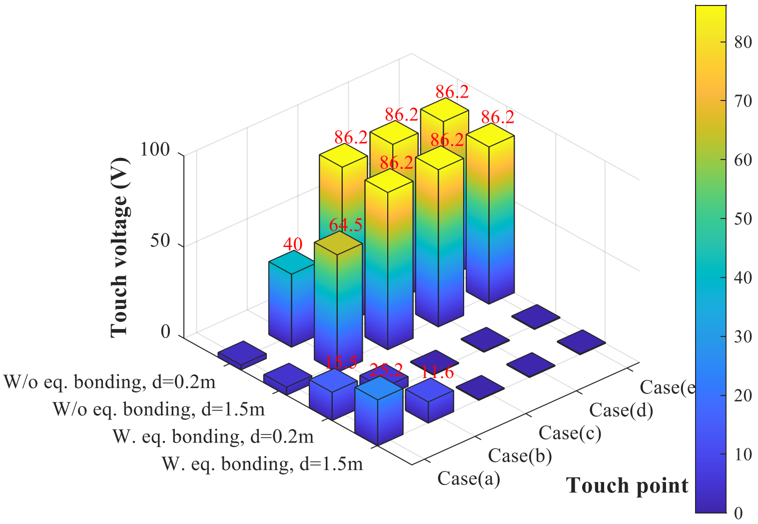

Fig.4-16 Touch-voltage distribution under different cases, with neutral-line-open fault and TX(M)-C-S grounding.

4.5.3 Discussion of the dangerous touch voltage

Touch voltages under different combinations of electric shock points and fault locations are summarized in Table. 4-6 to Table. 4-9. Note that in Section 4.2 the distance between the building foundation and the grounding rod is fixed at 0.2 m, while in these tables the distance in a range of 0.2~1.5 m is considered. The upper limit of a touch voltage range in the table corresponds to the distance of 1.5 m, due to the larger potential difference between point A and point B, as shown in Fig.4-10 and Fig.4-4.

It is noted that the limit of a safe touch voltage has been investigated by related standard files and research [23-25]. Touch voltage exceeding that level could be dangerous. This paper adopts a strict threshold of 24 V for safe touch voltage. A touch voltage valued over 24 V is classified as a “dangerous touch voltage”. A summary of the distribution of dangerous touch voltage is provided below:

a) Under a P-G fault, the touch voltage is higher when the observation point is close to the fault location and decreases near the distribution network’ far end.

b) The measure of equal potential bonding could mitigate the touch voltage nearby or inside the building, while this mitigation may not be effective under the electric shock scenarios at the sub-main DB. Under the TT and TT(M)-C-S grounding configurations, the eq. bonding at the building could generate a dangerous touch voltage to be transferred to the sub-main DB under a P-G fault in the building.

c) Under an L-N fault, the TT grounding configuration does not cause a dangerous touch voltage. The TT(M)-C-S grounding configuration has a dangerous touch voltage only in one case, *i.e.*, the case with both the line fault and observation points at the sub-main DB. With the TX(M)-C-S grounding configuration, most of the dangerous cases due to this fault could be addressed by an eq. bonding inside the building.

d) Under an N-wire-open fault, both the TT and TT(M)-C-S grounding configurations do not generate the situation with dangerous electric shock, while with the TX(M)-C-S, there will be dangerous touch voltage in the building if the eq. bonding is not provided.

Table 4-6 Touch voltage under different cases of electric shock point and fault location (TT)

		P-G fault					P-N short circuit
	Touchpoint / Fault location	Case a	Case b	Case c	Case d	Case e	All cases of touching
W/o eq. bonding	Power DB	81.7~134.1	Safe	Safe	Safe	Safe	Safe
	Final main DB	Safe	99.2~161.3	193.8	193.8	193.8	
	Consumer unit	Safe	98.7~160.6	192.9	193.5	193.5	
	Load	Safe	98.2~159.7	191.9	192.5	193.2	

W. eq. bonding	Power DB	81.7~134.1	Safe	Safe	Safe	Safe	Safe
	Final main DB	48.1~78.9	16.8~36.6	Safe	Safe	Safe	
	Consumer unit	46.6~76.5	16.2~35.8	Safe	Safe	Safe	
	Load	44.9~73.7	15.6~34.2	Safe	Safe	Safe	

Table 4-7 Touch voltage under different combinations of electric shock point and fault location (TT(M)-C-S)

	Type of faults	P-G fault					P-N short circuit	
	Touchpoint / Fault location	Case a	Case b	Case c	Case d	Case e	Case a	Case b~e
W/o eq. bonding	Power DB	37~60.5	Safe	Safe	Safe	Safe	41.5~68.0	Safe
	Final main DB	Safe	89.7~144.7	193.4	193.4	193.4	Safe	Safe
	Consumer unit	Safe	89.7~144.7	192.5	193.2	193.2	Safe	Safe
	Load	Safe	88.9~143.3	191.6	192.1	192.9	Safe	Safe
W. eq. bonding	Power DB	37.0~60.2	Safe	Safe	Safe	Safe	41.5~68.0	Safe
	Final main DB	43.7~71.2	16.8~32.6	Safe	Safe	Safe	Safe	Safe
	Consumer unit	42.4~68.9	16.7~31.8	Safe	Safe	Safe	Safe	Safe
	Load	40.8~66.4	14.2~30.7	Safe	Safe	Safe	Safe	Safe

Table. 4-8 Touch voltage under different combinations of electric shock point and fault location (TX(M)-C-S).

		P-G fault					L-N short circuit		
	Touchpoint Fault location	Case a	Case b	Case c	Case d	Case e	Case a	Case b	Case c~e
W/o eq. bonding	Power DB	34.2~56.2	35.6~57.5	76.8	76.8	76.8	38.7~63.6	39.9~65.0	78.1
	Final main DB	Safe	41.6~67.3	89.6	89.6	89.6	Safe	46.2~75.1	90.2
	Consumer unit	Safe	25.5~41.3	55.1	109.1	109.3	Safe	31.3~50.9	61.1
	Load	Safe	17.1~27.7	36.9	73.6	119.6	Safe	22.4~36.5	43.8
W. eq. bonding	Power DB	19.4~31.3	Safe	Safe	Safe	Safe	21.8~35.7	Safe	Safe
	Final main DB	Safe	Safe	Safe	Safe	Safe	Safe	Safe	Safe
	Consumer unit	Safe	Safe	Safe	57.2	57.3	Safe	Safe	Safe
	Load	Safe	Safe	Safe	38.4	85.4	Safe	Safe	Safe

Table. 4-9 Touch voltage under different electric shock scenarios with a neutral-line-open fault (TX(M)-C-S).

		Neutral-line disconnection				
	Touchpoint	Case a	Case b	Case c	Case d	Case e

	Fault location					
W/o eq. bonding	Sub main circuit	Safe	40.0~64.5	86.2	86.2	86.2
W. eq. bonding		15.5~25.2	Safe	Safe	Safe	Safe

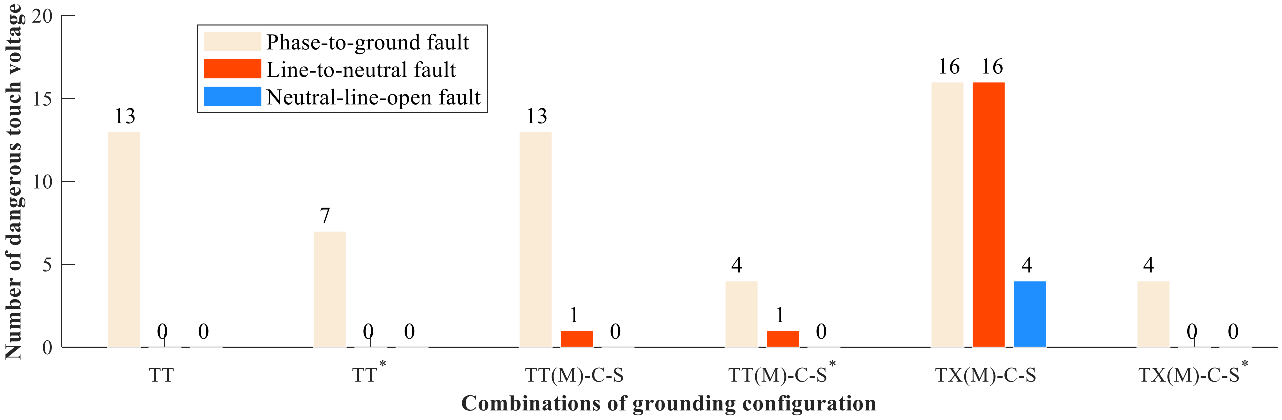

Fig.4-17 Number of electric shock scenarios with dangerous touch voltage, under different grounding configurations. (* represents the case with eq. bonding)

The number of electric shock scenarios with dangerous touch voltage is collected and compared, as shown in Fig.4-17. It is evident that the P-G fault is the most dangerous, while the neutral-line-open fault is the least dangerous. Whenever there is not any eq. bonding provided between the building foundation and the grounding grid, the TT grounding configuration leads to the lowest number of hazardous scenarios, and the TX(M)-C-S the most number. The measure of eq. bonding can significantly decrease the number of dangerous scenarios for all the grounding configurations, which also means the reduction of the frequency of occurrence. This measure makes the TX(M)-C-S the best choice.

4.6 Step voltage assessment

The typical grounding configuration in an electric power distribution system includes the vertical electrode, the horizontal electrode and the fork-type grid, as shown in Fig.4-18. In this simulation, the length of vertical electrode is 3m. The length of horizontal electrode is 2.5m and the buried depth is 0.5m. The fork-type grid has three vertical electrodes and the buried depth is 0.5m. The radius of all the electrodes is 0.01m.

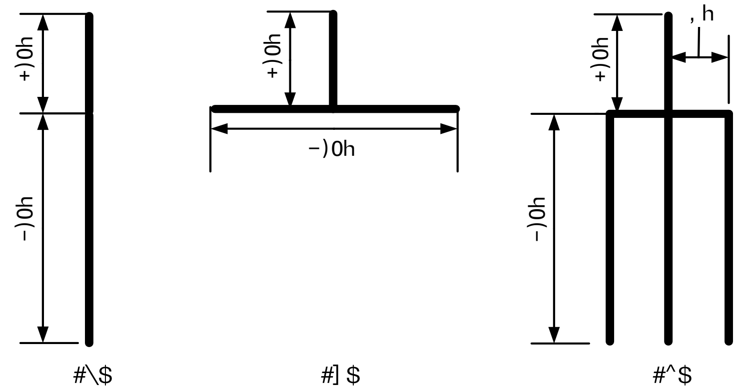

Fig. 4-18 (a) Vertical Electrode (b) Horizontal Electrode (c) Fork-type grid

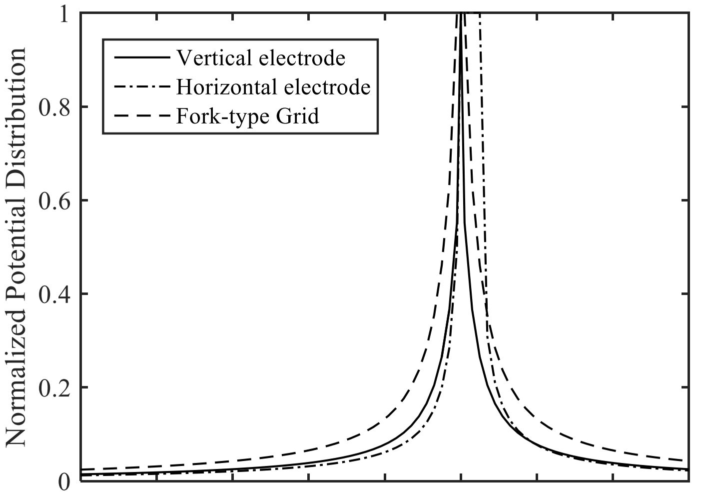

Fig. 4-19 The potential distribution ratio for different grounding configurations.

Table. 4-10 Step voltage at the vicinity of fork-type grid

Distance (m)	Step voltage (V)
0.5	80.1
1.5	118.6
2.5	142.1

The simulation result of ground potential distribution under phase-to-earth fault is shown in Fig.4-19. The normalized potential distribution is introduced as the ratio of the ground surface potential over the potential distribution around the electrode/grid varied significantly with distance. It is found that the fork-type grid has the smallest potential drop ratio in its vicinity. The horizontal and vertical electrode have a similar ground potential distribution curve. In table.1 is the step voltage in the vicinity of the fork-type grid. It is found that even with 0.5m from the grid, the step voltage is still higher than the human safety voltage.

As shown in Fig.4-20 and Fig.4-21, the TT or TN-C power supply mode are respectively analyzed for a typical electric distribution system. The overhead line is a three-phase four-wire power supply mode without a PE line. Overhead lines are connected to the building through a secondary distribution box. In a TT system, both the power distribution box and the building are grounded directly through the PE line. In a TN-C system, both the power distribution box and the building are grounded through the PEN line, which is the combination of the N line and PE line in a TN-C system.

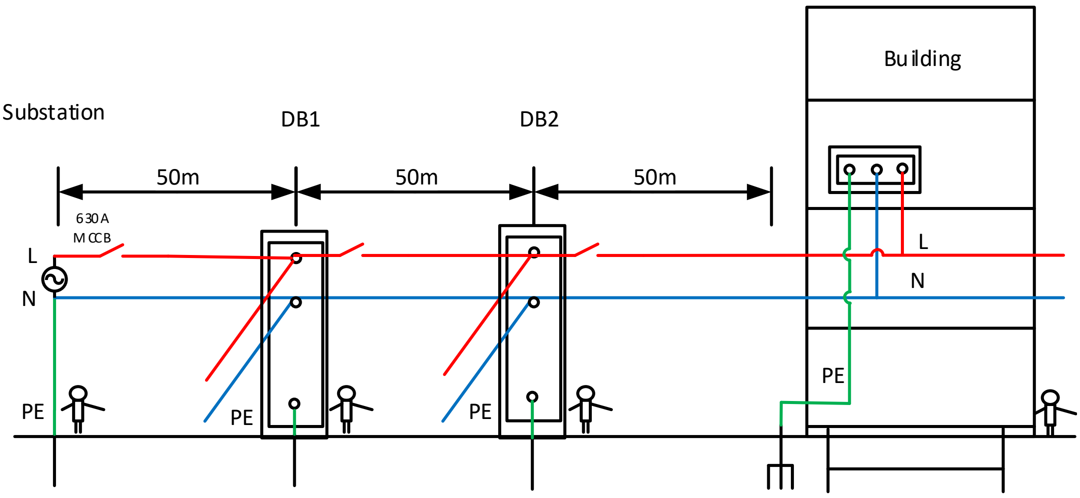

Fig. 4-20 a typical configuration of the TT system

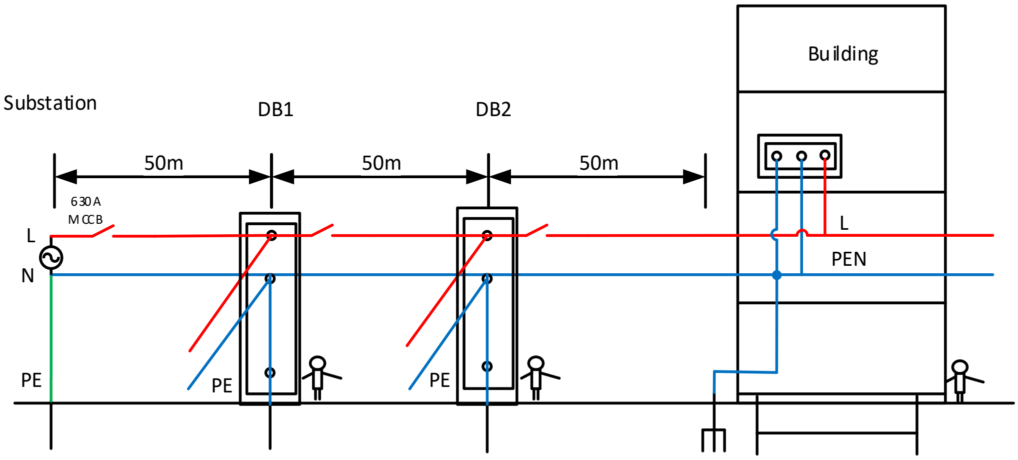

Fig. 4-21 a typical configuration of the TN-C system

Table. 4-11 Touch voltage for TT or TN-C system under phase-to-earth fault

Fault location	Power supply mode	*Voltage at DB*	*Voltage at building*

		(Step distance 0.2m-1.5m)	*(Step distance 0.2m-1.5m)*
DB	TT	75.6~125.9V	Safety
	TN-C	89.2~109.2V	Safety
OHL	TT	Safety	Safety
	TN-C	Safety	Safety
Building	TT	Safety	136.5~176.3V
	TN-C	Safety	49.4~92.6V

Table. 4-12 Touch voltage for TT or TN-C system under phase-to-neutral fault

Fault location	Power supply mode	*Voltage at DB* *(Step distance 0.2m-1.5m)*	*Voltage at building* *(Step distance 0.2m-1.5m)*
DB	TT	Safety	Safety
	TN-C	Safety	Safety
OHL	TT	Safety	Safety
	TN-C	Safety	Safety
Building	TT	Safety	48.2~62.1V
	TN-C	Safety	48.2~62.1V

The short circuit fault may happen at the distribution box (BD), overhead line (OHL) or the building. The touch voltage under phase-to-earth and phase-to-neutral fault are respectively shown in table.4-11 and table.4-12. It is found that the risk area for TT or TN-C system are the same. However, the touch voltage in a TN-C system is generally lower than the TT system. If only the electric shock area and touch voltage magnitude are taken into consideration, the TN-C system is a better choice than the TT system. But in a practical system, the protective devices are installed. This requires a more comprehensive study.

4.7 Analysis of Fault Potential in a Real Urban Old Community

4.7.1 The Overall line topology and LV system components

Fig.4-22 is a map and corresponding circuit diagram of a LV (low-voltage) distribution system for an real old residential community located in Shenzhen, China. Both the CAD map and the topology of the concerned line system are presented in Fig.4-22. The distribution circuit is made by a 10kV/380V transformer, a buried four-core (4/c) armored cable to an outdoor distribution board, and then overhead lines, labeled as submain OHL I and submain OHL II and presented in different colors in Fig.4-22, are equipped to the final main distribution boards (DBs) in multi-tenant low-rise buildings. Note that the submain circuit I and II have different two cross-section area (CSA) and the circuit II is nearer from the buildings than circuit II. The circuits in a building are connected to the individual units via single-core (1/c) PVC cables, finally to the individual user equipment.

Table. 4-13 Distribution equipment and its parameters for fault evaluation

Circuit component	Power equipment	Configurations	
Power Source	Distribution transformer	10kV/0.4kV,800kVA Z_t=6%	
Main circuit	Buried 4/c XLPE/SWA/PVC cable	Line	Length:250m, CSA: 240mm^2
		PE	Length:250m, CSA: 308mm^2
Submain OHL I	Overhead line	CSA: 185mm^2 Height: 3m Conductor spacing: 0.1m	
Submain OHL II	Overhead line	CSA: 35mm^2	

		Height: 3m Conductor spacing: 0.1m	
Final main circuit (inside buildings)	1/c PVC cables	Line	Length:20m, CSA: 10 mm^2
		PE	Length:20m, CSA: 6 mm^2
Final circuit (inside flats)	1/c PVC cables	Line	Length:20m, CSA: 4mm^2
		PE	Length:20m, CSA: 2.5 mm^2

Table. 4-13 provides the typical configurations of the line-circuit components adopted. Note that in the line-system modeling, the submain OHL I and submain OHL II adopt the real length and topology structure, while the cables inside the building and inside the flats adopt the same CSA configuration but with a fix length for simplicity.

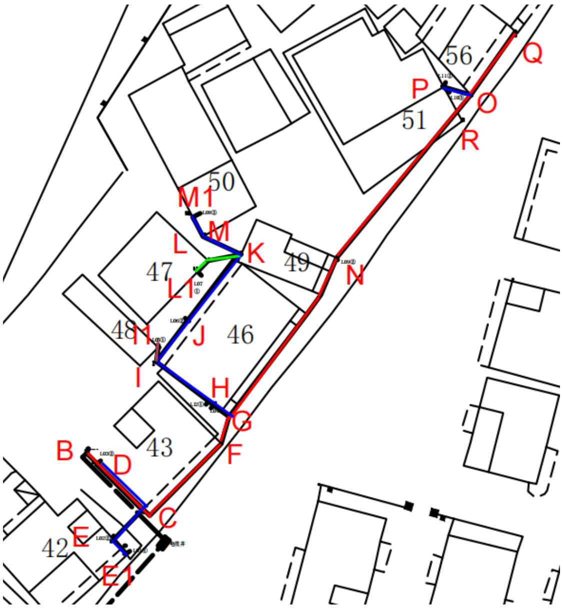

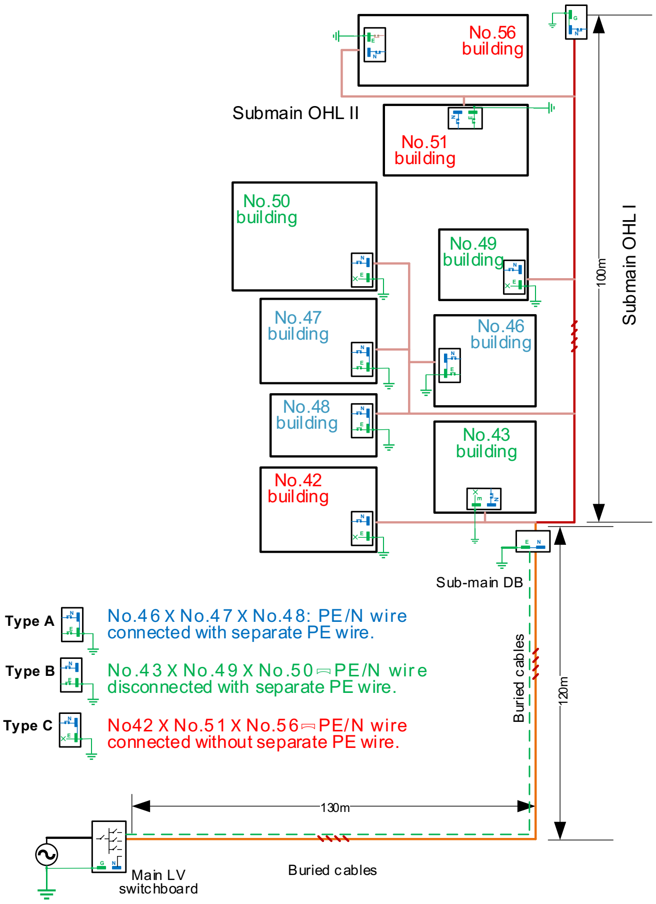

Fig.4-22 CAD Map and the topology of the concerned LV distribution line system in the old urban community for the case study.

4.7.2 Grounding configurations and main components of the LV line system

A typical circuit diagram for the specific line component and their grounding conditions has been shown in Fig.4-23. At each component of the LV distribution line system, the grounding protection should be implemented with different measures. For the 10kV/380V transformer in the substation, the grounding grid is always adopted for a low grounding resistance. According to the standard code, a value of 2 ohms is suitable for the case study in the simulation. As for sub-main distribution box (DB) at the connection point between the buried cable and the overhead lines, as well as the final main DB, a combined grounding electrode with both vertical and horizontal rods is used for the grounding of the power equipment and the protective-earth wire (PE wire). The parameters for the rods are introduced in Table. 4-14. Also, its corresponding equivalent low-frequency grounding impedance in the condition of 0.01 soil conductivity calculated using the PEEC model and numerical simulation is given. Besides the standard configurations of the grounding electrodes provided by the power company, the equivalent low-frequency grounding impedance versus the vertical-rod depth and the rod radius is presented in Fig.4-23.

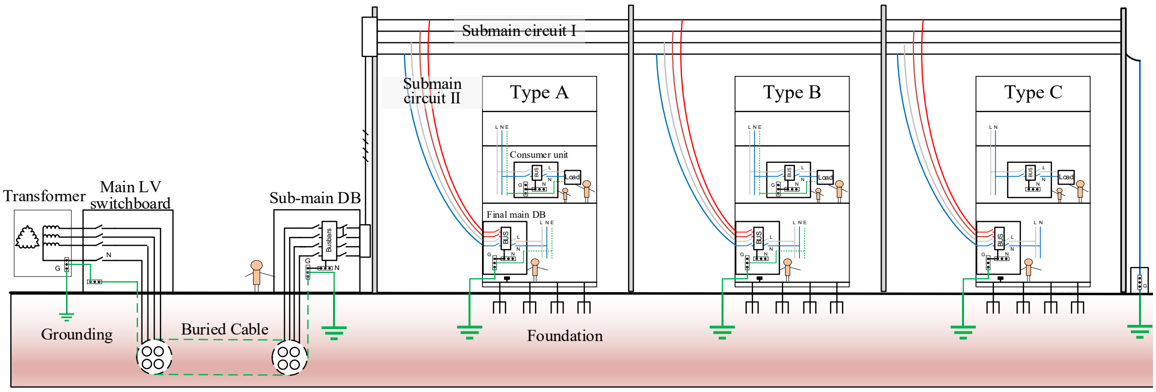

Fig.4-23 Circuit diagram of the concerned LV distribution line system and the three protective grounding (PE) methods, *i.e.*, type A, type B, and type C in the study case.

In residential buildings, the foundations have a more complex reinforcing structure with the concrete materials. The specific size of the steelwork of the foundation and its legs are presented in Fig.4-24. Because of the complexity of the modeling, in our study, we equate each reinforcing branch of the complex steel structure to a single-branch lumped resistance, which is then brought into the PEEC model. In this measure, the obtained total equivalent LF grounding impedance is about 2.04 ohms, which is nearly consistent with the actual measured results carried by the power company. Note that the measured soil conductivity is adopted as 0.01 S/m and the value adoptation is also based on the regular grounding measurement of the residential community. which is nearly consistent with the actual measured results.

Table. 4-15 Electrode parameters for different sections of a typical residential LV distribution network.

Grounding Location	Conductor Configuration	Equivalent LF grounding impedance
Substation	Grounding grid of the substation with a measured resistance of 2 ohms	2 ohms
Sub-main DBs and final-main DBs	Vertical conductor: Number:1; Length : 1.5m; Radius: 0.008 m; Horizontal conductor: Number:2; Depth: 0.8m; Length: 1.5m; Radius: 0.008 m;	26.2 ohms

Buildings	Up-layer reinforcing mesh: 0.95m length，Diameter:0.016 m, Number:8×8, Interval: 0.150 m Middle-layer reinforcing mesh: 1.45 m length, Diameter:0.016 m, Number:11×11, Interval: 0.150 m Middle-layer reinforcing mesh: 1.95 m length, Diameter:0.016 m, Number:14×14, Interval: 0.150 m	2.04 ohms

There are three regular grounding protective (PE) methods applied in the concerned residential community for the case study, as have been distinguished via different colors and labels in Fig.4-25. The main difference is that in the final main DB at the entrance of the buildings, Type A makes the PE wire connected with the N wire and Type B makes then disconnected. From the final main DB toward the final load in the users' flats, Type B and Type C adopts a separate PE wire or not. On the one hand, the difference in the PE method affects the grounding conditions when a line fault occurs, thereby impacting the absolute value of the line fault, such as phase-to-ground fault. On the other hand, the fault-potential transfer mainly depends on the PE wire. As humans are often prone to touching equipment housings or bare conductors connected to PE wires, the PE method determines the fault distribution and the possible exposure risk for the humans.

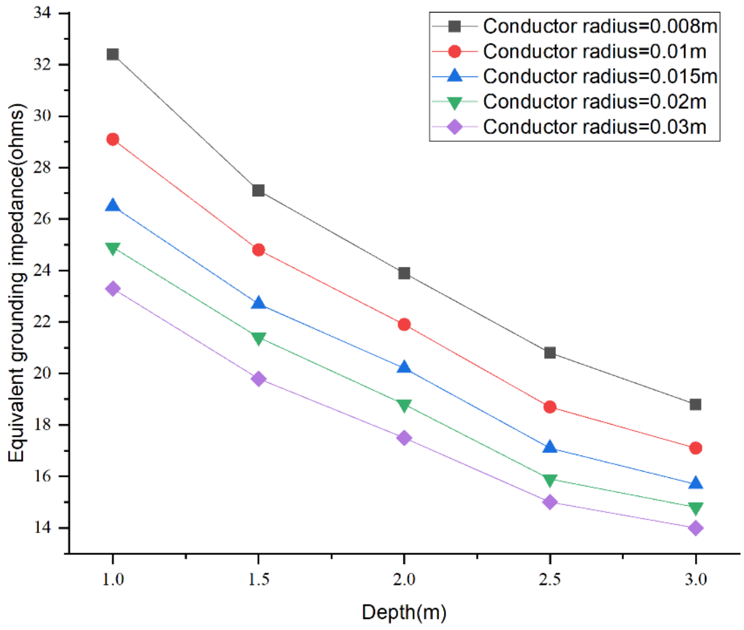

Fig.4-25 The equivalent LF grounding impedance of the grounding electrodes versus the vertical depth and the rod radius for the distribution box and the PE wires along the distribution line system.

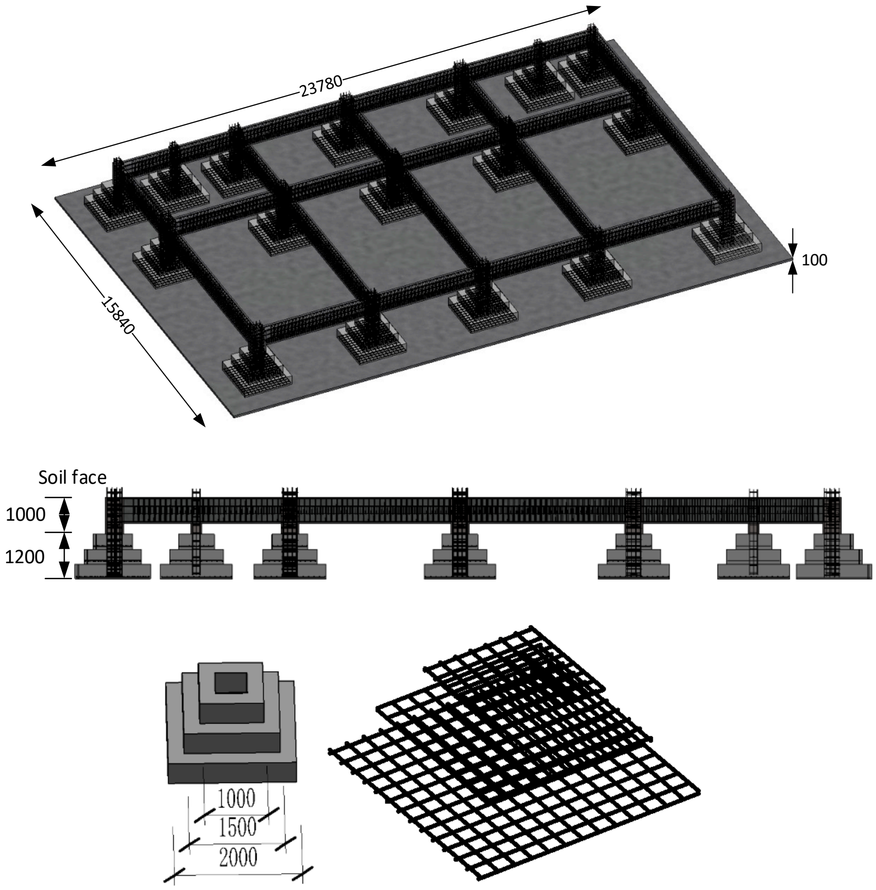

Fig.4-26 Size of the steel work of the foundation and its legs

Based on the modeled LV distribution line system for the concerned residential community, the fault potential under the most typical line fault conditions is assessed and analyzed in this section. Different from the ideal single-building case in the past studies [16-17], there are variations in the PE methods of different buildings, which are in different parts of the line topology network. Thus, all the possible fault locations are of concern for simulation. Since a human body is likely to touch the metal box of the power equipment or the electrical conductors, as briefly presented in Fig.4-26, all the possible locations have been set as the conditions of the fault positions and the measured positions. Three fault positions outside the residential buildings, i.e., the cases of the fault at sub-main DB, submain OHL I, and submain OHL II, and three faults positions inside the buildings, i.e., the fault at final main DB, consumer unit, and load, have been concerned in the simulation.

A. *Fault-potential assessment under the conditions of phase-to-ground line fault*

The fault potential under the most typical phase-to-ground line fault conditions is first assessed in this part. Fig.4-27 gives the maximum fault-potential distribution at each residential building or power distribution box of concern under different phase-to-ground fault positions occurred outside the buildings. Each radially distributed branch represents the measured positions, *i.e.*, the possible electric-shock positions. It is found that when a phase-to-ground fault occurs at the sub-main DB, there would be dangerous fault potential on the PE wire or its connected conductors in the main LV SB, sub-main DB itself, and the buildings with type A and type B PE methods. It is noted that the limit of a safe touch voltage has been investigated by related standard files and research [23–25]. The maximum effective value of the fault potential under the concerned fault conditions are always larger than 40V, exceeding the recommended lowest safe threshold of the human-body electric shock, i.e., 24V. Touch voltage exceeding that level could be dangerous. This is because of the high proportion of the grounding resistance at the sub-main DB in the line-fault point-earth-equivalent voltage source of the distribution transformer circuit, which determines a relatively high fault potential at the fault point and the equal-potential point via the earth, *i.e.*, the type A and type A PE protected buildings. For the case of phase-to-ground fault at the overhead line (called submain circuit I and II), the high ground potential has no path transferring to the PE wire wiring into the buildings and touched by human body, thus there is no abvious high fault potential exposure to other locations.

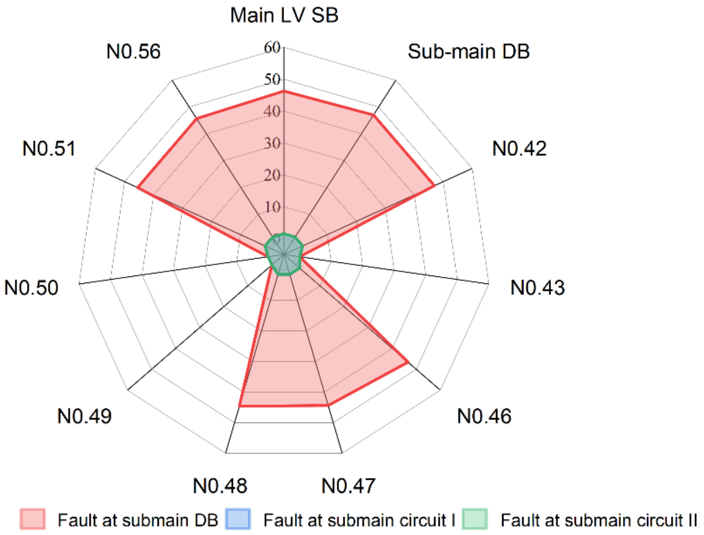

Fig.4-27 The maximum fault-potential distribution at the residential buildings or the concerned power components, under conditions of phase-to-ground fault occurred outside the buildings.

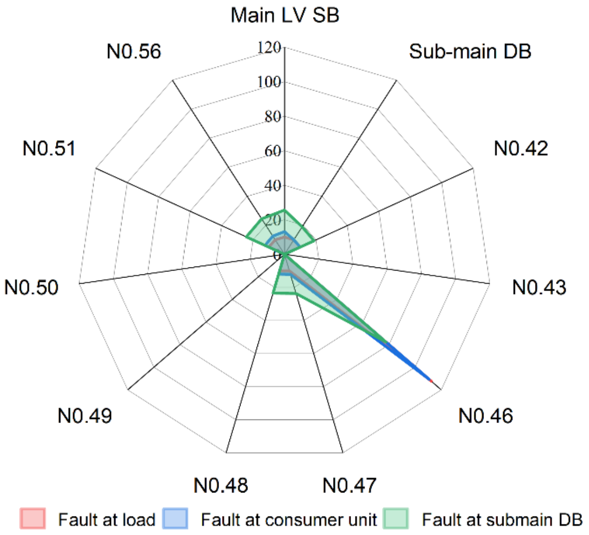

(a) Fault occurred in No.46 building

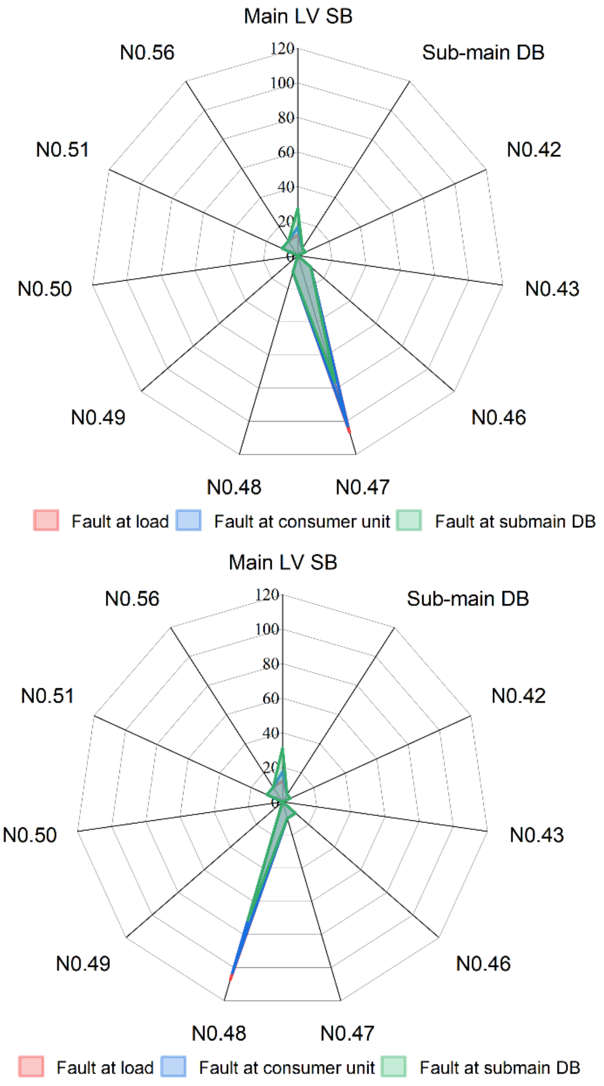

(b) Fault occurred in No.47 building (c) Fault occurred in No.48 building

Fig.4-28 The maximum fault-potential distribution at the residential buildings or the concerned power components, under different phase-to-ground fault occurred in type-A protected buildings.

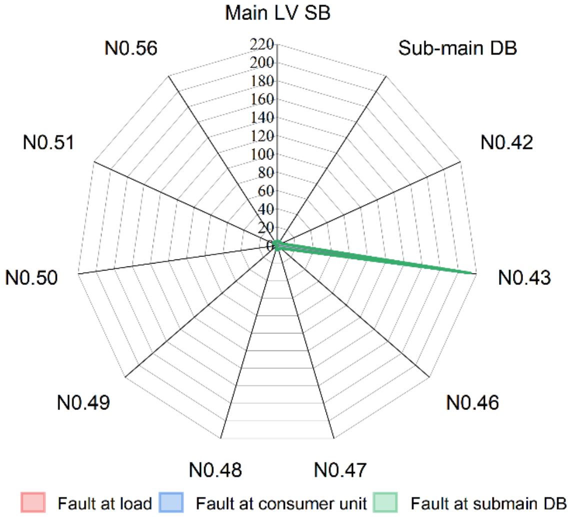

(a) Fault occurred in No.43 building

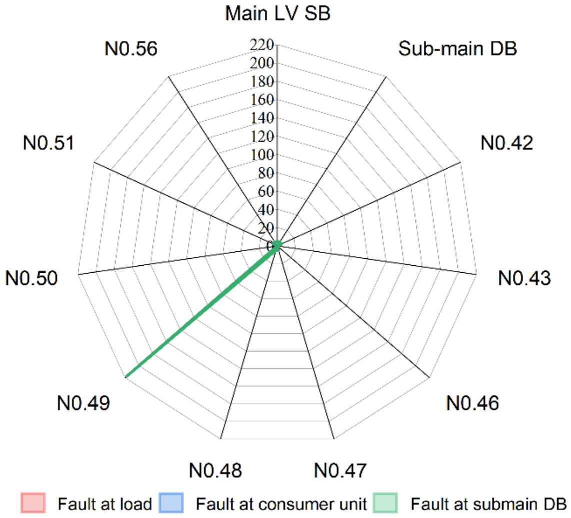

(b) Fault occurred in No.49 building

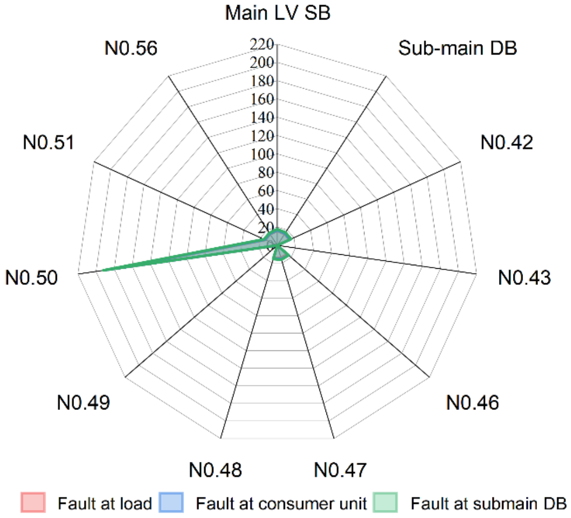

(c) Fault occurred in No.50 building

Fig.4-29 The maximum fault-potential distribution at the residential buildings or the concerned power components, under different phase-to-ground fault occurred in type-B protected buildings.

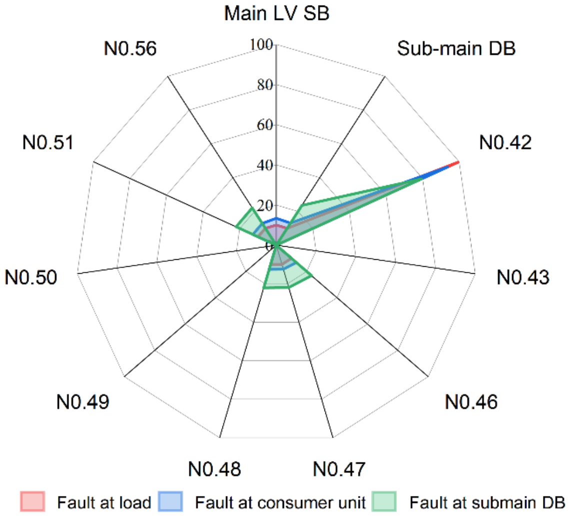

(a) Fault occurred in No.42 building

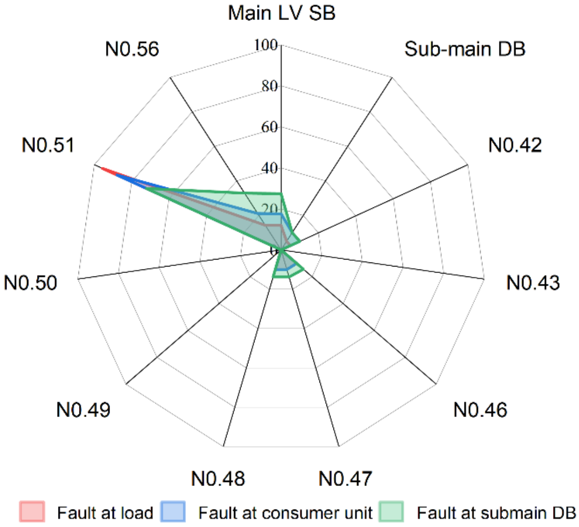

(b) Fault occurred in No.51 building

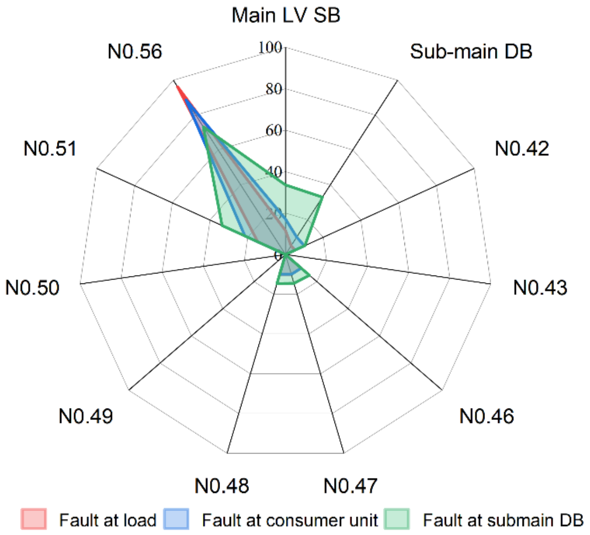

(c) Fault occurred in No.56 building

Fig.4-30 The maximum fault-potential distribution at the residential buildings or the concerned power components, under different phase-to-ground fault occurred in type-C protected buildings.

The fault-potential distribution in the case of phase-to-ground fault occurring in the residential buildings,have been shown in Fig.4-28 to Fig.4-30, respectively. The results with different colors in each sub-figure have distinguish different fault locations in the buildings. It is found that the fault potential distribution mainly depends on the PE protective methods in the case of a indoor phase-to-ground fault. Type-A protected buildings (No. 46, No. 47, No. 48) have a fault potential more than 100 V when the line fault occurs in themselves, while the main low-voltage (LV) switchboard (SB) would also have a potential over 24V in some cases, such as the fault at the final main DB.

Type-B protected buildings (No.43, No.49, No.50), as the results shown in Fig.4-28, have no separate PE wire indoors the buildings. Thus, when a ground fault occurs, there is a single fault circuit disconnected from other line systems and other buildings or main LV SB, and sub-main DB is difficult to be affected by the fault potential. Note that the fault potential in these buildings reaches close to 220V, as the results shown in Fig.4-28, because of a much larger proportion of the grounding resistance in the whole fault circuit.

Type-C protected buildings (No.42, No.51, No.56) have a fault potential close to 100 V when the line fault occurs in themselves. Since these buildings have a PE wire connected with the neutral wire (N wire) at the entrance of the buildings, the fault potential is more likely to be transferred to each other. Thus, the line-fault cases in one of the two buildings would more easily cause the dangerous electric shock case in the other one.

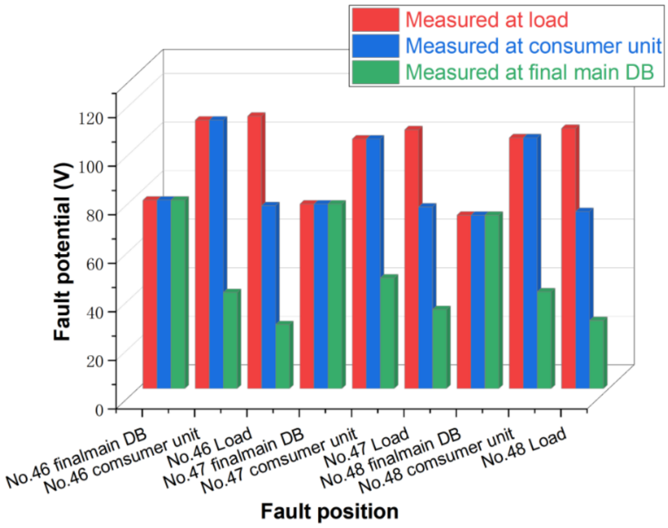

(a) Buildings with type A PE methods

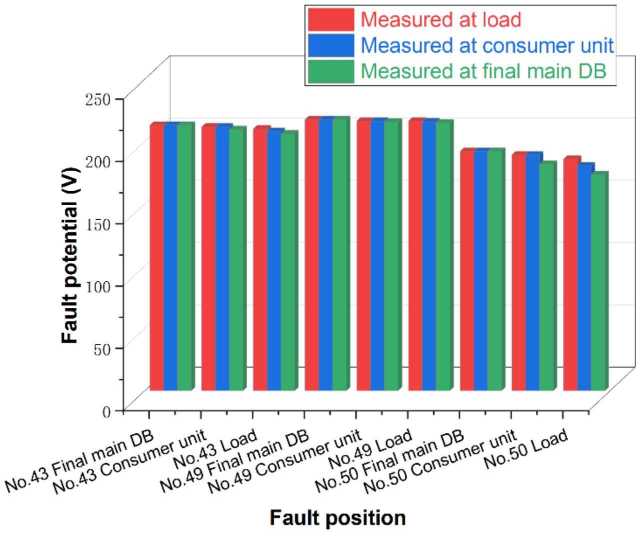

(b) Buildings with type B PE methods

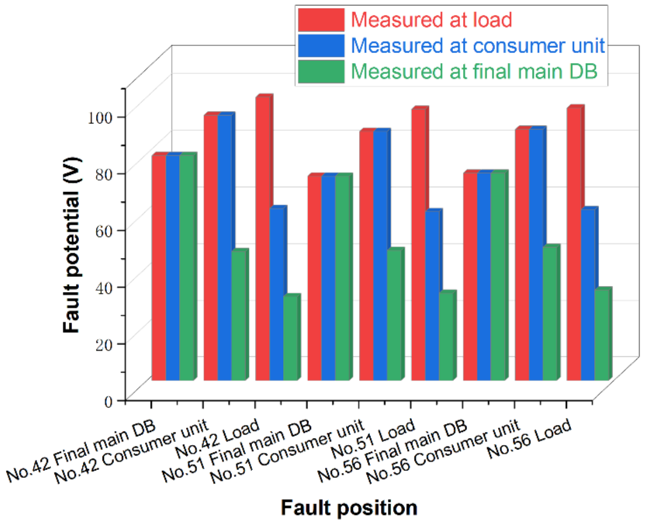

(c) Buildings with type c PE methods

Fig.4-31 The fault-potential distribution along the indoor PE wire under different phase-to-ground fault positions.

Overall, the buildings with the same PE method have similar characteristics of fault potential. That is, the overhead line topology of the LV distribution system outside the residential buildings has little effect on the fault potential distribution. Note that in Fig.4-30 only the maximum fault potential in a building is presented. In fact, if there is a grounding point for the N line at the building entrance no matter via a separate PE wire or not, *i.e.*, the type A and type C protected buildings, most of the fault cases would cause a fault-potential decrease along the wire in the buildings.

To investigate the characteristic of the fault-potential decrease along the wire in the buildings, Fig.4-31 presents the fault-potential distribution along the indoor PE wire, with conditions of indoor fault positions. The sub-figures respectively show the results with different PE methods. For type-A and type-B protected buildings, as the results shown in Fig.4-31 (a) and Fig.4-31(c), it could be found that when a line fault occurs at the consumer's load, there is obvious potential decrease along the indoor PE wire. When a line fault at the consumer unit appears, the consumer unit and the user's load have the same fault potential because of the open-circuit status of the PE wire between the two points, while the fault potential at the final main DB would significantly decrease because of the line-impedance voltage drop along the indoor PE line (or the N wire connected with PE wire). Note that the cases of the line fault occurring at the final main DB would cause the same potential in the indoor PE wire because of the open-circuit status between the load and final main DB. For the type-B protected buildings, as the results shown in Fig.4-31(b), since the indoor

N wire is disconnected with the PE wire at the entrance of the building, the voltage drop along the grounded PE wire is small due to the low fault current as well as the low line impedance, no matter where the indoor phase-to-ground fault occurs. Thus, there is only slight difference of the maximum amplitude among the three measurement points.

4.7.3 Fault-potential assessment under the conditions of phase-to-neutral line fault

In this part, the fault potential under the phase-to-neutral line fault conditions is assessed and analyzed. Similarly, all the possible fault locations as same as that of the analysis in Section IV are of concern for simulation.

Fig.4-32 shows the maximum fault-potential distribution at the residential buildings or the concerned power components, under conditions of phase-to-neutral line fault occurred outside the buildings. It is noted that the conditions of phase-to-neutral line fault at the sub-main DB causes the same fault-potential results as that of phase-to-ground fault, which have been shown as the red curve in both Fig.4-27 and Fig.4-32. It is because the N wire is connected with a PE wire at the main LV switchboard and the sub-main DB of the LV line system, i.e., the two faults actually have the same equivalent circuit. As for the faults occurs at the overhead lines (called sub-main circuit I and circuit II in this study), the fault potential could be transferred to some of the buildings due to the connection between the N wire and PE wire at the entrance of the buildings, e.g., NO.42, NO.46, NO.47, NO.48, NO.51, NO.56 building. In this case, the maximum fault potential could reach more than 40 V as shown in Fig.4-32.

Fig.4-33 shows the maximum fault-potential distribution at the residential buildings or the concerned power components, under conditions of phase-to-neutral line fault occurred in type-A protected buildings. It is found that compared with the phase-to-ground line faults at the same positions, the fault potential caused by the phase-to-neutral line fault is lower, while there are also a maximum exceed 80V, much higher than a human-body safe threshold of 24V. The fault potential distribution is highly similar to that of the phase-to-ground faults, compared with the results shown in Fig.4-28.

Fig.4-34 shows the maximum fault-potential distribution at the residential buildings or the concerned power components, under conditions of phase-to-neutral line fault occurred in type-B protected buildings. Since the type-B PE method has a separate PE wire disconnected with the indoor N wire, the phase-to-neutral line fault cannot cause fault potential on the PE wire in the building where the fault occurred. The fault potential would be transferred to nearby buildings, i.e., there is the wider fault-potential distribution than that of the phase-to-ground fault conditions, while the amplitude does not significantly exceed 24V.

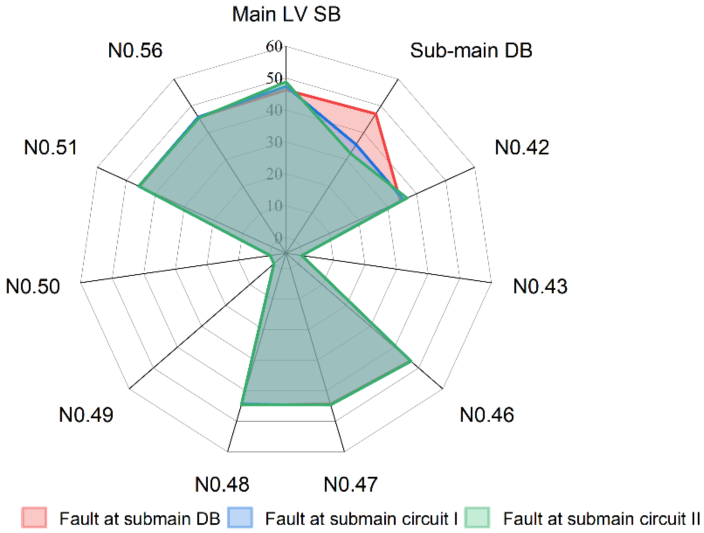

Fig.4-33 The maximum fault-potential distribution at the residential buildings or the concerned power components, under conditions of phase-to-neutral line fault occurred outside the buildings.

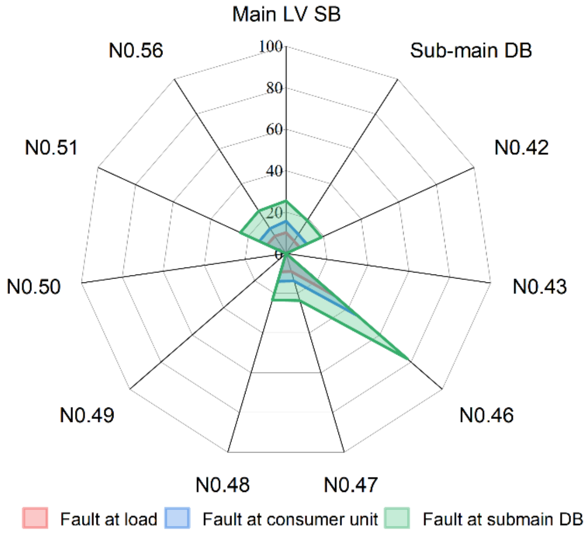

(a) Fault occurred in No.46 building

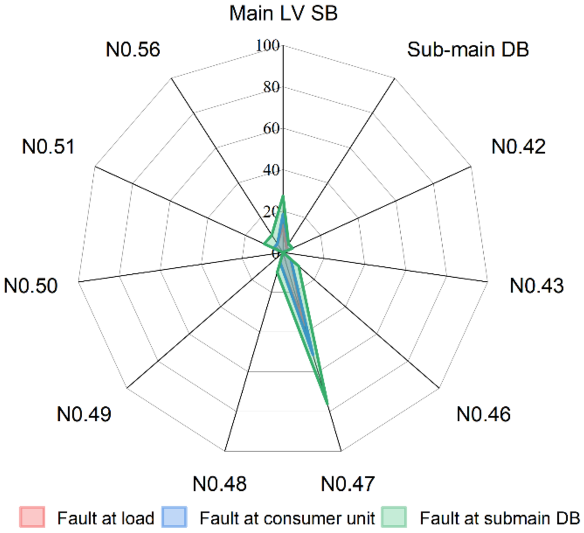

(b) Fault occurred in No.47 building

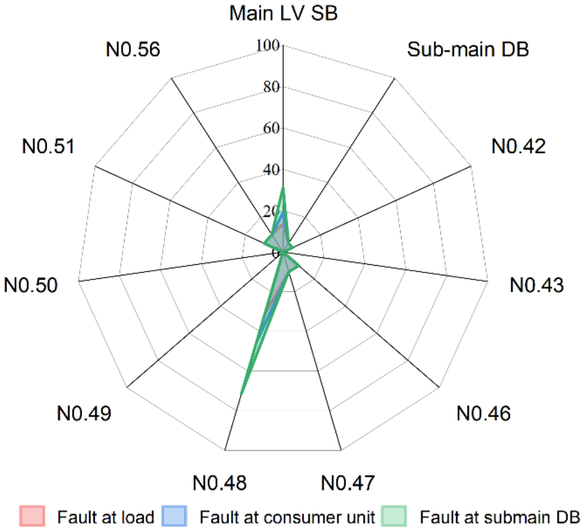

(c) Fault occurred in No.48 building

Fig.4-34 The maximum fault-potential distribution at the residential buildings or the concerned power components, under different phase-to-neutral line fault occurred in type-A protected buildings.

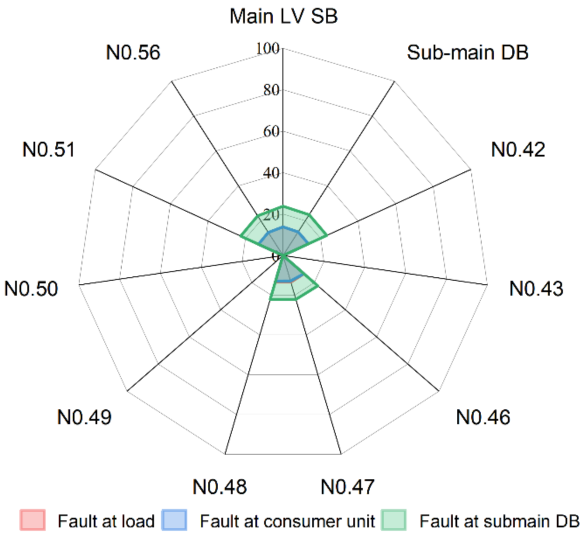

(a) Fault occurred in No.42 building

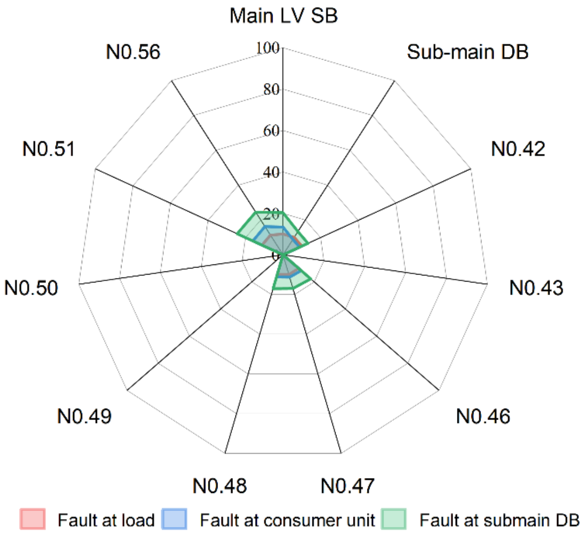

(b) Fault occurred in No.51 building

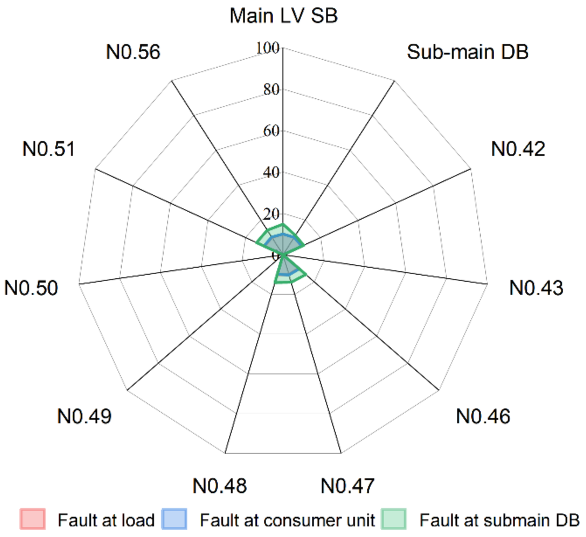

(c) Fault occurred in No.56 building

Fig.4-35 The maximum fault-potential distribution at the residential buildings or the concerned power components, under different phase-to-neutral line fault occurred in type-B protected buildings.

Note that for type-C protected buildings, the N wire is grounded and play a role as a PE wire indoor the buildings, the phase-to-neutral line faults have the same equivalent circuit as that of the phase-to-ground faults, which cause the same results as that of Fig.4-31. In this section, the corresponding results would not be repeatedly presented. It is also noted that for type-A and type-B protected buildings, the fault potential due to the phase-to-neutral line fault has a fixed value along the whole indoor PE wire, because of the open-circuit status of the PE wire when the line fault occurred. In this case, there is no need to show the indoor potential distribution separately like Fig.4-32.

Compared the calculated results in Section IV. A and B, it is noted that in most indoor phase-to-neutral line fault cases there would be a noticeably lower fault potential than that of the phase-to-ground cases at the same position with more than 30% reduction of the amplitude. Nevertheless, the amplitude of the fault potential at the fault positions would also be easily over the safe threshold 24V. As for the performance of three typical PE methods, it is concluded that Type-C PE method has the best protective performance, with the lowest phase-to-ground fault potential amplitude at the fault locations and the complete elimination of the phase-to-neutral line fault potential.

4.8 Section Conclusion

The present study investigated the fault potential of the equipment and human-body touch voltage in several typical line-fault conditions. Three protective grounding configurations of the LV distribution network adopted for the old residential communities were of concern. Both LV system components and grounding electrodes were simulated with the PEEC method. The potential distribution on the soil surface is evaluated by modeling the buried conductors. The equivalent circuit of electric shock scenarios that consider practical situations was considered in the simulation.

It has been observed that the phase-to-ground fault potential of equipment increases when the fault location is closer to the faulty equipment and decreases when it is closer to the circuit. High contact voltages are observed on indoor equipment when the phase-to-ground fault occurs indoors. Thus, the equipment in a building is likely exposed to the dangerous fault potential under the phase-to-ground line fault. As for line-to-neutral short circuit and neutral-line-open fault, the fault potential distribution mainly depends on the specific grounding configurations.

Bonding of non-exposed steelwork in the building foundation to the nearby grounding grid may not be recommended in the literature, but it can reduce the touch voltage effectively of concern in this paper. This method with the local eq. bonding method could give enhanced protection against electricity. Under L-N faults, the TX(M)-C-S configuration leads to more dangerous touch voltage than other configurations, while most of the hazardous cases could be addressed by eq. bonding provided in the buildings. Under the neutral-line open fault, both TT and TT(M)-C-S configurations usually do not lead to dangerous touch voltage, even if eq. bonding is not provided. Among three grounding configurations, the one with multiple grounding points of the neutral wires up to the entrance of a building leads to the least dangerous touch voltage cases.

The electric shock risk is analyzed for the different ground systems. The electric shock rise may be caused by step voltage or touch voltage. It is found that the step voltage is decided by the ground potential distribution around a grounding electrode/grid. The complicated grounding grid, like a fork-type ground grid, may have a low step voltage than a single electrode. Moreover, the touch voltage under phase-to-earth or phase-to-neutral fault condition is analyzed. Although the electric shock risk area is the same for a TT system or TN-C system, the TT system generally has a higher touch voltage magnitude than the TN-C system.

5 Conclusion

This thesis has undertaken an in-depth exploration of grounding systems in power distribution networks, specifically addressing both the effects of lightning transients and fault conditions within low-voltage (LV) networks. Given the increasing reliance on sensitive electronic systems and the prevalence of outdated electrical infrastructure, understanding and mitigating the risks associated with grounding systems have become essential for ensuring system reliability and public safety. By developing and integrating advanced models, this research has provided a new perspective on grounding configurations and their role in protecting against electromagnetic disturbances and fault-induced hazards.

The thesis first focused on lightning transients by introducing a Nonlinear Charge Simulation Method (NCSM) to model the charge dynamics in downward negative lightning leaders accurately. This method allowed for a more precise representation of the interaction between lightning channels and grounded structures, overcoming limitations present in traditional models. Additionally, an extended Transmission Line (TL) model was developed to simulate the electromagnetic effects of lightning strikes on tall structures, such as wind turbines, considering the critical role of corona effects and nonlinear channel characteristics. These contributions offer insights into improving protective measures against lightning in critical infrastructures, providing a framework for enhanced lightning resilience.

In the context of fault conditions, this research addressed the safety risks associated with touch voltage and fault potential in aging residential LV networks, where outdated grounding configurations pose significant risks. Using the Partial Element Equivalent Circuit (PEEC) method, the study evaluated different grounding configurations (TT, TT(M)-C-S, TX(M)-C-S) under fault conditions, providing a systematic analysis of their effectiveness in reducing touch voltage and mitigating electrocution risks. The simulation results highlighted the advantages of distributed grounding points and modern grounding designs, which offer improved fault safety and touch voltage protection, especially where retrofitting modern protective devices is not feasible.

Through comprehensive simulations and validation against experimental data, this thesis has demonstrated the limitations of traditional grounding models and the importance of adopting advanced simulation techniques for accurate risk assessment and safety enhancement in urban electrical systems. The proposed methods provide a foundation for future research in grounding system optimization and electromagnetic protection. Ultimately, the findings and recommendations of this study aim to guide the development of safer, more resilient power distribution networks, particularly in urban areas with aging infrastructure, ensuring the safety of both critical equipment and residents.

6 Future work

This research has provided valuable insights into grounding system modeling and assessment under lightning transients and fault conditions. However, several areas warrant further investigation to advance the understanding and application of grounding systems in power distribution networks.

Firstly, while this thesis has developed a Nonlinear Charge Simulation Method (NCSM) for modeling lightning charge dynamics and a Transmission Line (TL) model for lightning interactions with tall structures, there remains a need to extend these models to incorporate more complex environmental factors. Future studies could explore the effects of varying atmospheric conditions, such as humidity and temperature, on lightning propagation and charge distribution. Additionally, developing models that account for the influence of multiple structures in close proximity—such as densely packed urban environments—could enhance the applicability of these simulations for real-world urban planning and infrastructure protection.

Secondly, the fault condition analysis in low-voltage (LV) distribution networks could be expanded by investigating a wider range of grounding configurations, including hybrid or adaptive grounding systems. As power systems evolve to incorporate renewable energy sources and distributed generation, grounding systems in urban areas will need to accommodate these changes. Future research could assess the effectiveness of advanced grounding configurations that integrate adaptive or dynamic grounding elements, such as variable resistance grounding, to enhance protection against varying fault scenarios in modernized power networks.

The Partial Element Equivalent Circuit (PEEC) method, which was employed in this research for fault potential and touch voltage analysis, has demonstrated significant effectiveness. However, extending the PEEC method to model transient behavior over broader frequency ranges could offer further insights into the grounding system's response to various types of transient disturbances. Future work could also incorporate real-time data from fault monitoring systems to validate the PEEC simulations, improving model accuracy and real-world relevance. This approach would be particularly beneficial in adapting grounding systems to meet the evolving demands of smart grids and interconnected urban infrastructures.

Finally, given the critical importance of safety in aging residential communities, additional studies should be conducted on practical, cost-effective solutions for upgrading grounding systems in existing buildings. This could include experimental evaluations of grounding retrofit techniques or the development of guidelines for integrating residual current devices (RCDs) and other protective devices in areas with limited retrofit capacity. Pilot projects in real urban environments could provide valuable data for validating simulation results and refining grounding protection strategies. Collaborative efforts with municipal authorities and urban planners may facilitate the implementation of these solutions, ensuring that they are both technically feasible and practically adoptable in communities facing infrastructure constraints.

In conclusion, while this thesis has addressed foundational challenges in grounding system modeling and protection, further exploration in these areas will be essential for advancing grounding technologies to meet the demands of modern, resilient, and sustainable power distribution networks.

Appendix

Lightning-induced electromagnetic fields can be calculated by Uman's formula [36]. By using the image theory, a straight lightning channel above a perfect ground can be modeled as a vertical dipole, as shown in Fig.A. For the current segment at height *z* at time *t*, the electric field at a point with a horizontal distance D from the channel can be calculated with the following equation:

$$
d\boldsymbol{E}^{i}\left(r,t\right)=\frac{1}{4\pi\varepsilon_{0}}\left(\int_{0}^{t}\frac{I(z',\tau')\left[2\cos\theta\,\hat{r}+\sin\theta\,\hat{\theta}\right]}{R^{3}}d\tau\right.
$$

$$
\left.+\frac{I(z',t')\left[2\cos\theta\,\hat{r}+\sin\theta\,\hat{\theta}\right]}{cR^{2}}+\frac{\partial I(z',t')}{c^{2}R\,\partial t'}\sin\theta\,\hat{\theta}\right)dz'
$$

where $t'=t-\frac{R}{c}$, $\tau'=\tau-\frac{R}{c}$ and $R=\sqrt{D^{2}+\left(z-z'\right)^{2}}$.

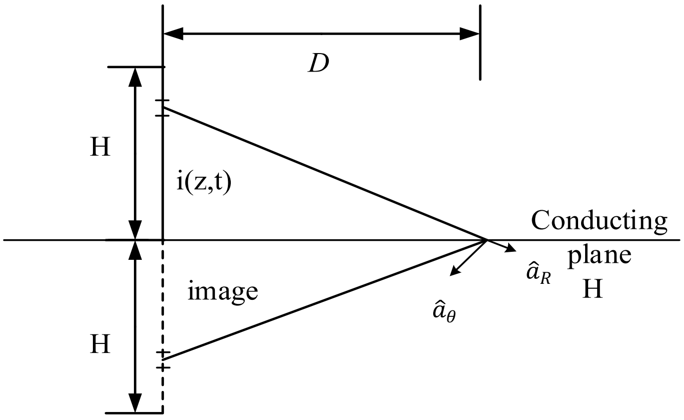

Fig. A straight vertical lightning channel of height H above a perfectly conducting ground plane.

Reference

[1] P. Clayton, Analysis of multiconductor transmission lines, Hoboken, N.J., Wiley-Interscience, IEEE Pres 2008

[2] F. Rachidi, C.A. Nucci, M. Ianoz and C. Mazzetti, “Influence of a lossy ground on lightning-induced voltages on overhead lines,” IEEE Tran. on EMC, Vol. 38, No. 3, pp.250-264, August 1996

[3] C. D. Taylor, R. S. Satterwhite and C.W. Harrison, “The response of a terminated two-wire transmission line excited by a nonuniform electromagnetic field,” IEEE Trans. on AP, vol. 13, pp. 987-989, 1965

[4] A. K. Agrawal, H. J. Price, and S. H. Gurbaxani, “Transient response of multiconductor transmission lines excited by a nonuniform electromagnetic field,” IEEE Trans on EMC, vol. 22, no. 2, pp. 119-129, 1980

[5] P. Chowdhuri, “Lightning-induced voltages on multiconductor overhead lines,” IEEE Trans. on PWRD, vol. 5 no. 2, pp. 658~667, 1990

[6] C. A. Nucci, M. Ianoz, and C Mazzetti, “Comparison of two coupling models for lightning-induced overvoltage calculations,” IEEE Trans. on PWRD, vol. 10 no. 1, pp. 330~339, 1995

[7] V. Cooray, “Calculating lightning-induced overvoltages in power lines: A comparison of two coupling models,” IEEE Trans on EMC, vol. 26 no 3, pp. 79~182, 1994

[8] S. Tkatchenko, F. Rachidi and M. Ianoz, "Electromagnetic field coupling to a line of finite length: Theory and fast iterative solutions in frequency and time domains," IEEE Trans on EMC, vol. 37 no. 4, pp. 509-518,1995

[9] A. E. Ruehli, "Equivalent circuit models for three-dimensional multiconductor systems," IEEE Trans. Microw. Theory Tech., vol. MTT-22, no. 3, pp. 216–221, Mar. 1974

[10] A. Ruehli, Jan Garrett, and Clayton Paul. "Circuit models for 3D structures with incident fields," Procs. of 1993 IEEE International Symposium on EMC, Dallas, TX, USA, Aug. 1993, pp. 28-32

[11] G. Antonini, S. Cristina and A. Orlandi, “PEEC modeling of lightning protection systems and coupling to coaxial cables,” IEEE, Trans. on EMC, vol. 40 no. 4, Nov, pp.481, 1998

[12] A. Orlandi and F. Schietroma F, “Attenuation by lightning protection

system of induced voltages due to direct strikes to a building," IEEE Trans. on EMC, vol. 8 no. 1, pp. 43-50, 1996

[13] P. Yutthagowith, A. Ametani, N. Nagaoka and Y. Baba, "Application of the partial element equivalent circuit method to analysis of transient potential rises in grounding systems," IEEE Trans. on EMC, vol. 53 no. 3, pp726-736, 2011

[14] P. Yutthagowith, A. Ametani, N. Nagaoka, Y. Baba, "Application of the partial element equivalent circuit method to analysis of transient potential rises in grounding systems." IEEE Trans on EMC vol. 53 no.3, pp. 726-736, 2011

[15] Q. B. Zhou and Y. Du, "Using EMTP for evaluation of surge current distribution in metallic gridlike structures," IEEE Trans. on IA, vol. 41 no. 4, pp1113-1117, 2005

[16] H. Chen, Y. Du and M. Chen, "Lightning transient analysis of radio base stations." IEEE Trans on PWRD, vol. 33, no. 5, pp. 2187-2197, 2018

[17] Hongcai Chen and Ya-ping Du, "Model of ferromagnetic steels for lightning transient analysis." IET Science, Measurement & Technology, vol. 12 no. 3, pp. 301-307, 2018

[18] Y. Du, SM Chen and J. Burnett, "Experimental and numerical evaluation of surge current distribution in buildings during a direct lightning stroke," HKIE Transactions, vol. 8 no. 1, pp.1-6, April 2001

[19] S.V. Kochetov, M. Leone and G. Wollenberg, "PEEC formulation based on dyadic Green's functions for layered media in the time and frequency domains," IEEE Trans. on EMC, vol. 50, no. 4, pp. 953-963, Feb. 2008

[20] C. D. Taylor, R. S. Sattenvhite and C.W. Harrison, "The response of a terminated two-wire transmission line excited by a nonuniform electromagnetic field," IEEE Trans. on AP, vol. 13, 1965, pp. 987-989

[21] A. K. Agrawal, H. J. Price, and S. H. Gurbaxani, "Transient response of multiconductor transmission lines excited by a nonuniform electromagnetic field," IEEE Trans on EMC, vol. 22, 1980, pp. 119~129

[22] P. Chowdhuri and E.T. B. Gross, "Voltage surges induced on overhead lines by lightning strokes," Proc. of IEE, vol. 114 no. 12, 1967, pp. 1899~1907

[23] P. Chowdhuri, "Lightning induced voltages on multiconductor overhead lines," IEEE Trans. on PWRD, vol. 5 no. 2, 1990, pp. 658~667.

[24] M.A. Uman, D.K. McLain and E. P. Krider, "The electromagnetic radiation

from a finite antenna." American Journal of Physics, vol. 43 no. 1, pp. 33-38.

[25] C. A. Nucci, M. Ianoz, and C Mazzetti, “Comparison of two coupling models for lightning-induced overvoltage calculations,” IEEE Trans. on PWRD, vol. 10 no. 1, 1995, pp. 330~339.

[26] V. Cooray, “Calculating lightning-induced overvoltages in power lines: A comparison of two coupling models,” IEEE Trans on EMC, vol. 26 no 3, 1994, pp. 79~182

[27] S. Tkatchenko, F. Rachidi and M. Ianoz, "Electromagnetic field coupling to a line of finite length: Theory and fast iterative solutions in frequency and time domains," IEEE Trans on EMC, vol. 37 no. 4,1995, pp. 509-518

[28] Y P. Yutthagowith, A. Ametani, F. Rachidi, N. Nagaoka & Y. Baba, "Application of a partial element equivalent circuit method to lightning surge analyses." EPSR, vol. 94, 2013, pp. 30-37.

[29] Du, Xinghua Wang and Mingli Chen, “Circuit parameters of vertical wires above a lossy ground in PEEC models”, IEEE Trans. on EMC, vol. 54, no. 4, 2012, pp.871-879

[30] G. Ala and M.L.Di Silvestre. "A simulation model for electromagnetic transients in lightning protection systems." IEEE Trans on EMC, vol. 44 no. 4, 2002, pp. 539-554.

[31] G. Antonini, S. Cristina, and A. Orlandi. "PEEC modeling of lightning protection systems and coupling to coaxial cables." IEEE Trans on EMC vol. 40 no. 4, 1998, pp. 481-491.

[32] Q. B. Zhou and Y. Du, “Using EMTP for evaluation of surge current distribution in metallic gridlike structures,” IEEE Trans. Ind. Appl., vol. 41, no. 4, 2005, pp. 1113–1117

[33] H. Chen, Y. Du and M. Chen, "Lightning transient analysis of radio base stations." IEEE Trans on PWRD, Vol. 33, no. 5, 2018, pp. 2187-2197

[34] Hongcai Chen and Ya-ping Du, “Model of Ferromagnetic steels for lightning transient analysis.” IET Science, Measurement & Technology, Vol. 12 no. 3, 2018, pp. 301-307

[35] S. Tkatchenko, N. Theethayi, Y. Baba, F. Rachii and R. Thottappillil, “On the choice between transmission line and full-wave Maxwell’s equation for transient analysis of buried wires,” IEEE Trans. EMC, vol. 50, no. 2, 2008, pp. 347–357

[36] K. Tanabe, A. Asakawa, M. Sakae, M. Wada, and H. Sugimoto, “Verifying the computational method of transient performance with respect to grounding systems based on the FD–TD method,” IEEJ Trans. Power Energy, vol. 123, no. 3, 2003, pp. 358–367 (in Japanese).

[37] Y. Baba, N. Nagaoka, and A. Ametani, “Modeling of thin wires in a lossy medium for FDTD simulation,” IEEE Trans. Electromagn. Compat., vol. 47, no. 1, 2005, pp. 54–60

[38] M. Akbari, K. Sheshyekani, A. Pirayesh, F. Rachidi, M. Paolone, A. Borghetti, and C.A. Nucci, “Evaluation of lightning electromagnetic fields and their induced voltages on overhead lines considering the frequency dependence of soil electrical parameters,” IEEE Trans on EMC, vol. 55 no. 6, 2013, pp. 1210-1219

[39] A. Orlandi, “Lightning induced transient voltages in presence of complex structures and nonlinear loads,” IEEE Trans. on EMC, vol. 38, no 2, 1996. pp. 150-155.

[40] Binghao Li, Yaping Du and Mingli Chen, “An FDTD thin wire model for lossy wire structures with non-circular cross section,” IEEE Trans. on PWRD, DOI 10.1109/TPWRD.2018.2835819.

[41] K. Sheshyekani and M. Akbari, “Evaluation of lightning-induced voltages on multiconductor overhead lines located above a lossy dispersive ground,” IEEE Trans. on EMC, vol. 29, no. 2, 2014, pp. 409.

[42] L. Hasselgren and J. Luomi, “Geometrical aspects of magnetic shielding at extremely low frequencies,” IEEE Trans. on EMC, vol. 37, no. 3, Aug. 1995, pp. 409–420.

[43] Y. Du and J. Burnett, “ELF shielding performance of metallic enclosure for heavy-current conductors,” IEE Proc. – Gener. Transm. Distrib. vol. 146, no. 3, May 1999, pp. 223-228.

[44] Baba Y, Rakov V A. “On the transmission line model for lightning return stroke representation,” Geophysical Research Letters, vol. 30, no. 24, 2003.

[45] Li B , Du Y P , Chen M . “An FDTD thin wire model for lossy wire structures with non-circular cross section,” IEEE Transactions on Power Delivery, 2018, pp.1-1.

[46] Baba Y , Rakov V A . “On the mechanism of attenuation of current waves propagating along a vertical perfectly conducting wire above ground: application to lightning,” IEEE Transactions on Electromagnetic

Compatibility, vol. 47, no. 3, 2005, pp.521-532.

[47] Baba Y , Rakov V A . “On the interpretation of ground reflections observed in small-scale experiments Simulating lightning strikes to towers,” IEEE Transactions on Electromagnetic Compatibility, vol. 47, no. 3, 2005, pp.533-542.

[48] Baba, Y. and Rakov, V. “Voltages Induced on an Overhead Wire by Lightning Strikes to a Nearby Tall Grounded Object,” IEEE Transactions on Electromagnetic Compatibility, vol. 48, no. 1, 2006， pp.212-224.

[49] Nagaoka, N., Morita, H., Baba, Y. and Ametani, A. “Numerical Simulations of Lightning Surge Responses in a Seismic Isolated Building by FDTD and EMTP,” IEEJ Transactions on Power and Energy, vol. 128, no. 2, 2008, pp.473-478.

[50] Nguyen T T , Holt R . “Lightning protection of transmission lines: optimal shielding design procedure,” IEE Proceedings-Generation, Transmission and Distribution, vol. 150, no. 6, 2003, pp.659-0.

[51] Banjanin, M., Savić, M. and Stojković, Z. “Lightning protection of overhead transmission lines using external ground wires,” Electric Power Systems Research, vol. 127, 2015, pp.206-212.

[52] Pernet, S., Ferrieres, X. and Cohen, G. “High spatial order finite element method to solve Maxwell's equations in time domain,” IEEE Transactions on Antennas and Propagation, vol. 53, no. 9, 2005, pp.2889-2899.

[53] Abu Bakar, A., Zainal Abidin, A., Illias, H., Mokhlis, H., Abd Halim, S., Nor Hassan, N. And Tan, C. “Determination of the striking distance of a lightning rod using finite element analysis,” TURKISH JOURNAL OF ELECTRICAL ENGINEERING & COMPUTER SCIENCES, vol. 24, 2016, pp.4083-4097.

[54] Denno, K. “Computation of electromagnetic lightning response using moments method. IEEE Transactions on Magnetics,”, vol. 20, no. 5, 1984, pp.1953-1955.

[55] Berberovic, S., Haznadar, Z. and Stih, Z. “Method of moments in analysis of grounding systems,” Engineering Analysis with Boundary Elements, vol. 27, no. 4, 2003, pp.351-360.

[56] Ruehli A E. “An Integral Equation Equivalent Circuit Solution to a Large Class of Interconnect Systems,” Ph. D Thesis. University of Vermont, 1972.

[57] Ruehli A E and Brennan P A. “Efficient Capacitance Calculations for

Three-dimensional Multiconductor Systems," IEEE Trans. on Microwave Theory And Techniques, vol. 21, no. 2, 1973, pp.76-82

[58] Ruehli, A. "Equivalent Circuit Models for Three-Dimensional Multiconductor Systems," IEEE Transactions on Microwave Theory and Techniques, vol. 22, no. 3, 1974, pp.216-221.

[59] Wolff PK and Ruehli A E. "Inductance Computations for Complex Three Dimensional Geometries," In Proc. of the IEEE Int. Symp. on Circuits and Systems, 1981, pp. 16-19.

[60] Heeb H and Ruehli A E. "Approximate Time-domain Models of Three-dimensional Interconnects," In Proc. of the IEEE Int. Conf. on Computer Design, 1990, pp. 201-205.

[61] Ruehli AE and Heeb H. "Circuit Models for Three-dimensional Geometries Including Dielectrics," IEEE MTT-40(7): 1507-1516, July 1992.

[62] Garrett JE, Ruehli A E. "PEEC-EFIE for Modeling 3D Geometries with Lossy Inhomogeneous Dielectrics and Incident Fields," IBM Research Report RC 19245 (# 83733). IBM TJ Watson Research Center, Yorktown Heights, October 1993.

[63] Ruehli AE, Garrett J, Paul C R. "Circuit Models for 3D Structures with Incident Fields," In Proc. of The IEEE Int. Symp. on Electromagnetic Compatibility, Dallas, Tx, August 1993, pp. 28-31.

[64] Jerse T A. "A Hybrid Technique for Efficiently Estimating Common-mode Currents Transmission-Line Structures," Ph.D Dissertation, The University of Kentucky, 1994.

[65] A. E. Ruehli, J. Garrett, C. R. Paul. "Circuit models for 3d structures with incident fields," In Proc. of the IEEE Int. Symp. onElectromagnetic Compatibility, pages 28–31, Dallas, Tx, August 1993.

[66] Ruehli A, Antonini G, Jiang L. "Circuit Analysis for PEEC Methods," Circuit Oriented Electromagnetic Modeling Using the Peec Techniques, 2017.

[67] Caligaris C , Delfino F , Procopio R . "Cooray–Rubinstein Formula for the Evaluation of Lightning Radial Electric Fields: Derivation and Implementation in the Time Domain," IEEE Transactions on Electromagnetic Compatibility, vol.50, no. 1, 2008, pp. 194-197.

[68] Ruehli, A. E., G. Antonini, and J. J. Li. "Skin-Effect Loss Models for Time- and Frequency-Domain PEEC Solver." Proceedings of the IEEE vol. 101,

no. 2, 2013, pp.451-472.

[69] A. E. Ruehli, “Inductance calculations in a complex integrated circuit environment”, IBM Journal of Research and Development, vol. 16, no. 5, Sep. 1972, pp. 470481.

[70] A. E. Ruehli, C. Paul, and J. Garrett, “Inductance calculations using partial inductances and macromodels”, in Proc. of the Int. Symposium on EMC, Atlanta, GA, USA, 1995.

[71] S. Mei and Y. I. Ismail, “Modeling Skin and Proximity Effects with Reduced Realizable RL Circuits”, IEEE Trans. on VLSI Systems, vol. 12, no.4, April 2004.

[72] Enohnyaket M , Ekman J . “PEEC Models for Air-core Reactors Modeling Skin and Proximity Effects,” IEEE Power Electronics Specialists Conference. IEEE, 2007.

[73] Hongcai, Chen , and D. Yaping . “Proximity effect modelling for cables of finite length using the hybrid partial element equivalent circuit and artificial neural network method.” IET Generation, Transmission & Distribution vol. 12, no.16, 2018, pp.3876-3882.

[74] Chen, Hongcai , Y. Du , and M. Chen . “Lightning Transient Analysis of Radio Base Stations.” IEEE Transactions on Power Delivery, 2018, pp.1-1.

[75] Application of a partial element equivalent circuit method to lightning surge analyses

[76] Yutthagowith, P. , et al. “Lightning-Induced Voltage Over Lossy Ground by a Hybrid Electromagnetic Circuit Model Method With Cooray–Rubinstein Formula.” IEEE Transactions on Electromagnetic Compatibility vol. 51, no. 4, 2009, pp. 975-985.

[77] Yutthagowith, P , et al. “Application of the Partial Element Equivalent Circuit Method to Analysis of Transient Potential Rises in Grounding Systems.” IEEE Transactions on Electromagnetic Compatibility vol. 53, no. 3, 2011, pp.726-736.

[78] Caligaris C , Delfino F , Procopio R . “Cooray–Rubinstein Formula for the Evaluation of Lightning Radial Electric Fields: Derivation and Implementation in the Time Domain,” IEEE Transactions on Electromagnetic Compatibility, vol.50, no. 1, 2008, pp. 194-197.

[79] X Zhang, “Computation of Lightning Transients in Large Scale Multi-conductor Systems,” IEEE Access, 2018

[80] A. Deri, G. Tevan, A. Semlyen, and A. Castanheria, “The complex ground return plane: A simplified model for homogeneous and multilayer earth return,” IEEE Trans. Power App. Syst., vol. 100, no. 8, Aug. 1981, pp. 3686–3693.

[81] A. Ametani, Y. Kasai, J. Sawada, A. Mochizuki, and T. Yamada, “Frequency-dependent impedance of vertical conductors and a multiconductor tower model,” IEE Proc.—Gener. Transm. Distrib., vol. 141, no. 4, Jul. 1994, pp. 399–345.

[82] K. Okumura. “Surge impedance of transmission line tower: C.A. Jordan’s formula,” [Online]. Available: http://www.ensc.sfu.ca/~ljilja/cnl/guests/okumura.html, 2012.

[83] G. Antonini, S. Cristina, and A. Orlandi, “PEEC modeling of lightning protection systems and coupling to coaxial cables,” IEEE Trans. Electromagn. Compat., vol. 40, no. 4, Nov. 1998, pp. 481–491.

[84] K. A. Michalski, “On the scalar potential of a point charge associated with a time-harmonic dipole in a layered medium,” IEEE Trans. Antennas Propag., vol. 35, no. 11, Nov. 1987, pp. 1299–1301.

[85] Du, Y. , X. Wang , and M. Chen . “Circuit Parameters of Vertical Wires Above a Lossy Ground in PEEC Models,” IEEE Transactions on Electromagnetic Compatibility, vol. 54, no. 4, 2012, pp.871-879.

[86] Yutthagowith, P. “Application of a time-domain partial element equivalent circuit method to lightning surge analysis,” International Conference on Electrical Engineering/electronics Computer Telecommunications & Information Technology IEEE, 2010.

[87] J. Ekman. “Full-Wave Time Domain PEEC Formulation Using a Modified Nodal Analysis Approach,” Technische Universiteit Eindhoven, EMC Europe 2004.

[88] Y. Zhang, Y. Du. “Lightning protection design of solar photovoltaic systems: Methodology and guidelines,” Electric Power Systems Research, June 2019.

[89] Yutthagowith, Peerawut , et al. “Application of a partial element equivalent circuit method to lightning surge analyses,” Electric Power Systems Research 94.none, 2013, pp. 30---37.

[90] H. Chen, Y. Zhang, Y. Du, “Lightning Transient Analysis of Telecommunication System With a Tubular Tower,” IEEE Access, Oct. 2018.

[91] X. Liu, P. Wang, G. Liang, “Time Domain Full Wave PEEC Circuit Model for Buildings Lightning Protection System”, 2016 Asia-Pacific International Symposium on Electromagnetic Compatibility (APEMC), May 2016.

[92] H. Chen, Y. Du, and M. Chen, “Lightning transient analysis of radio base stations,” IEEE Trans. Power Del., vol. 33, no. 4, Oct. 2018, pp. 2187–2197, Oct. 2018.

[93] J. Park, J. Lee, B. Seol, and J. Kim, “Fast and accurate calculation of system-level ESD noise coupling to a signal trace by PEEC model decomposition,” IEEE Trans. Microw. Theory Techn., vol. 65, no. 1, Jan. 2017, pp. 50–61, Jan. 2017.

[94] S. Thamm, S. V. Kochetov, G. Wollenberg, and M. Leone, “Alternative PEEC modeling with partial reluctances and capacitances for power electronics applications,” in Proc. 2007 7th Int. Symp. Electromagnetic Compatibility and Electromagnetic Ecology, Saint Petersburg, Russia, 2007, pp. 56–59.

[95] N. Xia, M. Tian, Y. Fu, Q. Zhou, and J. Guo, “A hybrid meshing technique for ferromagnetic structure based on PEEC method,” IEEE Trans. Magn., vol. 51, no. 11, Nov. 2015, pp. 1–4.

[96] Yutthagowith, P, “Application of the Partial Element Equivalent Circuit Method to Analysis of Transient Potential Rises in Grounding Systems,” IEEE Transactions on Electromagnetic Compatibility, vol. 53, no. 3, 2011, pp.726-736.

[97] Ala, G, M. L. Di Silvestre, “A simulation model for electromagnetic transients in lightning protection systems,” IEEE Transactions on Electromagnetic Compatibility, vol. 44, no. 4, 2002, pp.539-554.

[98] K. A. Michalski and D. Zhang, “Electromagnetic scattering and radiation by surfaces of arbitrary shape in layered media, part I: theory,” IEEE Trans. on AP, vol. 38, no. 3, 1990, pp. 335-344

[99] B. Gustavsen, "Fast passivity enforcement for pole-residue models by perturbation of residue matrix eigenvalues," IEEE Trans. on PWRD, vol. 23, 2008, pp. 2278-2285.

[100] B. Gustavsen and A. Semlyen, "Rational approximation of frequency responses by vector fitting," IEEE Trans. PWRD., vol. 14, no. 3, 1999, pp. 1052–1061

[101] R. G. Niciforovic, A. G. Polimeridis, “Fast Computation of Sommerfeld

Integral Tails via Direct Integration Based on Double Exponent," IEEE Transactions on Antennas and Propagation, Dec. 2010

[102] G.J. Burke et al., "Numerical Electromagnetic Code (NEC)," Technical document 116, Naval Ocean Systems Center, San Diego, 1980.

[103] K. A. Michalski and D. Zhang, "Electromagnetic scattering and radiation by surfaces of arbitrary shape in layered media, part I: theory," IEEE Trans. on AP, vol. 38 no. 3, 1990, pp. 335-344

[104] L. Grcev and F. Dawalibi, "An electromagnetic model for transients in grounding systems," IEEE Trans. Power Del., vol. 5, no. 4, Oct. 1990, pp. 1773–1779.

[105] Hongcai Chen and Yaping Du, "Lightning grounding grid model considering both the frequency-dependent behavior and ionization phenomenon," IEEE Trans on EMC, vol. 61, no. 1, Feb. 2019, pp.157–165

[106] Y. Rahmat-Samii, R. Mittra and P. Parhami, "Evaluation of Sommerfeld integrals for lossy half-space problems," Electromagnetics, vol. 1 pt. 1, 1981, pp.1-28

[107] Clayton R. Paul, Inductance: Loop and Partial, Hoboken, N.J., John Wiley & Sons, 2010

[108] F. W. Grover, Inductance Calculations: working formulas and tables, Research Triangle Park, N.C., Instrument Society of America, 1973

[109] Y. Du and Binghao Li and Mingli Chen, "The extended thin wire model of lossy round wire structures for FDTD simulations," IEEE Trans. on PWRD, Vol. 32, no. 2, 2017, pp. 2472-2480

[110] A. Canova, G. Gruosso, and M. Repetto, "Integral methods for analysis and design of low-frequency conductive shields," IEEE Trans. on Magn. vol. 39, no. 4, Jul. 2003, pp. 2009–2017.

[111] D. Romano and G. Antonini, "Augmented quasi-static partial element, equivalent circuit models for transient analysis of lossy and dispersive magnetic materials," IEEE Trans. on Magn., vol. 52 no. 5, 2016, pp.1-11

[112] D. Romano, G. Antonini, A. E. Ruehli, "Time domain PEEC solver including non-linear magnetic materials", IEEE Trans. on Magn., Vol. 52, no. 9, 2016, 7004911.

[113] Y. Du, Q. B. Zhou, and X. H Wang, "Equivalent circuit approach for evaluating low-frequency magnetic fields in the presence of non-ferromagnetic plates," IEEE Trans. Magn., vol. 45, no. 3, pp. 960–963.

[114] Nenghong Xia and Y. Du, “An efficient modeling method for 3-D magnetic plates in magnetic shielding,” IEEE Trans. on EMC, vol 56, no. 3, 2014, pp. 608-614

[115] G. Antonini, D. Romano, “Quasi-static partial element equivalent circuit models of linear magnetic materials”, IEEE Trans. on Magn., vol. 51, no. 7, 2015, 7003911

[116] Y. Du, Hongcai Chen and Mingli Chen, “Analysis of transient magnetic shielding made by conductive plates with a PEEC method,” IEEE Trans. on Magn.,vol. 53, no. 6, 2017, 6300404.

[117] Hidetosi Takahasi, “Double Exponential Formulas for Numerical Integration,” RIMS, 1974，pp. 721-741

[118] L. Xu, Y. Du and Q.B. Zhou, “The magnetic field and induced current arising from a cylindrical shell loop with an unbalanced current,” Electric Power System Research, vol. 71, 2004, pp. 21-26

[119] Rachidi, F. , “Influence of a lossy ground on lightning-induced voltages on overhead lines,” IEEE Transactions on Electromagnetic Compatibility, vol. 38, no. 3,1996, pp.250-264.